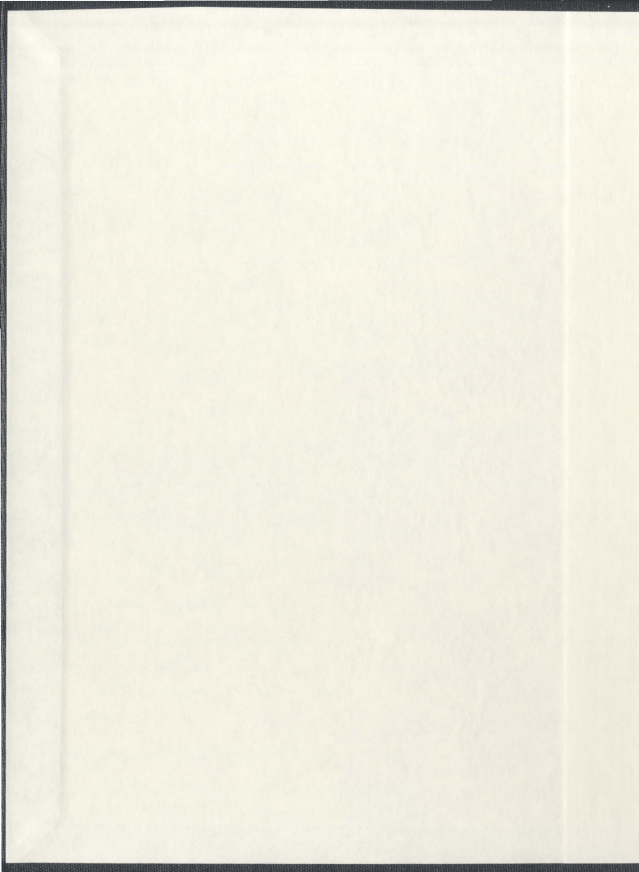


A THREE-DIMENSIONAL SIMULATION OF VORTEX
INDUCED VIBRATIONS (VIV) ON MARINE RISERS AT
HIGH REYNOLDS NUMBER USING COMPUTATIONAL
FLUID DYNAMICS

DAVID C. MURRIN



A Three-dimensional Simulation of Vortex Induced
Vibrations (VIV) on Marine Risers at High Reynolds
Number using Computational Fluid Dynamics

by

David C. Murrin, B.Eng. M. Eng.

A thesis submitted to the School of Graduate Studies
in partial fulfilment of the requirements of the degree of
Doctor of Philosophy

Faculty of Engineering and Applied Science
Memorial University of Newfoundland
June 2007

St. John's, Newfoundland, Canada



Abstract

The flow of seawater around marine risers is subject to vortex shedding which excites oscillations known as Vortex Induced Vibrations (VIV). When the VIV frequency approaches one of the natural frequencies of the structure, resonance occurs. This results in enhancement of the vibration amplitude of the structure and may have potentially destructive consequences. At present, the prediction of this phenomenon is one of the most challenging areas in the offshore industry.

The focus of this research is on the development of a new approach for simulating vortex induced vibrations on marine risers at high Reynolds numbers using a Large Eddy Simulation (LES) computational fluid dynamics code. This method considers the span-wise variation of the lift and drag forces, and determines the moment acting on the cylinder. The predicted motion then consists of a rotational component to accompany the traditional cross-stream translation.

A simulation of flow around a stationary cylinder was performed to establish the vortex shedding pattern and determine the lift and drag coefficients. At this point a harmonic model was invoked and the cylinder was free to respond to it's shed vortices. Results are presented for the simulation of turbulent flows past a 3 m long cylinder with 1 m diameter, undergoing vortex induced vibrations at a Reynolds number equal to 1×10^5 .

Acknowledgements

First, I would like to take this opportunity to thank my thesis supervisors, Dr. Neil Bose, Dr. Julio Militzer, and Dr. Eric Thornhill. It has been my great pleasure to work with each of you. Dr. Bose has been instrumental in moving this project forward and was always available, willing, and able to provide valuable guidance and a helpful hand when called upon. I am grateful to Dr. Militzer for providing me the focus and direction that I needed to press on when I was ready to throw my hands up in despair. The long chats about life, computational fluid dynamics, and everything in-between will be a treasure for my entire professional career. I would like to acknowledge Dr. Thornhill for his helpful suggestions and Dr. Rubens Campregher for providing sage advice on the design and development of the numerical routines contained in this dissertation.

I would also like to thank Memorial University of Newfoundland and Dalhousie University for providing the numerical facilities required for this project and I am grateful for the financial support provided by the Natural Sciences and Engineering Research Council (NSERC) of Canada and Petroleum Research Atlantic Canada (PRAC).

I am deeply indebted to my parents for creating an environment in which choosing this path seemed so natural. My brother, Matthew, and sister, Krista, have provided a ready ear and incisive mind to support and challenge me in my life and work, and

for that I thank you both. A special thanks to my young sons, David and Seamus for the opportunity to watch them learn and grow. Their uninhibited journeys of discovery served as great motivation throughout this research.

Finally, I would like to thank my wife Jennifer, for her unwavering support, encouragement and motivation throughout my studies. For putting up with all my mood swings, rants, raves, frustrations, and moments of jubilation during the course of this study, I am eternally grateful. She pulled me back down to earth when things were tough and always helped me to keep the proper perspective. I can only hope that I might someday be able to provide the same level of assistance to someone in a similar situation as the above individuals have provided me.

Contents

Nomenclature	xvi
1 Introduction	1
1.1 Overview of Thesis	3
2 Literature Review	5
2.1 Forced Oscillations	5
2.2 Structures in the Wake of VIV	8
2.3 Self Excited or Free Oscillations	10
2.4 Effect of Mass Damping	15
2.5 One vs. Two Degrees of Freedom Systems	18
2.6 Three Dimensionality	19
2.7 High Reynolds Number Flows	21
2.8 Numerical Simulations	25
2.9 Three-dimensional Wake effects	29
2.10 Summary of Literature Review	31
3 Methodology of the Research	33
3.1 Numerical Requirements for the Simulation of VIV	34
3.1.1 Large Eddy Simulation (LES)	34

3.1.2	Moving Geometry	35
3.1.2.1	Dimensionality	36
3.2	The Numerical Wind Tunnel	36
3.2.0.2	Hardware Requirements and Additional Software	38
3.3	Flow Past a Stationary Cylinder	41
3.3.1	Flow Structures in Wake	41
3.3.2	Strouhal Number	42
3.4	Flow-Structure Interaction	44
3.4.1	Dimensional Analysis	44
3.4.2	Effect of Cylinder Motion on the Wake	46
4	Code Development for the Simulation of VIV	48
4.1	Surrounding Cells method	48
4.2	Second-Order Velocity Interpolation	49
4.3	Calculation of Lift and Drag Forces	57
4.4	Quantifying the Induced Roughness	61
4.4.1	Controlling the solution with roughness approximation	63
4.5	Accounting for the span-wise variation in forces along the cylinder span.	64
5	Modeling Generalities and Validation	73
5.1	Domain Size	73
5.2	Grid Independence Study	74
5.3	Validating the 2 nd -order Velocity Interpolation	77
6	Simulation of Flow Past a Fixed Circular Cylinder at $Re = 10^5$	82
6.1	Computational Details	83
6.1.1	Computing Time	84
6.2	Results	87

6.2.1	Three-dimensional Effects	87
6.2.2	Correlation Coefficients	94
6.2.3	Span-wise Distribution of Force and Moment Coefficients	97
7	Simulation of 3D Flow Past an Elastically Mounted Cylinder Undergoing VIV	101
7.1	Modelling Details	102
7.2	Results for Cross-stream Translation Case	105
7.2.1	Three Dimensional Effects	106
7.2.2	Span-wise Distribution of Force and Moment Coefficients	110
7.3	Results for $I^* = 1$	112
7.3.1	Three-dimensional effects	114
7.3.2	Span-wise Distribution of Force and Moment Coefficients	119
7.4	Results for $I^* = m^*$	122
7.4.1	Three-dimensional effects	123
7.4.2	Span-wise Distribution of Force and Moment Coefficients	130
8	Conclusions & Recommendations	133
8.1	Summary of Code Development	133
8.2	Summary of Validation for 2 nd -order interpolation	135
8.3	Summary of Stationary Cylinder Simulations	135
8.4	Summary of Moving Cylinder Simulations	137
8.4.1	Summary of Results for Cross-Stream Translation	138
8.4.2	Summary of Results for $I^* = 1$	138
8.4.3	Summary of Results for $I^* = m^*$	139
8.5	Significant Contributions to the Field	141
8.6	Recommendations for Further Work	142

Bibliography	144
Appendix A: Grid Refinement Study	154
Appendix B: Matlab Scripts	156

List of Figures

1.1	Typical geometry for marine riser	2
2.1	Vortex shedding patterns behind VIV cylinder (Williams and Roshko)[85]	10
2.2	Response of flexible one degree of freedom circular cylinder (Feng) [23]	12
2.3	Phase Response of flexible one degree of freedom circular cylinder (Feng) [23]	13
2.4	Vibration amplitude data for impulsive and progressive regimes (Brika and Laneville) [19]	14
2.5	Amplitude response for low $m^*\zeta$ parameters (Khalak-Williamson) [40]	16
2.6	Amplitude response for high $m^*\zeta$ parameters (Khalak-Williamson) [40]	17
2.7	Discontinuities in Strouhal number for transition to three dimension- ality (Williamson) [82]	20
2.8	Hysteretic behavior at the first discontinuity in Strouhal number for transition to three dimensionality (Williamson) [82]	21
2.9	Variation in C_d versus Re for shear, 1:3, and uniform flow, 1:1 (Humphries and Walker) [33]	22
2.10	Variation in A/D versus Re for shear and uniform flow (Humphries and Walker) [33]	23
3.1	Eddies in turbulent flow	34

3.2	Cartesian adaptive grid	37
3.3	Transitions in disturbed regions: (a) TrW, (b) TrSL, (c), (d) TrBL . . .	42
4.1	Simple grid	49
4.2	Traditional IB velocity interpolation on stationary boundary	50
4.3	Second order linear interpolation	51
4.4	Second order bilinear interpolation	52
4.5	Simple surrounding cells flowchart	53
4.6	Identifying cells to East and West	54
4.7	Identifying cells to North and South	54
4.8	Identifying faces to East and West	54
4.9	Identifying surrounding faces	55
4.10	Differential lift and drag forces	58
4.11	Simple lift and drag integration flowchart	60
4.12	Boundary cell with both faces inside	61
4.13	Determining roughness on immersed boundary	62
4.14	Arbitrary two degree of freedom spring-mass-damper system	65
4.15	Free body diagram for multiple spring-mass-damper system	67
4.16	Displacement history for cylinder without span-wise lift moment . . .	71
4.17	Displacement history for cylinder with moment varying with C_l	72
5.1	Calculation domain	74
5.2	Illustration of separation bubble size	78
5.3	Grid Convergence Study at $Re = 100$	79
5.4	Single Sided Amplitude Spectrum of C_l at $Re = 100$	79
5.5	C_l and C_d vs time at $Re = 100$	80
5.6	Vorticity contours for stationary cylinder at $Re = 100$	81

5.7	Velocity contours for stationary cylinder at $Re = 100$	81
6.1	Computational domain for flow past stationary cylinder at $Re = 10^5$	85
6.2	Refined mesh for flow past stationary cylinder at $Re = 10^5$	86
6.3	Refined mesh around cylinder for flow past stationary cylinder at $Re = 10^5$	87
6.4	Refined mesh along span for flow past stationary cylinder at $Re = 10^5$	88
6.5	Coefficients of lift and drag for stationary cylinder at $Re = 10^5$	88
6.6	Amplitude spectrum of lift coefficient for stationary cylinder at $Re = 10^5$	89
6.7	Velocity vectors for stationary cylinder at $Re = 10^5$, and $y = 0.5$	90
6.8	Velocity vectors for stationary cylinder at $Re = 10^5$, and $y = 1.5$	91
6.9	Velocity vectors for stationary cylinder at $Re = 10^5$, and $y = 2.5$	91
6.10	Vorticity contours for stationary cylinder at $Re = 10^5$, and $y = 0.5$	92
6.11	Vorticity contours for stationary cylinder at $Re = 10^5$, and $y = 1.5$	92
6.12	Vorticity contours for stationary cylinder at $Re = 10^5$, and $y = 2.5$	92
6.13	Instantaneous span-wise vorticity iso-surfaces for flow past stationary cylinder at $Re = 10^5$. Iso-surfaces +2.0 and -2.0	93
6.14	Span-wise vorticity in mid-plane of stationary cylinder at $Re = 10^5$ ($z = 15D$)	94
6.15	Instantaneous span-wise vorticity iso-surfaces for flow past stationary cylinder at $Re = 10^5$. Iso-surfaces +2.0 and -2.0	95
6.16	C_l vs time at $Re = 10^5$ along span of stationary cylinder	95
6.17	Cross correlation coefficient along span of stationary cylinder at $Re = 10^5$	96
6.18	Distribution of lift coefficient along the stationary cylinder span at $Re = 10^5$	98
6.19	Distribution of drag coefficient along the stationary cylinder span at $Re = 10^5$	99

6.20	Moment coefficient and lift coefficient for stationary cylinder at $Re = 10^5$	100
6.21	Amplitude spectrum of moment coefficient for stationary cylinder at $Re = 10^5$	100
7.1	One degree of freedom spring-damper system	102
7.2	Two degrees of freedom spring-damper system (stream-wise and cross-stream)	102
7.3	Two degrees of freedom spring-damper system (stream-wise and rotation)	103
7.4	Coefficients of lift and drag for cylinder at $Re = 10^5$ oscillating in the cross-stream direction	107
7.5	Velocity vectors at $y=0.5$ for cylinder at $Re = 10^5$ oscillating in stream-wise direction	108
7.6	Velocity vectors at $y=1.5$ for cylinder at $Re = 10^5$ oscillating in stream-wise direction	108
7.7	Velocity vectors at $y=2.5$ for cylinder at $Re = 10^5$ oscillating in stream-wise direction	109
7.8	Instantaneous iso-surfaces stream-wise velocity for flow past a moving cylinder. Iso-surfaces $+0.5, 0.2$ and $-0.5, -0.2$	109
7.9	Cross correlation coefficient along span of cylinder translating in cross-stream direction at $Re = 10^5$	110
7.10	Distribution of r.m.s. lift coefficient along span of cylinder translating in cross-stream direction at $Re = 10^5$	111
7.11	Distribution of drag coefficient along span of cylinder translating in cross-stream direction at $Re = 10^5$	111
7.12	Moment and lift coefficients for cylinder at $Re = 10^5$ translating in cross-stream direction	112

7.13	Coefficients of lift and drag for translating and rotating cylinder with $I^* = 1$ at $Re = 10^5$	113
7.14	Velocity contours for moving and rotating cylinder at $Re = 10^5$, $I^* = 1$ and $y = 1.5$	115
7.15	Velocity vectors for moving and rotating cylinder with $I^* = 1$ at $Re = 10^5$, and $y = 0.5$	115
7.16	Velocity vectors for moving and rotating cylinder with $I^* = 1$ at $Re = 10^5$, and $y = 1.5$	116
7.17	Velocity vectors for moving and rotating cylinder with $I^* = 1$ at $Re = 10^5$, and $y = 2.5$	116
7.18	Velocity vectors showing 2C pattern for moving and rotating cylinder with $I^* = 1$ at $Re = 10^5$, and $y = 2.5$	117
7.19	Instantaneous iso-surfaces stream-wise velocity for flow past a moving and rotating cylinder with $I^* = 1$ at $Re = 10^5$. Iso-surfaces +0.2 and -0.2 m/s	117
7.20	3-D model of vortex shedding from moving and rotating cylinder with $I^* = 1$ at $Re = 10^5$	118
7.21	Cross correlation coefficient along span of moving and rotating cylinder with $I^* = 1$ at $Re = 10^5$	119
7.22	Distribution of r.m.s lift coefficient along span of the moving and rotating cylinder with $I^* = 1$ at $Re = 10^5$	120
7.23	Distribution of drag coefficient along span of the moving and rotating cylinder with $I^* = 1$ at $Re = 10^5$	120
7.24	Moment coefficient and lift coefficient for moving and rotating cylinder with $I^* = 1$ at $Re = 10^5$	121

7.25	Coefficients of lift for translating and rotating cylinder at $Re = 10^5$ and $I^* = m^*$	123
7.26	Velocity vectors for cylinder at $Re = 10^5$ and $I^* = m^*$, at $y = 0.5$. . .	124
7.27	Velocity vectors for cylinder at $Re = 10^5$ and $I^* = m^*$, at $y = 1.5$. . .	125
7.28	Velocity vectors for cylinder at $Re = 10^5$ and $I^* = m^*$, at $y = 2.5$. . .	125
7.29	2C pattern for cylinder at $Re = 10^5$ and $I^* = m^*$, at $y = 1.5$	126
7.30	Instantaneous iso-surfaces of stream-wise velocity for flow past a mov- ing cylinder with $I^* = m^*$. Iso-surfaces $+0.5, 0.2$ and $-0.5, -0.2$ m/s . .	126
7.31	Comparison of rotation angles for cylinder at $Re = 10^5$ for $I^* = 1$ and $I^* = m^*$	127
7.32	Comparison of amplitude ratios for cylinders at $Re = 10^5$ for $I^* = 1$ and $I^* = m^*$ and pure translation	128
7.33	Comparison of cross-stream cylinder velocities ratios for translating and rotating cylinder at $Re = 10^5$ for $I^* = 1$ and $I^* = m^*$	128
7.34	Cross correlation coefficient along span of moving cylinder at $Re = 10^5$ for $I^* = m^*$	129
7.35	Cross correlation coefficient along span of moving cylinder at $Re = 10^5$	130
7.36	Distribution of lift coefficient along span of moving cylinder at $Re = 10^5$ for $I^* = m^*$	131
7.37	Distribution of drag coefficient along the moving cylinder span at $Re =$ 10^5 and $I^* = m^*$	131
7.38	Moment and lift coefficients for moving cylinder at $Re = 10^5$ at $Re =$ 10^5 for $I^* = m^*$	132

List of Tables

3.1	Flow regimes over a smooth cylinder	43
5.1	Grid Convergence for 2 nd -order Benchmark	78
6.1	Computational Times for Numerical Simulation	84
6.2	Grid Convergence for flow over a Stationary Cylinder	86
7.1	Computational Times for Numerical Simulation of Moving Cylinder . .	105
7.2	VIV parameters for cylinder translating in cross-stream direction . . .	106
7.3	VIV parameters for case of $I^* = 1$	113
7.4	VIV parameters for case of $I^* = m^*$	122

Nomenclature

α	bi-linear interpolation coefficient
β	bi-linear interpolation coefficient
Δx_{target}	target cell dimension in the x -direction
Δy_{target}	target cell dimension in the y -direction
Δz_{target}	target cell dimension in the z -direction
ε	relative error
γ	correlation coefficient
φ	phase angle
Λ	correlation length
ν	dynamic viscosity
θ	angle
ρ	fluid density
τ	non-dimensional time
ζ	material damping coefficient
2c	co-rotating vortex pairs
2D	two-dimensional
2P	counter-rotating vortex pairs
2S	single vortex
3D	three-dimensional

A	amplitude of cylinder motion
a1	distance from spring/damper no. 1 to cylinder centroid
a2	distance from spring/damper no. 2 to cylinder centroid
Ar	aspect ratio
BL	boundary-layer
c	structural damping coefficient
Ca	added mass coefficient
c_{adapt}	grid adaptation criterion
C_d	drag coefficient
C_{dl}	out-of phase component of lift
C_l	lift coefficient
C_m	moment coefficient
C_{ml}	in-phase component of lift
CPU	Central Processing Unit
D	Diameter
DNS	Direct Numerical Simulation
f	forcing function for immersed boundary method
F	Force
f_{com}	common frequency at which lock-in occurs
F_d	drag force
f_{ex}	frequency of oscillation of a body
f_{inline}	frequency of oscillation in the inline direction
F_l	lift force
f_n	natural frequency
F_{px}	pressure contribution to drag force
F_{py}	pressure contribution to lift force

Fs	factor of safety
f_{st}	vortex shedding frequency for a body at rest
$f_{transverse}$	frequency of oscillation in the transverse direction
$F_{\mu x}$	viscous contribution to the drag force
F_v	viscous force
f_{vac}	natural frequency of an object in a vacuum
F_{xx}	magnitude of the second derivative of u -velocity at cell centroid
F_{yy}	magnitude of the second derivative of v -velocity at cell centroid
F_{zz}	magnitude of the second derivative of w -velocity at cell centroid
h	inside distance from the face velocity to the immersed boundary
I	moment of inertia
I^*	inertia ratio
I_d	moment of inertia of displaced body
k	spring constant
L	length
L_b	separation bubble length
LES	Large Eddy Simulation
L_f	eddy formation length
L_x	stream-wise distance from inside face to immersed boundary
L_y	cross-stream distance from inside face to immersed boundary
m	body mass
m^*	mass ratio
M_v	external moment acting on spring damper system
N_1	fine grid
N_2	coarse grid
p	pressure

r	grid refinement ratio
RANS	Reynolds Averaged Navier Stokes
Re	Reynolds number
S	separation region
SL	shear layers
St	Strouhal number
t	time
Tr	transition
U	velocity in the stream-wise direction
$u+$	ratio of local fluid velocity and friction velocity
u^*	friction velocity
VIV	vortex induced vibrations
V_r	reduced velocity
x	direction parallel to free stream
y	direction parallel to cylinder span
$y+$	dimensionless wall distance
z	direction perpendicular to free-stream

Chapter 1

Introduction

Vortex induced vibration is the most important dynamic response of a deep water riser [81]. The flow of seawater around these long cylinders is subject to vortex shedding. This is an unsteady oscillatory phenomenon, which causes the pressure distribution around the cylinders to fluctuate, resulting in forces perpendicular to the flow and structure. These forces excite forced oscillations of the cylinder known as vortex-induced vibrations. When the frequency of VIV approaches one of the natural frequencies of the structure, the amplitude of vibration is enhanced through a resonant phenomenon known as lock-in. Figure 1.1 shows the typical geometry of a marine riser. The deflected shape may vary due to a number of factors including shear currents, riser material, and the intended function of the riser. In general it is reasonable to assume that vertical sections of the riser (i.e at 90 degree angles of attack) are sufficiently long for local lock-in to occur. The current profile also varies from the surface to the ocean floor and there are generally large current velocities at the top that diminish with increasing water depth.

While vortex shedding on bluff bodies in the cross-stream and stream-wise directions has been described in a number of review papers over the past fifty years (Sarp-

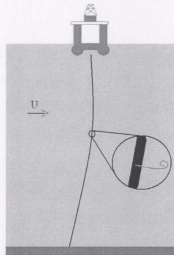


Figure 1.1: Typical geometry for marine riser

kaya [62], Feng [23], Bearman [9], Marcollo and Hinwood [45], Jauvtis and Williamson [35], etc.), the three-dimensional nature of vortex shedding has received very little attention, despite the general agreement that cylinder wakes are three-dimensional for Reynolds numbers greater than 150. Moreover, the majority of three-dimensional numerical simulations have been performed at Reynolds numbers much lower than the industry relevant range of $10^5 - 10^7$. A typical marine riser, for example, may have an outer diameter of 0.3 m and in some deepwater environments current velocities may reach as high as 2 m/s.

The focus of this research is on the development of a new approach for simulating vortex induced vibrations on marine risers at relatively high Reynolds numbers. This method considers the span-wise variation of the lift and drag forces, and determines the moment acting on the cylinder. The predicted motion then consists of a rotational component to accompany the traditional cross-stream translation. The movement of the cylinder, therefore, is no longer confined to a principal axis, which may influence

the prescribed motion. This is accomplished by describing the motion of the cylinder using a set of springs and dampers. A moment acting on the cylinder causes the springs on one end to compress, and stretch on the other, thus rotating the cylinder.

One of the major difficulties encountered in the simulation of this flow is the fact that the cylinder moves. In this research a number of innovative features have been incorporated into a Large Eddy Simulation (LES) computational fluid dynamics code initially developed at Dalhousie. The code originally included an adaptive unstructured Cartesian grid, and a first-order Immersed Boundary (IB) Method for boundary condition specification, but needed to be developed considerably for this research. In order to simulate the VIV phenomenon, the code was used to calculate the unsteady flow and at each time step the hydrodynamic forces acting on the cylinder were calculated in a separate routine based on the pressure distribution around the cylinder. This information was then used to solve three second-order ordinary differential equations, which gave the velocity and displacement of the cylinder in cross-flow, stream-wise, and rotational planes. This information was transferred back to the code where the cylinder was displaced and another cycle of LES calculations was started. The advantage of the Immersed Boundary Method is that there was no need to create a new mesh after the cylinder was displaced.

1.1 Overview of Thesis

The contents of each chapter in this thesis are summarized below:

- Chapter 2 provides the background for this research, and presents a summary of the major accomplishments in the study of vortex induced vibrations on cylinders.
- Chapter 3 establishes the methods used in the simulations.

- Chapter 4 discusses the development of numerical procedures and formulae required for these simulations.
- Chapter 5 presents some modeling generalities common to the simulations in this thesis along with a validation of the velocity interpolation routine described in Chapter 4.
- Chapter 6 discusses the simulation of flow over a stationary cylinder at $Re = 10^5$ and investigates the distribution of span-wise forces and degree of three-dimensionality present in the field.
- Chapter 7 explores the response of the cylinder to vortex induced loads in terms of vortex shedding patterns and three-dimensional force distributions.
- Chapter 8 provides the conclusions drawn from this thesis, highlights the new contributions, and suggests future research directions.

Chapter 2

Literature Review

The following chapter gives a brief review of the significant contributions to the understanding of vortex induced vibrations on circular cylinders.

2.1 Forced Oscillations

The majority of experiments on VIV have been performed on circular cylinders forced to oscillate at a fixed frequency, desired amplitude and Reynolds number. These experiments, known as forced oscillation experiments, are useful in isolating certain aspects of VIV, but the results of forced oscillation experiments may differ from the more realistic case where a cylinder is free to vibrate in response to forces in its wake. Such experiments are known as self-excited or free oscillation experiments and are discussed in section 2.3.

Bishop and Hassan [15] conducted the pioneering experiments of vortex induced vibrations on circular cylinders in 1964 using forced oscillations in the transverse plane. Their results, at $Re = 6000$ and $A/D = 0.25$, showed a jump in phase angle (between displacement and excitation) in the interval $0.86 < f_{com}/f_{st} < 0.95$, where Re , A/D , f_{com} and f_{st} represent the Reynolds number, dimensionless amplitude,

common frequency at which lock-in occurs and vortex shedding frequency for a body at rest, respectively. This behaviour delineated a hysteresis loop, and its discovery has proven to be a major accomplishment that has since been the focus of a great deal of research. Mercier [47] then conducted forced in-line and transverse oscillations for $4000 < Re < 8000$ and plotted drag and lift coefficients as functions of reduced velocity and A/D . His figures separated the drag coefficient into mean and oscillatory components and the lift coefficient into drag and inertial components. In 1976 Stansby [71] observed the phase jump of Bishop and Hassan at $f_{com}/f_{st} = 0.86$, $Re = 3600$ and $A/D = 0.25$ and attributed his results to a change in the wake above and below some critical limit.

In 1978 an important experiment was undertaken by Sarpkaya [62], who determined in-phase and out-of-phase components of time dependent force on a rigid cylinder for various values of A/D in the range of $6000 < Re < 35000$. In-line force observations showed that the in-line force increased as the transverse oscillation amplitude increased and that synchronization occurred at a frequency lower than Strouhal frequency for a stationary cylinder ($St = 0.21$) for $5000 < Re < 25000$. The transverse force observations showed that the in-phase and out-of phase components of lift (C_{ml} and C_{dl} , respectively) were independent of Reynolds number for $5000 < Re < 25000$ and that at lock-in there is a rapid decrease in the in-phase (inertia) component and an increase in the absolute value of the out-of-phase (drag) component. Furthermore, at lock-in for $A/D < 1$, the cylinder response is similar to that of periodic flow over a cylinder at rest. This important result shows that the in-phase coefficient of lift cannot be determined from an oscillating cylinder in a fluid at rest. This has been confirmed by the fact that $C_{ml} = 1$ for an oscillating cylinder in a fluid at rest, while experimental observations have shown that this value may be as high as 2.0 near synchronization. In 1983 Staubli [72] essentially repeated the experiments of Sarpkaya

at a higher Reynolds number ($Re = 60000$). He concluded that hysteresis observed in elastically mounted cylinders of certain damping and mass ratios is caused by a non-linear relation between the fluid force and amplitude of oscillation.

Gopalkrishnan [28] reported the vortex induced lift and drag components from forced oscillation experiments on a smooth circular cylinder at $Re = 10^4$. The results compared well with the works of Bishop and Hassan [15] and Staubli [72] and showed that the lift force phase angle was different for large A/D and small A/D . Furthermore, the range of reduced velocities where the lift coefficient excited the cylinder did not coincide with the lock-in region. It was surmised that the excitation region is dependent on phase and lock-in is frequency dependent. His results also showed that amplitude modulated forces (beating) cause a reduction in mean drag coefficient, an increase in r.m.s. oscillating drag coefficient, and that the magnitude of lift is similar to lift from sinusoidal forcing. In these experiments the reaction force was only measured at one end of the cylinder (which was suspended at both ends), and the load was assumed to be uniformly distributed. As a result, the span wise variation (3-dimensional effect) was not accounted for.

Moe and Wu [50] conducted a large set of experiments with free and forced oscillations using the same apparatus with various end-conditions. These included a) free in both directions, b) clamped in-line, free in transverse, c) clamped in-line, forced in transverse, d) free in-line, forced transverse. It was determined that a prevailing oscillation frequency resulted for similar lock-in regions in both free and forced oscillations. Furthermore, large self-excited transverse motions occurred for a wider range of reduced velocities if bodies were free in both directions, rather than restrained in-line. It was also determined that the lift force was irregular for all cases (more so for the self-excited cylinder) and that large random effects exist in the lift force for both free and forced cases (more so for in-line fixed than in-line spring supported).

Blevins [17] suggested that the drag and inertia coefficients obtained by Mercier [47], Sarpkaya [62], Staubli [72], Wu [86], Deep Oil Technology [73] and Gopalkrishnan [28] be combined into a single database for semi-empirical correlations for design purposes only.

2.2 Structures in the Wake of VIV

Before discussing the experiments performed on cylinders undergoing free oscillations it is important to consider the work that has been done on understanding the source of hysteresis in low Reynolds number flows over circular cylinders.

In 1972 Angrilli et al. [7] studied the relationship between vortex shedding and cylinder displacement for $2500 \leq Re \leq 7500$. They determined that for small oscillations the vortex trails were similar to those behind stationary bluff bodies. For larger oscillations it was determined that the trajectories of vortex trails must cross each other twice in order to reach a stable configuration in the wake. Zdravkovich [87], [88] analyzed the flow visualization patterns of the forced and free oscillation experiments of previous investigators. He suggested that the phase change in unsteady lift near synchronization could be explained by a change of timing of the newly shed vortices with respect to the displacement of the cylinder. He found that two very different modes of vortex shedding occurred in the lock-in region. At the beginning of the range, a vortex formed on one side of the cylinder was shed when the cylinder was near its maximum displacement on the other side. Near the end of the range, vortices were shed when the cylinder was near its maximum displacement on the same side.

It is clear that the character of vortex shedding influences the phase of the lift force, and hence the energy transfer between the fluid and the body. Williamson and Roshko [85] investigated the reason for the abrupt change in the character of vortex formation

through the synchronization region. They oscillated a vertical surface piercing cylinder along a sinusoidal path and photographed the path of aluminum particles that were floating at the free surface. Their results, in the range of $300 \leq Re \leq 1000$, identified a critical curve below which the vortex formation was similar to the classic von Karman vortex street and which is called the 2S mode. For reduced velocity values greater than the critical curve, two counter-rotating vortices (not necessarily of equal strength) were shed in each half-cycle. A double-wake type velocity profile resulted and the flow structure was denoted as the 2P mode (meaning two vortex pairs). Along the critical curve only two vortices were formed in each cycle and the shed vorticity is more concentrated than at other reduced velocities. This phenomenon coincides with the peak in lift forces from the experiments and is called resonant synchronization. They concluded that the shedding of more concentrated vorticity induced larger forces and that the abrupt changes in body forces through lock-in are therefore due to sharp changes in vortex dynamics. Furthermore, the jump in phase angle (between lift force and body motion) is due to a change in the timing of shedding that results from pairing of the 2P mode. Since either mode of vortex shedding may occur at certain reduced velocities, hysteresis results. A map of the vortex shedding patterns is included in Figure 2.1, where the *I* and *II* are the curves where Bishop and Hassan [15] observed the jump in lift force on the cylinder, and $\lambda = \frac{U}{f_{ex}}$. Line *I* corresponds to the decreasing reduced velocity tests and line *II* represents the results from incrementally increasing reduced velocity tests.

These experiments identified some important vorticity characteristics in the wake of bodies undergoing induced vibrations, however, they were performed over a small range of Reynolds numbers and may not be relevant to more realistic flows (at higher Reynolds numbers). Moreover, it has been suggested by Sarpkaya [64] that aluminum particles strongly affect the position and strength of vortices and vorticity distribution

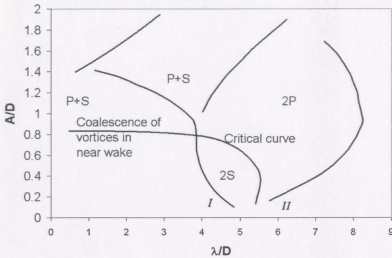


Figure 2.1: Vortex shedding patterns behind VIV cylinder (Williams and Roshko)[85]

near the free surface. Although Williams and Roshko [85] claimed that vortex patterns obtained using a dye method beneath the surface were similar, they did not report on the results of this technique. In order to expand the work of Williams and Roshko [85] to a wider range of applications, further testing is necessary at higher Reynolds numbers without surfactants.

2.3 Self Excited or Free Oscillations

This section reviews experiments performed on circular cylinders for the more realistic case of self excited or free oscillation and concludes with a comparison of forced and free oscillations.

In 1968 Feng [23] undertook one of the more famous contributions to VIV. His experiments were performed with a flexible one degree of freedom cylinder in a wind tunnel with $m^* = 248$, $\zeta = 0.00103$ and $m^*\zeta = 0.255$, where the mass ratio and

material damping coefficient were given by m^* and ζ , respectively. He measured f_{ex}/f_{com} , A/D and phase angle (φ) versus reduced velocity ($V_r = U/f_{vac}D$) for the following cases:

1. cylinder started from rest at a prescribed velocity
2. velocity increased incrementally with cylinder oscillating at steady state amplitude
3. velocity decreased incrementally with cylinder oscillating at steady state amplitude

For the experiments with the cylinder started from rest, it was observed, as shown in Figures 2.2 and 2.3 that for $V_r < 5$, A/D was very small and the frequency of oscillation for the cylinder was less than both the natural frequency of the cylinder and the frequency of vortex shedding. This is known as the inception phase of oscillations. For $V_r > 5$ the frequency of vortex shedding and frequency of oscillation approached each other (lock-in) and maximum A/D occurred for $V_r = 6$. At $V_r \approx 7$, the oscillation frequency of the cylinder returned to a value close to its natural frequency in a vacuum, f_{vac} (lock-out).

For the experiments with the velocity increasing incrementally, A/D was much higher than the results obtained when the cylinder started from rest at a prescribed velocity, and at $V_r \approx 6$, $A/D = 0.53$. At $V_r = 6.4$, A/D dropped to the value determined in the first set of experiments, and the phase angle changed by 35 degrees. As will be discussed later, this indicated a change in the wake structure.

For the third set of experiments the A/D data followed the results of the first case until $V_r \approx 5.9$, when A/D jumped back to higher values. This indicated a clockwise oscillation hysteresis loop. At the same reduced velocity, the phase angle changed by 60 degrees, indicating a counter-clockwise phase-hysteresis loop.

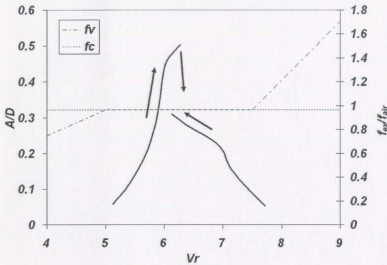


Figure 2.2: Response of flexible one degree of freedom circular cylinder (Feng) [23]

In 1993 Brika and Laneville [19] followed up on these experiments with a series of relatively low Reynolds number tests ($3.4 \times 10^3 \leq Re \leq 11.3 \times 10^3$) on a flexible circular cylinder in a wind tunnel. The tests were separated into the progressive regime (PR) and the impulsive regime (IR). In the progressive regime the cylinder oscillated at steady state amplitude and the velocity of the air was incrementally a) increased or b) decreased. In the impulsive regime the velocity of air was fixed and the cylinder was either a) released from rest or b) externally excited by a shaker at $A/D \approx 0.85$. As a final test, PR(a) was repeated for a velocity step twice as large as the original. The results, shown in Figure 2.4 were strikingly similar to Feng's [23] and hysteresis was once again identified for A/D and phase angle.

Brika and Laneville [19] determined that for velocities larger than the synchronization offset velocity (at about $V_r = 0.78$) and smaller than the lower critical velocity the system first tends toward an unavailable final state on extension of the lower branch. It then suddenly departs towards the upper branch to a second and available

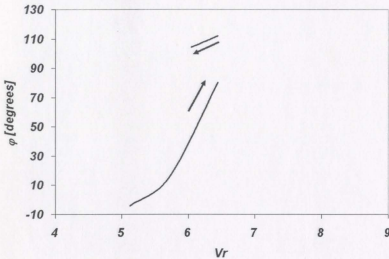


Figure 2.3: Phase Response of flexible one degree of freedom circular cylinder (Feng) [23]

state. It was also observed that the phase angle remained constant along the cable (within 5%), so the authors concluded that the flow mode is not governed, or affected by variations of vibration amplitude and the results should be comparable to those from uniform rigid cylinders.

Brika and Laneville [19] determined that a hysteresis loop existed for $V_r = 5.84$ and $Re = 7350$ at $A/D = 0.4$ and $A/D = 0.27$. According to the work of Williamson and Roshko [85], the shedding mode for both regions should be 2P, but Brika and Laneville [19] observed the 2P mode at $A/D = 0.4$ and the 2S mode at $A/D = 0.27$. The large difference in Reynolds numbers between Brika and Laneville [19] and Williamson and Roshko [85], as well as variation in amplitude (previously assumed inconsequential) along the flexible cable used by Brika and Laneville [19] could account for the different wake states observed by both sets of researchers. Brika and Laneville [19] conclude that the transition from 2P to 2S mode is very sensitive to hysteresis.

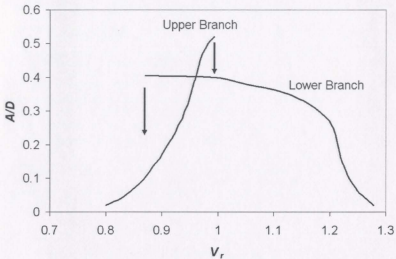


Figure 2.4: Vibration amplitude data for impulsive and progressive regimes (Brika and Laneville) [19]

In 1984 Bearman [9] undertook a major review of the forced and free oscillation experiments of vortex induced vibrations on bluff bodies. He observed that two shear layers were responsible for vortex shedding and that the motion of an oscillating cylinder controlled the instability mechanism leading to vortex shedding. It was also determined that the vortex shedding correlation length increased when the shedding frequency coincided with the body oscillation frequency and that the range of lock-in was a function of the amplitude (A/D). This means that while the shed vortices are invariably three-dimensional, they appear to be more two-dimensional during lock in. Furthermore, Bearman [9] concluded that fluctuating lift increased in the lock-in range due to improved two-dimensionality of the flow which increased the strength of vortices. He concluded his review with a comparison of free and forced oscillations. The advantage of forced oscillations is that reduced velocities and A/D can be varied independently, while they are intrinsically linked in free oscillation

experiments. The disadvantage of forced oscillations is that only a limited range of reduced velocities and amplitudes match those of free vibrations. He concluded that the results of free and forced vibrations are only the same if the exact history of motion is inconsequential. Moe and Wu [50] considered this very issue in 1990 and concluded that separation points and pressure distributions along the cylinder are strongly affected by the previous history of the motion. So, while forced oscillation experiments may provide insight into certain aspects of VIV, the true behavior can only be modeled by free oscillation.

2.4 Effect of Mass Damping

In 1996 Khalak and Williamson [39] investigated the effects of mass damping on the response of a rigid cylinder undergoing VIV in uniform flow. The test cylinder had a low mass ratio m^* and a normalized damping parameter, ζ , at least an order of magnitude smaller than previous experiments. Their results showed initial and lower branches of response due to changes in vortex shedding mode. It was determined that a low mass ratio m^* leads to higher response amplitude and larger range of response in the lower branch. The upper branch, however, is unaffected by changes in the mass ratio. Perhaps the most important finding in this paper was that, for cylinders with low mass ratios, lock-in cannot be defined by near matching of the shedding frequency with the frequency obtained from pluck tests in still water. It was observed, for example, that in the synchronization regime, the structural natural frequency was much lower than the frequency of oscillation, but “the frequency of oscillation was still below the vortex shedding frequency of a non-oscillating cylinder in this regime” [39].

Follow-up papers by Khalak and Williamson [40] and Govardhan and Williamson

[29] confirm that there are two distinct types of responses depending on if the parameter $m^*\zeta$ is high or low. As shown in Figures 2.5 and 2.6, at high $m^*\zeta$ only the initial and lower branches are observed.

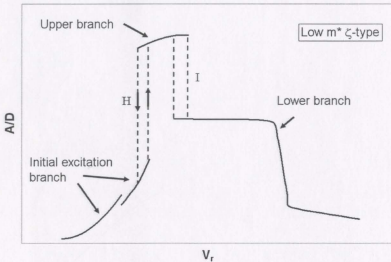


Figure 2.5: Amplitude response for low $m^*\zeta$ parameters (Khalak-Williamson) [40]

These branches are separated by continuous mode transition. At low $m^*\zeta$ values, initial, upper and lower branches were observed with the highest response amplitudes existing in the upper branch. Furthermore, the initial branch is characterized by the 2S vortex shedding mode and the 2P mode is found in both the upper and lower branch. In the upper branch, the two vortices have quite unequal strengths, while in the lower branch they are relatively equal in strength. The authors also observed that the jump from the initial to upper branch was hysteretic, while the transition between the upper and lower branch exhibited switching in the timing of the vortex shedding (denoted by H and I, respectively, in Figure 2.5). Govardhan and Williamson [29] conclude that the range of synchronization is controlled mainly by m^* , and that the peak amplitudes are controlled by $m^*\zeta$. Sarpkaya [64] has concerns with the use of

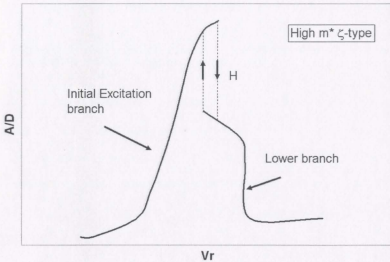


Figure 2.6: Amplitude response for high $m^*\zeta$ parameters (Khalak-Williamson) [40]

a combined mass-damping parameter and recommends that correlations should be confirmed at higher Reynolds number and other $m^*\zeta$.

Triantafyllou et al. [74] also analyzed the behavior of cylinders with low mass and damping in 2003 with a series of experiments on a rigid and flexible cylinders (in one and two degrees of freedom, respectively). The most important result from his experiments was the absence of hysteretic jump from the initial to upper branch. It has been proposed by Sarpkaya [64] that either the value of $m^*\zeta = 0.105$ used by Triantafyllou et al. [74] was not sufficiently small, or that the Reynolds number present in the experiments of Govardhan and Williamson [29] was too small for the shear layer transition to reach completion. This points to a Reynolds number effect which could be explained by experiments with " $m^*\zeta \leq 0.105$ where the minimum Re at $V_r = 3$ is larger than about 15 000 to resolve the existence or absence of various regimes in the A/D versus V_r plot at industrially significant Reynolds numbers"[64].

2.5 One vs. Two Degrees of Freedom Systems

Most of the work in VIV has been done on single degree of freedom systems with the assumption that oscillations in the in-line direction do not strongly affect the behavior of the cylinder. Jong and Vandiver [37] studied the relationship between in-line and cross-flow VIV of cylinders and determined that the motion in the two directions are not independent of each other. The added mass is a function of the type of motion of the body, and is much different for one and two degree of freedom systems. Moreover, differences such as kinetic energy and phase angle complicate the motion even more.

Sarpkaya [63] studied two directional (bi-harmonic) free oscillations in 1995 and found that A/D values and the range of lock-in frequencies were both 20% larger at $Re = 35 \times 10^3$ for two directional oscillations compared to their single degree of freedom equivalents. They concluded that the variation of A/D over frequency ratios such as $f_{in-line}/f_{transverse}$ are very complicated, indicating changes in the wake.

There has been some disagreement on this subject as evidenced by the work of Jauvtis and Williamson [35] in 2002. Based on their forced oscillation experiments on a cylinder in two degrees of freedom, they concluded that “the freedom to oscillate in-line with the flow affects the transverse vibration surprisingly little”. Most other researchers, however have arrived at completely different conclusions, which leads one to believe that the experiments of Jauvtis and Williamson [35] may have been influenced by the fact that both the in-line and transverse frequencies were set equal to one another. Marcollo and Hinwood [45] contradicted the work of Jauvtis and Williamson [35] with their experiments on cross-flow and in-line responses of long flexible cylinders subjected to uniform flow. They concluded that “In line vibration is found to have strong dependency on the cross flow vibration and is forced at frequencies very different to that which would be predicted a priori”. It is clear from the foregoing that cylinders undergoing VIV that are constrained in one direction behave differently from

cylinders with two degrees of freedom. The question that remains, however, is what this means for cylinders free to move in more than two directions. To the author's knowledge this subject has not received considerable attention and no experiments have been undertaken to address this issue. This may be an area that would benefit from numerical simulation, since restraints can be easily applied to numerical models. The promising field of numerical simulations is discussed in Section 2.8.

2.6 Three Dimensionality

The wake behind even a nominally 2-dimensional cylinder can produce vortices with 3-dimensional character. With this in mind, Williamson [82] observed 3-dimensional structures behind the wake of a circular cylinder for $Re > 178$. It had been traditionally assumed that these structures were the result of Kelvin-Helmholtz vortices caused by oscillations within the separating regions. Williamson [82] showed that these structures were in fact the result of deformation of the primary wake vortices and that the transition to three-dimensionality occurs through two discontinuities in the Strouhal number. As shown in Figure 2.7, the first discontinuity occurs at $170 \leq Re \leq 180$.

This corresponds to the hysteretic transition from periodic and laminar vortex shedding to the formation of vortex loops. The second discontinuity occurs over $225 \leq Re \leq 270$ and corresponds to the transition from vortex loops to finer stream-wise vortices, which do not display hysteretic behavior. As shown in Figure 2.8, the behavior at the first discontinuity is hysteretic.

The 3-dimensionality of vortex induced vibrations was studied by Voorhees and Wei [76] in 2002. Specifically, they investigated the three dimensionality in the wake of a surface piercing rigid cylinder ($m^* = 190$ and $m^*\zeta = 0.103$), mounted as an inverted pendulum for $2300 \leq Re \leq 6800$. The cylinders underwent free vibration

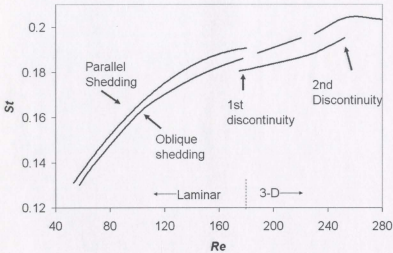


Figure 2.7: Discontinuities in Strouhal number for transition to three dimensionality (Williamson) [82]

and produced results consistent with experiments on elastically mounted cylinders with similar mass ratio and damping. In general, results showed that Karman vortices produced strong axial flows that were directed towards the free surface. Below the free surface, these flows were the result of linearly increasing oscillation amplitude along the span. Near the free surface, however, there was an equal likelihood of up-flow or down-flow. Interestingly, the up-flow and down-flow were well correlated with the quasi-periodic beating of the cylinder amplitude in the synchronization range. An important result, then is that the free surface disrupts the primary up-flow mechanism below the free surface, while inducing the Karman vortices at the top of the cylinder to spread laterally. Finally, it was concluded that at the free surface, vortex formation depends on the size of the gap between the cylinder and the free surface.

As discussed in Section 2.3, Bearman [9] also studied three-dimensionality behind circular cylinders undergoing VIV and observed increased correlation lengths during

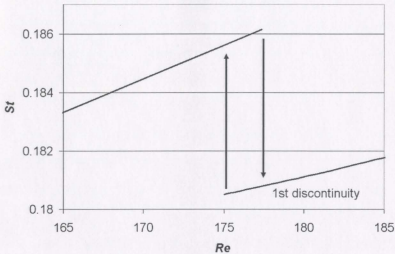


Figure 2.8: Hysteretic behavior at the first discontinuity in Strouhal number for transition to three dimensionality (Williamson) [82]

lock-in. This indicates that over certain lengths along the cylinder span during lock-in, the flow becomes more 2-dimensional. The extent of the correlation length has not been established, however, for a wide range of Reynolds numbers, and as discussed in Section 2.8, three dimensional simulations produce results that compare better with experimental work. The foregoing underscores the requirement of numerical studies of vortex induced vibration to be fully three-dimensional.

2.7 High Reynolds Number Flows

By far the majority of the work done on the vortex induced vibrations of rigid and flexible cylinders has been performed at low Reynolds numbers, Re . As a result the occurrence of VIV at high Re and modal response of structures is poorly understood. Designers have been forced to use high safety factors due to either a lack of data or practical experience with VIV at high Reynolds numbers. Moreover, the experiments

that have been undertaken at high Re are generally case-specific or proprietary.

Nonetheless, a number of important VIV studies have been performed at relatively high Reynolds number. Humphries and Walker [33] tested a rigid cylinder ($m^* = 1.98, m^*\zeta = 0.0283$) in uniform and shear flow for $5 \times 10^4 \leq Re \leq 4 \times 10^5$. Their results, shown in Figures 2.9 and 2.10 showed that the drag coefficient was much higher compared to a rigid cylinder at rest and was largest for VIV in uniform flow. The legends in these figures describe the extent of shear flow by the ratio of the minimum to maximum free stream velocity used in the experiment. For example 1 : 1 corresponds to uniform flow and 1 : 3 represents a linear shear flow in which the maximum free stream velocity is three times larger than the minimum free stream velocity.

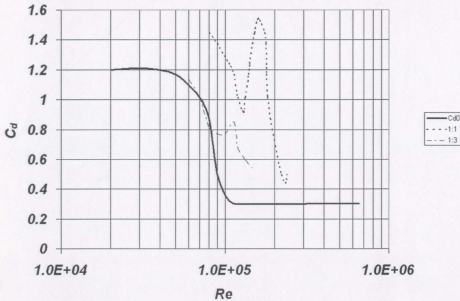


Figure 2.9: Variation in C_d versus Re for shear, 1:3, and uniform flow, 1:1 (Humphries and Walker) [33]

The drag coefficient behaved similar to that of a rigid, non-VIV, cylinder (C_{d0}) entering the critical regime (or drag bucket), in that it underwent a considerable

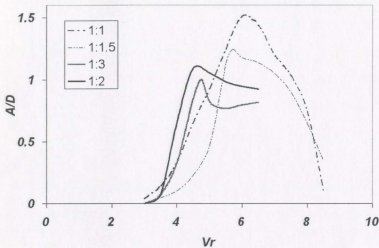


Figure 2.10: Variation in A/D versus Re for shear and uniform flow (Humphries and Walker) [33]

decrease in value. At lock-in, however, in 2 degrees of freedom, the drag coefficient increased sharply, and VIV took place. In the critical regime, C_d reached a maximum before the maximum A/D . In shear flows it was observed that the drag coefficient increased with increasing shear and that lock-in occurred with smaller peaks at lower Re . Furthermore, with increasing shear, the maximum A/D decreased towards unity and the range of lock-in increased.

Huse et al. [34] performed large scale model testing of deep sea risers (90 m long) in sheared currents and determined that vortex induced vibrations cause resonant axial vibrations along the length of the cylinder whether the riser is pinned at both ends or free at one end and pinned at the other. They concluded that reducing both the lateral and axial excitation is important in the reduction of high axial stresses. They also determined that, at high Re , A/D values for cylinders with pinned-pinned connections are generally smaller than for cylinders with both ends free to move

in the axial direction. This raises important questions about the influence of the connections between the spans that make up a riser. According to Sarpkaya [64], the elastic connections may behave as a strong damper, which increases the stiffness of the line, and hence reduces the amplitude of VIV. More testing is necessary in this area to determine the role that span connections, or couplings, may play in the dynamics of VIV. Finally, Huse et al. [34] conclude that high Reynolds number data are not significantly different from sub-critical data above $Re = 20000$.

Tentative conclusions for high Re VIV were presented by Sarpkaya [64] based on conversations with representatives of large petroleum concerns and are summarized here.

- I As Re increases from 4×10^5 to $\approx 10^6$, the Strouhal number, St , is undefined for steady flow over a smooth cylinder. For a cylinder undergoing vortex induced vibrations St is indeed definable over this range and increases from $\sim 0.18 - 0.24$ due to enhanced correlation.
- II Cylinders with small roughness exhibit small A/D values and if the roughness is increased, A/D increases. The same cylinder undergoing forced oscillations behaves similarly to a cylinder undergoing free oscillation.
- III None of the experiments with $Re > 20000$ show the initial branch that Khalak and Williamson [40] observed at $Re < 5000$. Furthermore, vortex modes have only been mapped at $Re < 10^3$, and it may be difficult to photograph coherent structures in the wake at much higher Reynolds numbers.
- IV Free oscillations at large Re are not sinusoidal. It is proposed, then, that the A/D , phase angle, vortex structures and other influencing parameters never become fully established (periodic). Each cycle in free oscillation is

affected by the character of the previous cycle, so branches in the A/D versus V_r plots are never exhibited, due to the ever changing flow topology.

V High Re lift, drag and amplitude data for smooth cylinders are similar to results for $20000 \leq Re \leq 60000$ except for the smooth St and C_d transition. At issue is the manner in which to quantify the effects of the end conditions for single span experiments versus continuous pipes, to account for multiple modes and mode interfaces, and to suppress VIV without drag penalty.

VI The interpretation and planning of experiments will be greatly improved by the dissemination of large-scale proprietary data.

2.8 Numerical Simulations

Experimental investigations of VIV have been quite successful at low Reynolds numbers but studies at industry relevant Reynolds numbers (on the order of $10^5 - 10^7$) have proven difficult in an experimental setting. The numerical simulation of VIV through computational fluid dynamics has therefore arisen as a practical alternative. Numerical simulations of vortex induced vibrations have received considerable attention in recent years, but significant, three-dimensional contributions are still very few. This is due, in part, to the incredible complexity inherent in three-dimensional simulation of fluids at high Reynolds number, notwithstanding the fluid structure interaction that is not fully understood. Gabbai and Benaroya [27] outline four issues to be considered for any numerical simulation: modeling of the flow field, modeling of the structural vibration, modeling of the fluid-structure interaction, and data analysis. While there are a number of possible numerical methods for computational fluid dynamics, it has been shown that LES and DNS hold the most promise for understanding the

wake-boundary-layer interaction [48], especially at high Reynolds numbers, and for moving geometries. Limitations in computing power have prevented DNS simulations for Reynolds numbers greater than around 5000 and even these are for the simplest problems, like channel flow. It would seem then, that for the immediate future, the simulation of vortex induced vibrations can best be accomplished using large eddy simulation, and this is the focus of the work outlined in this section.

Tutor and Holdo[75] investigated the benefits of 3D simulation in 2000. Using a 2D and 3D sub-grid scale LES model, they forced a cylinder to oscillate in the transverse direction at $A/D = 0.11$, $Re = 2.4 \times 10^4$, and $V_r = 5.4$ and compared the results. Their results, showed a departure from two-dimensionality a short distance behind the cylinder.

The spacing between simulated vortices was also compared and it was observed that the 3D simulation predicted more room for the vortices to develop behind the cylinder. This translated into more elongated and slightly weaker vortices, with a longer time averaged recirculation length. A slight phase difference between the two simulations was also observed and the 3D simulation showed better agreement with the experimental work of Bearman and Curie [10] at equivalent reduced velocity. Finally, the 3D simulation predicted smaller time averaged drag coefficient and absolute pressure than the 2D simulations and it was concluded that the deviations between the simulations were attributed to three-dimensionality of the wake. These results support the notion that simulations of vortex induced vibrations at high Reynolds number should be performed by three-dimensional codes.

A criticism of this type of simulation is the fact that it is essentially a forced oscillation, having the same limitations as the experimental equivalent. A simulation of self-excited vortex induced vibration requires a model that couples the cylinder motion and the fluid forcing function such that the two are calculated simultaneously.

Al-Jamal et al. [5] simulated self-excited VIV at $Re = 8000$ for a range of damping ratios and natural frequencies using a 2D LES code and compared their results to the work of Govardhan and Williamson [29]. The immediate concern with a 2D simulation is the assumption of two-dimensionality. Most 2D codes over-predict the drag coefficient for large Reynolds numbers by 5-10% [5] and the results from 3D codes provide better agreement with experimental data (confirmed by Tutor and Holdo [75]). Al-Jamal et al. argue that a 2D simulation has its merits since the lift and drag coefficients are predicted more accurately when VIV begins, because at this point, the wake correlation length increases and the 3D influence of vortex shedding is diminished. They do concede, however, that there is some difference in the vortex shedding behavior when $Re > 7000$ and there is significant turbulence in the wake of the cylinder. For their simulation, the vibratory motion of the cylinder was predicted by the following non-dimensional one degree-of-freedom model:

$$\frac{d^2Y}{d\tau^2} + 4\pi f_N \zeta \frac{dY}{d\tau} + (2\pi f_N)^2 Y = \frac{1}{m^* \pi} C_L(\tau) \quad (2.1)$$

where Y is the displacement of the cylinder relative to the at-rest position, $dY/d\tau$ is the transverse velocity of the cylinder, ζ is the material damping ratio, f_N is the natural frequency, m^* is the ratio of the cylinder mass to the mass of the displaced fluid (the mass ratio) and C_L is the instantaneous lift coefficient.

Their results showed that as ζ was increased, the beating response was less pronounced, and the range of the lock-in region and peak A/D decreased. The plots of A/D versus V_r did not identify the upper branch described by Govardhan and Williamson [29], and the lower branch did not reach a constant value for $V_r > 13.0$. The authors speculate that the discrepancy was likely due to the fact that the reduced velocity in the simulation was varied by changing the natural frequency of the cylinder,

rather than changing the fluid velocity (and hence Reynolds number). This meant that at $V_r > 13.0$, the cylinder oscillation frequency was very low due to negligible cylinder stiffness.

An important result from the simulation was that during lock-in the ratio of the cylinder oscillation to the natural frequency was less than unity observed by Govardhan and Williamson [29]. This was likely because Govardhan and Williamson used a forced regular sinusoid as the forcing function and assumed a constant fluid damping. In contrast, the simulation of Al-Jamal et al.[5] incorporated an irregular forcing function and the fluid damping was calculated implicitly in the fluid forces and varied with time.

Perhaps the most important result from the study was the absence of the 2P and 2S modes of vibration identified by Williamson and others([19], [85] [40], [29]). Govardhan and Williamson [29] state that visualization was unclear for $Re > 3700$ and to this point vibration modes still haven't been established for moderate to high Reynolds numbers. It is therefore not surprising that 2P and 2S modes of vibration were not observed by Al-Jamal et al.[5], since there is no evidence to indicate that they even exist in this flow regime. Furthermore, according to Zdravkovich [89], shear layers around cylinders begin to show instabilities at $Re \approx 1300$ and are fully turbulent at $Re \approx 1100$. For this work, then, the wake was likely in the transition range, still developing, and doubtlessly different from the wake at a much smaller Reynolds number. This becomes even more pronounced in the case of VIV, since the shear layers are time dependent. Moreover, while the work of Govardhan and Williamson [29] was based on forced sinusoidal oscillations, the motion of the cylinder for the 2D simulation of Al-Jamal et al.[5] was irregular, and not purely sinusoidal. As discussed in Section 2.7, vortex structures and other influencing parameters may never become fully established (periodic) for irregular flows due to time dependent A/D and phase

angle. Al-Jamal et al.[5] contend that “the lack of constancy in amplitude and phase angle could quite likely lead to the lack of repeatability in vortex formation which certainly could suppress the standard mode patterns”. They conclude that a direct comparison between forced and self excited oscillations cannot be made, especially when self-excited oscillation is not sinusoidal and phase angle is not constant.

2.9 Three-dimensional Wake effects

While two-dimensional vortex shedding on bluff bodies has been described in a number of review papers over the past fifty years, the three-dimensional nature of vortex shedding has received very little attention, despite the general agreement that cylinder wakes are three dimensional for $Re > 150$ [89]. Nevertheless, Williamson, [84] identified oblique and parallel vortex shedding, and mode A and mode B three-dimensional instabilities in the wake of circular cylinders for laminar and turbulent flow regimes. Oblique shedding influences the amplitude, frequency, and phase of the flow induced forces and the transition from one oblique shedding mode to another has been linked to the existence of discontinuities in the relationship between the Strouhal number and the Reynolds number for laminar flows. Slaoutli and Gerard, [68], studied the effect of end plates on the wake of circular cylinders at low Re and determined that the shedding pattern (whether oblique or parallel) depended on the end conditions. Williamson concluded that the oblique and parallel modes of vortex shedding are intrinsic to the flow around cylinders and may be instigated by the end conditions.

The majority of numerical investigations of vortex shedding in the wake of circular cylinders have been two-dimensional. This is largely due to the computational expense of three-dimensional simulations, especially at higher Reynolds numbers. Mittal [49] simulated the three-dimensional flow past a circular cylinder with low aspect ratio

($L/D=16$) at $Re = 100, 300$ and 1000 . Mode A and mode B instabilities were identified using a computational domain with one 'slip' wall and one 'no-slip' wall. It was shown that parallel shedding persisted in the simulations for $t < 100$ s. Beyond this time, oblique shedding occurred. They concluded that, since other researchers used slip-wall end conditions in their simulations and did not observe oblique vortex shedding, the end-conditions are responsible for oblique and parallel modes and both are intrinsic to the flow. Despite the large body of data showing that the wake behind the cylinder is 3-D and varies along the span, a plane of symmetry at mid-span was invoked in this work. In addition, the vortex induced force and frequency data was only given at the mid-span and variation along the span was not reported.

Evangelinos and Karniadakis [21] performed a Direct Numerical Simulation for the flow over a stationary rigid cylinder assuming periodic boundary conditions. Only results at mid-span were given and no span-wise variation of the unsteady forces was reported. Norberg [54] presented a review of significant 2-D and 3-D simulations over the range of $45 < Re < 4.4 \times 10^4$ for rigid, smooth, long, and unconfined (low blockage) cylinders. The report showed that the 3-D simulation of Lu et al. [43] at $Re = 10^4$ produced a fluctuating lift component of 0.46 at the mid-span. Furthermore, mid-span approximations of Strouhal and r.m.s. lift coefficient for the range of $1.6 \times 10^3 - 1.5 \times 10^5$ and $5.4 \times 10^3 - 2.2 \times 10^5$, respectively, were provided by the following empirical functions:

$$\text{Strouhal number: } 0.1853 + 0.0261^{(-0.9x^{2.3})} \quad (2.2)$$

$$\text{Sectional r.m.s. lift coefficient: } 0.52 - 0.6x^{-2.6} \quad (2.3)$$

where $x = \log \frac{Re}{1.6 \times 10^3}$.

So et al. [70] assessed the validity of 2-D assumptions on mean drag and flow induced forces for a stationary circular cylinder with $Re = 100$ and aspect ratio of 16, using finite volume and lattice Boltzmann numerical techniques. They found that the calculated mean drag and r.m.s. lift coefficients varied greatly across the span and that vortex shedding changed from parallel to oblique over the time range of $600 \leq t \leq 900$. They also found that lift and drag signals go through a series of transitions for $t \leq 200$, $200 \leq t \leq 500$, and $t \geq 500$, and conclude that the variation partially explains why there is so much scatter in the lift and drag coefficients in the literature.

In 2005, Flemming and Williamson [25] performed a series of VIV experiments on a hanging cylinder pin connected at one end, and free in the other. The results showed a new mode of vortex shedding near the pin in which a pair of co-rotating vortices were formed. This mode was subsequently named the 2C mode of vortex shedding, and illustrated that all of the shedding mode shapes for cylinders undergoing VIV have may not have been discovered.

2.10 Summary of Literature Review

To a large extent, the experiments discussed in this chapter have been of limited value for the case of marine risers at relatively high Reynolds number. The experimental work, for example, has mostly been dedicated to forced oscillations at low Re , and the results of a smaller number of free-oscillation experiments have either been performed at low Re or have not been published. Furthermore, the majority of the numerical work was performed by two-dimensional codes at low Re and the small number of three-dimensional codes used to simulate VIV have been performed almost exclusively at lower Re . Finally, in all of the simulations it was assumed that the flow around

the riser became increasingly two-dimensional at the onset of VIV and that there was no amplitude variation over the span of the cylinder. To date, the validity of these assumptions has not been investigated and one of the aims of this thesis is to determine whether the assumption of two-dimensionality is justified. Another important question that arises from all of the previous research is the extent to which the experimental apparatus influenced the behaviour of the riser. For example, span-wise amplitude variation would not be apparent if the experimental apparatus was restricted to planar (cross-stream and/or stream-wise) motion.

The research presented in this thesis investigates the vortex shedding modes and influence of span-wise force variation for cylinders undergoing vortex induced vibrations in the translational, as well as rotational planes at relatively high Reynolds number ($Re = 10^5$).

Chapter 3

Methodology of the Research

Under normal operating conditions, the flow around full-scale marine risers is at high Reynolds number on the order of $10^5 - 10^7$ and the risers have low structural damping. The focus of the current work was on the simulation of the VIV phenomenon at high Reynolds numbers for risers translating and rotating in the cross-stream plane.

To achieve this goal the research was done systematically for a series of milestone events. These included:

- Comprehensive literature review
- Identification and development of a suitable numerical code and required dimensionality
- Simulation of flow past a fixed circular cylinder
- Simulation of flow structure interaction

A review of the pertinent literature was presented in chapter 2, and the remaining topics are discussed here.

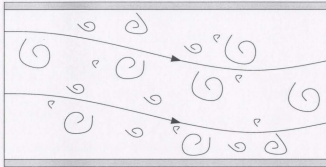


Figure 3.1: Eddies in turbulent flow

3.1 Numerical Requirements for the Simulation of VIV

As discussed in Chapter 2 Large Eddy Simulations hold promise for understanding flows at critical Reynolds numbers with moving geometry. The tremendous computational expense of Direct Numerical Simulation is prohibitive for VIV simulations at significant Reynolds numbers and LES is seen as the most practical alternative.

3.1.1 Large Eddy Simulation (LES)

Turbulent flows contain a wide range of length and time scales. One of the key challenges in turbulence research is understanding relationships between the structure, dynamics, and statistics of small and large scales of motion. Figure 3.1 shows an illustration of the different eddy sizes that might exist in a turbulent flow.

It has been suggested that while a full simulation of all of the length and time scales using DNS could be quite expensive (computationally), a method that resolves the largest eddies and models the effects of the small eddies may also be useful [69]. This is known as Large-Eddy-Simulation (LES). The large-scale motions are generally more energetic than the small-scale ones, and are by far the most effective transporters

of the conserved properties [24]. The small-scale motions, in contrast contribute little in terms of transport. Large-eddy simulations are three dimensional, time dependent and much less costly than DNS. Furthermore, LES is the preferred method when DNS is not a practical option, such as in high Reynolds number flows or flows with complex geometry. Thus, in LES the dynamics of large scale (energy containing) motions (which are affected by the flow geometry and are not universal) are computed explicitly whereas the influence of smaller scales (energy dissipating) are represented by simple models such as eddy viscosity. Traditional eddy viscosity LES models simulate the energy cascade by dissipating energy for all wavelengths. Multiscale LES models split the resolved scales of the simulation into 'large' and 'small' using a filter. The large scales do not require a model, while the unresolved small scale needs a model to dissipate the energy. Although an eddy viscosity model using the Reynolds Averaged Navier-Stokes (RANS) [80] equations provides good predictions for certain types of flows such as pipe or channel flows and flat plate boundary-layers, it fails to represent accurately flows where large scale unsteadiness is significant - such as the flow over bluff bodies which involves unsteady separation and vortex shedding. For these flows, large eddy simulation (LES), which resolves the large-scale unsteady motion explicitly, is a better option. Conceptually, LES is situated between Direct Numerical Simulation (DNS) and the RANS approach.

3.1.2 Moving Geometry

The analysis of VIV on marine risers is complicated by the fact that the geometry is not fixed in space. Most CFD codes apply body-fitted coordinates where the mesh conforms to an object's boundaries. When this object moves, the entire mesh must be regenerated at each time step, which increases the computational expense of the simulation. A code that minimizes or eliminates this procedure is well suited to the

simulation of vortex induced vibrations.

3.1.2.1 Dimensionality

The increased correlation length associated with the VIV phenomenon during lock-in may lead one to assume that a two-dimensional simulation would sufficiently describe the behavior of circular cylinders undergoing VIV. As discussed in Chapter 2 the extent of this correlation length has not been studied extensively and 3D simulations show better agreement with experimental work at moderate Re . Three-dimensional numerical codes are therefore essential to adequately simulate the VIV phenomenon. Based on these findings it was decided to use a fully 3D Large Eddy Simulation that is effective at modelling a moving geometry.

3.2 The Numerical Wind Tunnel

The Numerical Wind Tunnel (NWT) [2] is a 3-dimensional CFD simulation tool developed by the Centre for Marine Vessel Development and Research at Dalhousie University, Halifax, Canada. It is capable of simulating flows around multiple, complex, moving geometries using Large-Eddy Simulation. The main features of the code include: boundary conditions enforced with the Immersed Boundary Method (IMBM); anisotropic Cartesian adaptive staggered mesh; time advancement by the fractional step method; and multi-scale LES turbulence model.

To overcome the re-gridding requirements inherent to most simulations with moving geometry, the immersed boundary method was proposed by Peskin [57]. This method models complex geometries by representing the necessary shape through additional force terms in the momentum equations and has found wide application in Bio-Fluid Mechanics for solving flows such as a swimming fish, a pulsing heart and

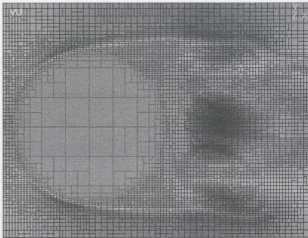


Figure 3.2: Cartesian adaptive grid

flow in a flexible blood vessel. Fadlun [22] proposed an alternative method for the types of flows considered here, namely those where the coupling between the moving boundaries and flow is one way and the boundary is known as a function of space and time. This method lends itself very well to the simulation of any flow with complex and or unsteady boundaries and uses Cartesian meshes. Figure 3.2 presents a close up view of the grid around a cylinder. It is notable that the round surface is approached by stair-like successions of rectangular cells and that the approximation can be improved by increasing the number of cells or implementing a second order approximation of the immersed boundary.

Ham et al. [30] successfully used anisotropic local grid refinement on Cartesian grids as an alternative to embedded-grid techniques proposed by Fadlun [22]. Localized grid refinement allows for fewer cells to be used far from the flow feature and a higher concentration of cells near the boundary. This means that the linearized velocity profile will be more accurate because the grid spacing near the boundary is small. The process of refining and coarsening (combining) cells is called grid adaptation. As

stated by Ham et al. [30], "the optimal mesh is the smallest mesh (i.e. mesh with the fewest cells) for which the error associated with each cell is less than a specified tolerance". The NWT uses the IMBM as modified by [22] with the anisotropic Cartesian grid of [30].

For time advancement the NWT uses the Fractional Step Method. A pseudo-pressure is used to correct the velocities and enforce continuity at each time step. The transient anisotropic Cartesian grid used for the NWT is fully unstructured and staggered. While collocated meshes may be better suited for steady and low Reynolds number flows, the accuracy of the collocated scheme is diminished for turbulent flows. Under these circumstances, non-physical oscillations in the pressure field may occur and the collocated method must be adapted to conserve the convective term. Conversely, the staggered arrangement is unconditionally stable, and correctly models the turbulent behavior without introducing artificial dissipation. Following the method proposed by Kim and Choi [41], the integration of the momentum and continuity equation is carried out in steps. Initially, the momentum equations are solved for a velocity using the pressure values from the previous time step and then the estimated velocity field is used to find the new pressure. This new pressure is then used to calculate the velocities at cell centre and face normal. In their derivations and the method used here, a fully implicit Crank-Nicholson method is used for time advancement. Unlike SIMPLE type methods, which are better suited for steady flows, the fractional step scheme proposed here enforces mass conservation at each time step, which is essential for unsteady flows.

3.2.0.2 Hardware Requirements and Additional Software

Traditionally, software has been written for serial computation (i.e. to be executed by a single computer having a single Central Processing Unit (CPU)). Problems are

solved by a series of instructions, executed one after the other by the CPU, where only one instruction may be executed at any moment in time. In the simplest sense, parallel computing is the simultaneous use of multiple computer resources to solve a computational problem. The computer resources can include a single computer with multiple processors, an arbitrary number of computers connected by a network, or a combination of both.

The computational problem usually demonstrates characteristics such as the ability to be broken apart into discrete pieces of work that can be solved simultaneously, and solved in less time with multiple computer resources than with a single computer resource. Ultimately, parallel computing allows for the solution of large CFD problems in reasonable time. The Numerical Wind Tunnel has been designed to operate in a parallel environment where the computational domain is distributed among a number of processors such that the number of computational cells dedicated to each processor is roughly equal.

In order to take advantage of this feature of the NWT, a suitable parallel environment is necessary. For the majority of this research a small 16 processor cluster located at Dalhousie University was made available and traffic was usually limited to one other user, also using 16 processors. Additionally, a recent partnership of seven academic institutions, including Memorial University of Newfoundland, University of New Brunswick, Mount Allison University, and the University of Prince Edward Island has resulted in the Atlantic Computational Excellence Network, or ACEnet for short. The goal of ACEnet is to create and operate high performance computing facilities interconnected by high-speed networks, allowing them to behave as a single, regionally distributed "computational power grid" of enormous capacity [1]. At the time of writing, the newly developed network is still experiencing "growing pains" and has not proven to be extremely useful to this research. The availability of suitable

cluster resources has been a limiting factor in the number of simulated time-steps achievable for this work, as well as the number of potential simulation cases to be studied.

In addition to the CFD code itself, there are additional pieces of software that must be installed and understood in order to use the NWT on multiple processors:

- MPICH (<http://www-unix.mcs.anl.gov/mpi/mpich/>) is the message-passing library used with NWT. It is the standard implementation for a wide variety of parallel and distributed computing environments and is the method by which processors communicate with each other.
- PARMETIS(<http://www-users.cs.umn.edu/karypis/metis/parmetis/>) is an MPI-based library that repartitions the mesh in parallel. The domain must be partitioned for parallel computing. In order to improve the efficiency of the parallel computing jobs, each processor should have an equal number of cells and the amount of data passed between processors should be minimized. In the NWT, this is accomplished using PARMETIS. It optimizes the redistribution cost versus the inter-processor communication cost and assigns new processor identifiers for each cell, based on an array of cell-centre connectivity supplied by NWT.
- OpenDX (<http://www/opendx.org>) OpenDx is a powerful program developed by IBM to visualize 2 and 3-dimensional data. Post-processing routines must be created in OpenDX format in order to interpret the results from the NWT.

Along with the NWT code, these programs are all open source and must be downloaded and installed in order for the code to function properly. For more information on the theoretical development of the Numerical Wind Tunnel, the interested reader is directed to thesis published by Bell [11].

3.3 Flow Past a Stationary Cylinder

The first step in simulating the motion of a cylinder undergoing vortex induced vibration is to simulate the flow field around a stationary cylinder. The following paragraphs describe the vortex shedding characteristics and structures that develop in the wake of a stationary cylinder at various Reynolds numbers.

3.3.1 Flow Structures in Wake

The pressure on a fluid particle increases from the free-stream to stagnation pressure as the leading edge of a cylinder is approached. The increased pressure impels the fluid over the cylinder and a boundary-layer develops. As the Reynolds number increases beyond 5, the pressure cannot force the flow around the trailing edge of the cylinder and the boundary-layer separates, forming two shear layers that bound the wake. The slower moving portion of the shear layers cause the shear layers to roll into the near wake and form swirling vortices. A regular pattern of vortices forms which is known as the vortex street. The behavior of flow structures in the wake of a cylinder depends on the state of the flow, which may be laminar, transitional, or turbulent. The transition from laminar to turbulent flow around bluff bodies is gradual and takes place over various regions of disturbed flow. These regions can be identified as the wake, shear layers, and boundary-layers. Figure 3.3, shows the transition in disturbed regions where BL, L, Tr and S refer to the boundary-layer, laminar, transition, and separation regions respectively.

The transition to turbulence first takes place in the wake, with the separated boundary-layers (free shear layers) remaining laminar. This is known as the TrW regime. As the Reynolds number is increased, the transition moves from the wake to the free shear layers towards the point of separation, and is called the TrSL regime.

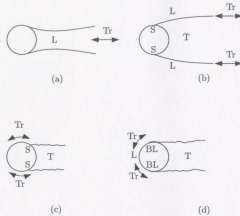


Figure 3.3: Transitions in disturbed regions: (a) TrW, (b) TrSL, (c), (d) TrBL

The transition then moves from the shear layers to the boundary-layers at separation (TrBL), and a drastic decrease in drag occurs due to the different flow structures resulting from the interaction between the separating layers and those undergoing transition to turbulence. The final stage of transition occurs as the boundary-layers become fully turbulent before the separation line and move towards the front stagnation point. This marks the end of the transitional flow regime and the flow is said to be fully turbulent. The major Reynolds number flow regimes for flow over a smooth circular cylinder are given in Table 3.1

3.3.2 Strouhal Number

The regular pattern of alternating vortices in the vortex street causes an oscillatory lift force perpendicular to the stream motion. The dimensionless frequency of vortex shedding is expressed as a Strouhal number, St :

$$St = \frac{f_s D}{U} \quad (3.1)$$

Table 3.1: Flow regimes over a smooth cylinder

Re	Description
< 5	Unseparated Flow
$5 - 15 \leq Re < 40$	Fixed pair of opposing vortices in wake
$40 \leq Re < 150$	Vortex street is laminar
$150 \leq Re < 300$	Transition to turbulence in wake (TrW)
$300 \leq Re < 3 \times 10^5$	vortex street is fully turbulent (TrSL)
$3 \times 10^5 \leq Re < 3.5 \times 10^6$	Laminar boundary-layer has undergone transition and wake is narrower and disorganized (TrBL)
$3.5 \times 10^6 \leq Re$	Turbulent vortex street is established

where f_s is the frequency of vortex shedding, D is the characteristic length (cylinder diameter), and U is the free-stream velocity of the fluid. Experiments have shown that the vortex shedding frequency is equal to the frequency of oscillation of the lift force and twice the frequency of the drag force (since the drag shedding frequency is influenced by both vortices as they are shed from the cylinder). The Strouhal number is a function of Re and to a lesser extent surface roughness and free stream turbulence [16]. The Strouhal number for a fixed rigid cylinder settles on a value of $St \simeq 0.21$ for Re outside of the transitional range of ($2 \times 10^5 < Re < 2 \times 10^6$). For smooth cylinders in the transitional range, however, the wake does not show periodic behavior and the Strouhal number may reach values as high as $St \simeq 0.5$ [4]. Finally, vortex shedding does not occur at a single frequency at high Reynolds numbers, but rather wanders over a narrow band of frequencies and is not constant along the span [65] of a fixed cylinder. According to Friehe [26] the distance over which force fluctuations along the span may be considered insignificant (the correlation length) for stationary cylinders is 5 diameters for fully turbulent vortex sheets and 3-4 diameters for transitional Reynolds numbers [32].

3.4 Flow-Structure Interaction

The aim of this research was to investigate the response of a cylinder undergoing vortex-induced vibrations in translation and rotation in a plane parallel to the cross-stream direction. There have been no published studies to determine to what extent the forces, responses, and vorticity dynamics of an elastically mounted body in a flow are modified by this motion. This research addresses these issues through a system of harmonic models used to simulate the response of the cylinder to its three-dimensional shed vortices. The details of the model are discussed further in Section 4.5, and some of the parameters important to the analysis of vortex induced vibrations are described in the following section.

3.4.1 Dimensional Analysis

The following non-dimensional terms have been found most useful in the analysis of subsonic vortex induced vibrations in a steady flow [16]:

1. Fineness ratio
2. Reduced velocity
3. Dimensionless amplitude
4. Mass ratio
5. Reynolds number
6. Damping factor
7. Turbulence intensity

The significance of these parameters is discussed in Chapter 2, and their definitions are given in the ensuing paragraphs.

The fineness ratio is defined as the ratio of the model length (l) to its width (D). When the length is specified as the third dimension, the parameter is known as the aspect ratio. Furthermore, the relative roughness is defined as the ratio of the surface roughness to the width.

$$\text{fineness ratio} = \frac{l}{D} \quad (3.2)$$

The reduced velocity is defined as the path length per cycle (given by U/f , where U is the free stream velocity and f is the oscillation frequency) divided by the model width. The maximum model width is often used in this parameter since it tends to govern the width of the wake.

$$\text{reduced velocity} = \frac{U}{fD} \quad (3.3)$$

The dimensionless amplitude is defined as the vibration amplitude (A_y), or one half of the path width, divided by the model width.

$$\text{dimensionless amplitude} = \frac{A_y}{D} \quad (3.4)$$

The mass ratio is used to measure of the tendency of a lightweight structure to experience VIV. It is defined as the ratio of the structural mass (m) to the displaced fluid mass and is given by:

$$\text{mass ratio} = \frac{m}{\frac{\pi}{4}\rho D^2} \quad (3.5)$$

where ρ is the density of the fluid.

The Reynolds number is a measure of the inertial forces to the viscous forces and may be used to determine whether a flow is laminar, turbulent, or in transition.

$$\text{Reynolds number} = \frac{UD}{\nu} \quad (3.6)$$

where ν is the dynamic viscosity of the fluid.

The damping factor, ζ , describes the energy dissipated by a structure as it vibrates and is given by:

$$\text{damping factor} = \zeta = \frac{\text{energy dissipated per cycle}}{4\pi \times \text{total energy of structure}} \quad (3.7)$$

Finally, the turbulence intensity is a measurement of the root mean square of the turbulence in a flow u'_{rms} to the free stream velocity.

$$\text{turbulence intensity} = \frac{u'_{rms}}{U} \quad (3.8)$$

3.4.2 Effect of Cylinder Motion on the Wake

As discussed in Chapter 2, the cylinder motion has large effect on vortex shedding. Some of the potential consequences of cylinder vibration are summarized below:

- Increased strength of vortices
- Increased span-wise correlation
- Lock-in or synchronization
- Increased mean drag
- Modified phase, sequence and pattern of vortices

The simulation of vortex induced vibrations on marine risers is very challenging and computationally expensive. Furthermore, simulations covering a large range of reduced velocities and industry relevant Reynolds numbers for large aspect ratio cylinders are impractical for the foreseeable future using present numerical techniques. For this thesis it was important to identify a major aspect of VIV modelling problem that had been accepted into practise but not challenged critically. Namely, the assumption that harmonic models (or experimental arrangements) that permitted only translation in the cross-stream and/or stream-wise direction were sufficient to predict the response of a cylinder to vortices shed at relatively high Reynolds number. In order to challenge this approach a modelling technique was developed that included a rotational component to account for the force variation along the span of a circular cylinder.

The ensuing chapters detail the code development necessary for this work, as well as the results of a series of simulations for the analysis of a circular cylinder undergoing VIV in both translation and rotation parallel to the cross-stream dimension, at a relatively high Reynolds number of $Re = 10^5$.

Chapter 4

Code Development for the Simulation of VIV

The work described in this thesis made use of the Numerical Wind Tunnel (NWT) platform developed at the Centre for Marine Vessel Development and Research at Dalhousie University [2]. In order to perform a simulation of vortex induced vibrations using the NWT, considerable code development was required. The following chapter describes some of the major contributions to the NWT necessary to study vortex induced vibrations on marine risers.

4.1 Surrounding Cells method

The surrounding cells method was developed for this research and is an algorithm for finding the cells and/or faces surrounding a given face or cell in a computational domain. The faces in the NWT are sorted into lists which makes it easy to propagate along the list, but advancing to another location is somewhat more difficult. Consider the cell shown in Figure 4.1.

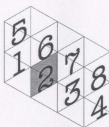


Figure 4.1: Simple grid

If the faces adjacent to the highlighted face #2 are desired, the list can be incremented or decremented to find face #1 and face #3. If, however, the face immediately above face #2 is desired, there is no way to immediately jump to that face. Many of the routines discussed in this section need information about the faces and cells surrounding a particular face; hence the requirement for the surrounding cells method. The method is described in more detail in section 4.2

4.2 Second-Order Velocity Interpolation

To implement the immersed boundary method a forcing function is added to the momentum equation as a body force. This equation, in integral conservation form, is given by Equation 4.1:

$$f^{i+1/2} = (\text{convective} + \text{viscous} + \text{pressure})^{i+1/2} + \frac{V^{i+1} - u^i}{\Delta t} \quad (4.1)$$

where the forcing function, f , ensures that the fluid velocity, u , is equal to the boundary velocity, V . Traditional immersed boundary simulations approximate the no-slip condition at a solid boundary by setting the fluid velocity at all faces inside the

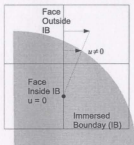


Figure 4.2: Traditional IB velocity interpolation on stationary boundary

boundary to zero (a first-order approximation). This method will not accurately resolve velocities at the cylinder surface unless the grid and immersed boundary are coincident, which is unlikely for curved surfaces. As shown in Figure 4.2 this approach can lead to non-physical values of the velocity at a solid surface, and a violation of the no-slip condition. The no-slip condition dictates that at a solid boundary the velocity of the fluid and the velocity of the boundary must be equal. For stationary objects this means that the fluid velocity must be zero at the surface of an object. The arrows in the figure represent velocity vectors and it is clear that at the cylinder surface the velocity is not zero. For most practical applications an interpolation scheme that is second order accurate is advisable, since it will improve the predictions obtained by a first-order method.

The simplest second order interpolation scheme is based on a linear interpolation of the face velocity, u_i inside the immersed boundary from the first face outside of it, u_o , and is given by Equation 4.2:

$$u_i = -\frac{h}{y}u_o \quad (4.2)$$

where y is the distance from u_o to the immersed boundary and h is the distance from u_i to the immersed boundary. An example of the linear interpolation scheme is shown

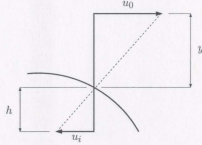


Figure 4.3: Second order linear interpolation

in Figure 4.3 and is applicable in all coordinate directions.

Figure 4.3 shows that the velocity at the solid surface is zero. While the interpolation is algebraically correct, if the distance from u_o to the immersed boundary is small, $\frac{h}{y}$ may become large and lead to numerical instability. In other words, if the external face paired with the IB face is too close to the boundary the IB velocity is forced to become very large and non-physical, which may lead to instability. To overcome the instability, Kim and Choi [41], recommend either using a face further away from the IB or a bilinear interpolation scheme.

The bilinear interpolation method has several advantages over the linear interpolation method. Namely, it is numerically more stable, allows for external faces close to the IB to be used, interpolates over three external faces, rather than one (or two), and interpolates over two directions rather than one. Figure 4.4 illustrates the bilinear interpolation method. The point (x_p, y_p) is where the no-slip condition is to be enforced, and $\bar{u}_1, \bar{u}_2, \bar{u}_3, \bar{u}_4$, are the face velocities surrounding point (x_p, y_p) .

The interpolation of the IB face velocity, U_1 is based on the following formula from Kim and Choi [41]:

$$U_1 = - \left[\alpha (1 - \beta) \bar{u}_2^k + (1 - \alpha) (1 - \beta) \bar{u}_3^k + (1 - \alpha) \beta \bar{u}_4^k \right] / \alpha \beta \quad (4.3)$$

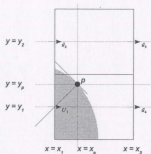


Figure 4.4: Second order bilinear interpolation

where $\alpha = (x_3 - x_p) / (x_3 - x_1)$, $\beta = (y_2 - y_p) / (y_2 - y_1)$. The scheme is similarly extended to all components of velocity.

In order to obtain the face velocities \tilde{u}_{1-4} , the surrounding cells method must be used, and it is now explained in more detail. A simplified flowchart is given in Figure 4.5 for two-dimensional flow from West to East. The first steps involve identifying a face inside the immersed boundary. This is accomplished by a simple algorithm that defines a line connecting the centre of the immersed boundary to each face in the computational domain. If the line crosses the boundary of the object an even number of times (including zero) then the face is considered inside the IB. Conversely, if the number of intersections is odd the face is outside.

If a face is inside the immersed boundary the cells to the east and west are identified as shown in Figure 4.6, where the face is denoted by f_1 and the cells to the West and East are given by c_1 and c_2 , respectively. For each of these cells, the cells to the North and South are identified, as shown in Figure 4.7 for cell c_2 .

With these cells identified it is possible to obtain the face information. Recall that it is not possible to move to the North and South directly from the faces, so the surrounding cells must be first identified so that the faces belonging to these cells may be used. The faces to the East and West of the surrounding cells are identified as shown in Figure 4.8 for cell c_{2b} .

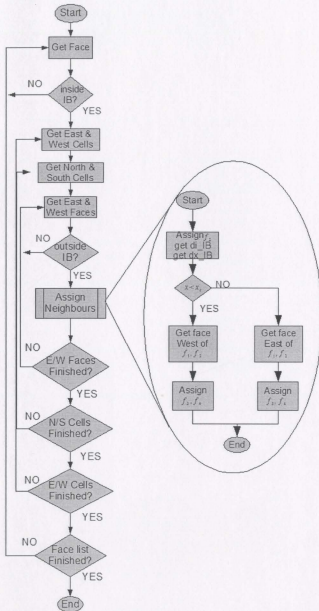


Figure 4.5: Simple surrounding cells flowchart

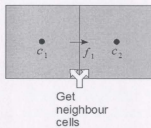


Figure 4.6: Identifying cells to East and West

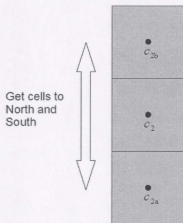


Figure 4.7: Identifying cells to North and South

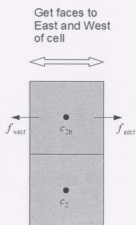


Figure 4.8: Identifying faces to East and West

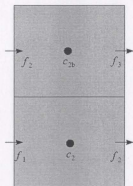


Figure 4.9: Identifying surrounding faces

If one of these faces is outside the immersed boundary it represents a suitable external face neighbor for the internal face. For the internal face and neighbor (f_1 and f_2) located east of the object centre, faces f_3 and f_4 are located east of f_1 and f_2 . Similarly, for f_1 and f_2 located west of the object centre, faces f_3 and f_4 are located west of f_1 and f_2 , as shown in Figure 4.9 for cells c_2 and c_{2b} .

With the surrounding faces identified, the velocity and the coordinates of each face are stored as well as the location of the point p . Point p is defined as the intersection of the wall-normal line passing through the location where the internal face velocity U_1 is defined, and the immersed boundary.

The 2nd order implementation assumes a linear relationship between cells. In order to use the routine effectively, it is therefore important to ensure that such a relationship is valid. Turbulent effects vanish very near a wall and the boundary-layer is dominated by viscous shear [80]. In the 1930s, the Law of the Wall was developed by Ludwig Prandtl and assumes that the dimensionless velocity, u^+ , is purely a function of the dimensionless wall distance, y^+ . He proposed the following:

$$u = f(\mu, \tau_w, \rho, y) \quad (4.4)$$

where u is the local fluid velocity, μ is the kinematic viscosity of the fluid, τ_w is the shear stress at the wall, ρ is the fluid density and y is the distance to the wall.

Dimensionless analysis gives

$$\frac{u\rho^{1/2}}{\tau_w^{1/2}} = f\left(\frac{y\rho^{1/2}\tau_w^{1/2}}{\mu}\right) \quad (4.5)$$

Prandtl then defined the following non-dimensional terms:

$$u^* = \sqrt{\frac{\tau_w}{\rho}} \quad (4.6)$$

$$u^+ = \frac{u}{u^*} \quad (4.7)$$

$$y^+ = \frac{yu^*}{\nu} \quad (4.8)$$

Substitution leads to the Law of the Wall :

$$u^+ = f(y^+) \quad (4.9)$$

The term u^* has the dimensions of velocity and is referred to as the friction velocity. It is a measure of the velocity gradient at the wall. The ratio of the local fluid velocity to the friction velocity is given by u^+ , and y^+ is a form of the Reynolds number, evaluated at a distance y from the wall, using the friction velocity. The inner part of the wall layer, very near the wall is called the *viscous sublayer*. The velocity profile is assumed linear in this region and experiments have shown that the linear distribution holds for $y^+ \leq 5$ [42]. For the 2nd order implementation to be valid, the interpolation must take place in the viscous sublayer, so a routine was written into the algorithm to calculate y^+ and determine the validity of the linear assumption. For flows in which

boundary-layer effects are important, it is generally accepted that the first grid point above the surface should be located at $y^+ \sim 1$ [8], [77], so this is generally not a problem for well resolved meshes.

4.3 Calculation of Lift and Drag Forces

When a fluid flows past an object an interaction between the body and the fluid occurs that can be described in terms of wall shear stresses (due to viscous effects) and normal stresses (due to the pressure). The resultant force in the direction of the upstream velocity is termed the drag, and the resultant force normal to the upstream velocity is termed the lift. The total drag and lift forces are obtained by integrating the differential drag and lift forces over the surface of the object, as shown in Equations 4.10 and 4.11

$$F_d = F_{p_x} + F_{v_x} = \int p \cos \theta dA + \int \tau \sin \theta dA \quad (4.10)$$

$$F_l = F_{p_y} + F_{v_y} = \int p \sin \theta dA + \int \tau \cos \theta dA \quad (4.11)$$

where p and v represent the pressure and viscous contributions in each of the coordinate direction shown in Figure 4.10 and F_d and F_l represent the forces of drag and lift, respectively.

For cylindrical surfaces at moderate Reynolds numbers it has been shown that the contribution to the lift and drag forces from shear stresses is minimal. For example, the contribution to the lift and drag force from shear stresses (F_{v_x} and F_{v_y} , respectively) can be approximated from the following equation from Munson [51]:

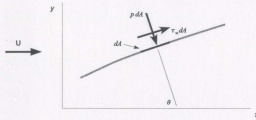


Figure 4.10: Differential lift and drag forces

$$F_{v_x} = \frac{\rho V_0^2 A}{2} \left(\frac{5.93}{\sqrt{Re}} \right) \quad (4.12)$$

$$F_{v_y} = \frac{\rho V_0^2 A}{2} \left(\frac{1.96}{\sqrt{Re}} \right) \quad (4.13)$$

For Reynolds numbers of 1×10^3 , 1×10^4 , 1×10^5 the ratio of friction (viscous) drag to the total drag is 0.14, 0.048, and 0.016 and the wall shear stress contribution to total lift is significantly smaller. For this work, the drag and lift forces are pressure dominated and the contribution of shear stress is therefore ignored.

The resultant of the pressure distribution is obtained by integrating the pressure values over the cylinder surface, so the lift force on a cylinder (F_l) is given by:

$$F_l(t) = \int p \sin \theta dA \quad (4.14)$$

and the lift coefficient (C_l) is calculated from:

$$C_l = \frac{2F_L(t)}{\rho V_0^2 A} \quad (4.15)$$

Similarly, the drag force (F_d) and drag coefficient (C_d) on a cylinder are given by equation 4.16 and 4.17, respectively:

Algorithm 1 Identifying surface cells

```

FOR each cell
  Get East Face
  IF face is inside IB
    get west face
    IF face is outside IB
      assign pressure, angle
    END IF
  END IF
  Get West face
  IF face is inside IB
    get east face
    IF face is outside IB
      assign pressure, angle
    END IF
  END IF
END FOR

```

$$F_d(t) = \int p \cos \theta dA \quad (4.16)$$

$$C_d = \frac{2F_D(t)}{\rho V_0^2 A} \quad (4.17)$$

In order to apply these formulae to the Numerical Wind Tunnel, significant code development was required. Figure 4.11 shows a simplified flowchart for the lift and drag integration routine.

Firstly, the cells at the surface of the cylinder had to be identified. This was accomplished via a modified version of the surrounding cells method. The routine needs information about each cell immediately outside the immersed boundary, but does not require information from the surrounding faces or cells. The pseudocode presented in Algorithm 1 describes the routine.

As shown in Figure 4.12, the situation may arise where a cell is located on a boundary, but neither face to the east or west is located outside. This algorithm must

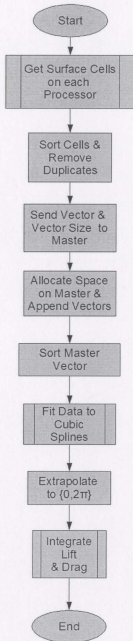


Figure 4.11: Simple lift and drag integration flowchart

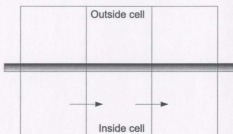


Figure 4.12: Boundary cell with both faces inside

also be run for cells in the north direction, where references to the east and west are replaced by north and south, respectively. This is necessary so that the cells adjacent to straight sections are identified.

The next step in the drag integration routine is to sort each cell according to the angle it makes with respect to the centre of the cylinder and the front stagnation point and remove any duplicate entries identified. This angle is termed θ_{stag} and the domain is generally divided amongst several processors. Vectors of pressure and θ_{stag} are created for each processor and sent to the main processor, where they are combined into a single vector and sorted according to θ_{stag} . The vector that resides on the master processor then contains pressure and θ_{stag} data for all of the cells surrounding the cylinder. A cubic spline routine was then developed to fit through the data contained on the master processor. This cubic spline was then integrated numerically over the cylinder surface to determine the lift and drag forces.

4.4 Quantifying the Induced Roughness

In the Immersed Boundary method, the no-slip condition is enforced at faces identified as being inside the immersed boundary (the IB faces). The true no-slip condition, however, exists at the surface of the immersed boundary, and rarely do the face and boundary coincide. This results in a staircase pattern, which essentially induces a

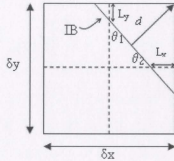


Figure 4.13: Determining roughness on immersed boundary

roughness on the immersed surface. For a staggered grid, the extent of this roughness can be approximated by the distance from the immersed boundary surface to the IB face in each of the coordinate directions.

Figure 4.13 illustrates the method for determining roughness where L_x and L_y represent the distance from the immersed face to the immersed boundary in the x and y coordinate directions, respectively, and the dashed lines indicate the centre-lines of the cell.

The roughness, then, is calculated based on the following formulae:

$$\theta_1 = \tan^{-1} \left(\frac{\frac{\partial x}{2} - L_x}{\frac{\partial y}{2} - L_y} \right) \quad (4.18)$$

$$\theta_2 = \tan^{-1} \left(\frac{\frac{\partial y}{2} - L_y}{\frac{\partial x}{2} - L_x} \right) \quad (4.19)$$

$$d = \frac{1}{2} \sqrt{\left(\frac{\partial x}{2} + \frac{L_y}{\tan \theta_2} \right)^2 + \left(\frac{\partial y}{2} + \frac{L_x}{\tan \theta_1} \right)^2} \quad (4.20)$$

When comparing rough and smooth cylinders, we notice an increase in the drag coefficient and a decrease in the Strouhal number for the rough cylinder. Bishop [14]

reported on a series of measurements of full-scale instrumented piles 0.48m and 2.8m in diameter and found that the maximum and minimum drag coefficient more than doubled the assumed drag coefficient when compared with similar smooth cylinders entering the drag crisis. Furthermore, while typical marine growth roughness ranges from 1 to 100mm [55], Sarpkaya [61] and Kasahara [38] found that a roughness as low as $\frac{\epsilon}{d} = 0.005$ resulted in a doubling of the drag coefficient. It can therefore be assumed that the drag coefficient on marine risers is heavily subject to the roughness imparted to them by the marine environment. Due to time constraints, the roughness algorithm was not validated against experimental or numerical benchmarks. However, it has provided a unique means of quantifying how well the Cartesian grid approximates an immersed boundary. Section 4.4.1 describes a manner in which this algorithm has been used to control the mesh in a CFD solution.

4.4.1 Controlling the solution with roughness approximation

The default grid adaptation method in the NWT uses a target number of cells or a constant adaptation criterion. Using a constant adaptation level can require a great deal of computer memory in the adaption routine and it is only possible to increase the value by a small amount at a time (or risk running out of memory). The target mesh method gradually adjusts the adaptation criteria by comparing the user-defined target with the actual number of cells in the computational domain. If the number of cells is less than the target, more refinement is required and the adaptation level is increased. Conversely, if the number of cells is greater than the target, the grid is coarsened.

Unfortunately, in the process of achieving the target number of cells the grid resolution near the immersed boundary may be coarsened, as the solution advances in time and a greater number of cells are required in the wake. In response to this the

Algorithm 2 Target Roughness Method

```

IF actual roughness > target roughness
    adaptation criterion = (adaptation criterion)/1.1
ELSE IF actual roughness < target roughness
    adaptation criterion = (adaptation criterion)*1.1
END IF

```

“target roughness” method was developed. The target roughness method compares the roughness value for the immersed boundary with a user-defined target roughness and adjusts the adaptation level as shown in Algorithm 2:

The result is that the number of cells around the immersed boundary remains relatively constant unless the target roughness is changed.

4.5 Accounting for the span-wise variation in forces along the cylinder span.

While vortex shedding on bluff bodies in the cross-stream and stream-wise directions has been described in a number of review papers over the past fifty years, the three dimensional nature of vortex shedding has received very little attention, despite the general agreement that cylinder wakes are three dimensional for Reynolds numbers greater than 150. In order to account for the force variation along the span of a cylinder, a rotational component should be introduced into the system of VIV equations traditionally used to model translation. The movement of the cylinder, therefore, is no longer confined to the principal axis, which may influence the prescribed motion.

For an arbitrary two-d.o.f. spring-mass-damper system, as shown in Figure 4.14, the coupled equations of motion are defined by

$$m\ddot{x} = F_v - F_1 - F_2 \quad (4.21)$$

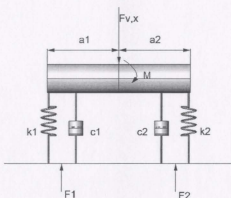


Figure 4.14: Arbitrary two degree of freedom spring-mass-damper system

$$I\ddot{\theta} = M_v + F_1 a_1 - F_2 a_2 \quad (4.22)$$

where F_v and M_v are the external force and moment on the system, while F_1 and F_2 are the interactive forces between the two d.o.f. spring-mass-damper system and a_1 , a_2 are the distances shown in Figure 4.14 .

In general, the equation of motion for a single spring-mass-damper can be written as:

$$m\ddot{y} + c\dot{y} + ky = F(t) \quad (4.23)$$

For the purposes of VIV, the following non-dimensional terms are introduced

$$\zeta = \frac{c}{2\sqrt{km}} \quad (4.24)$$

$$\frac{k}{m} = (2\pi f_n)^2 \quad (4.25)$$

$$U^* = \frac{U_\infty}{f_n D} \quad (4.26)$$

$$m^* = \frac{m}{\left(\frac{\pi}{4} \rho D^2\right)} \quad (4.27)$$

$$C_L(t) = \frac{2F_L(t)}{\rho U_\infty^2 A} \quad (4.28)$$

Substituting equation 4.24 and equation 4.25 into equation 4.23 gives:

$$m\ddot{y} + (4\pi\zeta f_n m)\dot{y} + (2\pi f_n)^2 m y = F(t) \quad (4.29)$$

and dividing equation 4.29 by m gives:

$$\ddot{y} + (4\pi\zeta f_n)\dot{y} + (2\pi f_n)^2 y = \frac{F(t)}{m} \quad (4.30)$$

Substituting equations 4.26, 4.27 and 4.28 into equation 4.30 and letting the system response force $F(t)$ be the lift force on the cylinder F_L

$$\ddot{y} + \left(\frac{4\pi\zeta}{U^*}\right)\dot{y} + \left(\frac{2\pi}{U^*}\right)^2 y = \frac{2}{\pi} \frac{C_L(t)}{m^*} \quad (4.31)$$

which is recognized as a suitable equation for describing the cross-stream response of a structure to vortex induced vibrations. This equation may be written compactly as:

$$\ddot{y} + c\dot{y} + ky = \frac{2C_L(t)}{\pi m^*} \quad (4.32)$$

where $c = \left(\frac{4\pi\zeta}{U^*}\right)$ and $k = \left(\frac{2\pi}{U^*}\right)^2$.

For multiple spring-mass-damper systems, equation 4.32 can be written as:

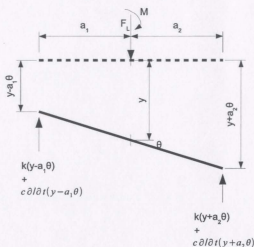


Figure 4.15: Free body diagram for multiple spring-mass-damper system

$$m\ddot{y} + \sum c_i \dot{y}_i + k_i y_i = F \quad (4.33)$$

and equivalently,

$$I\ddot{\theta} - \sum c_i \dot{y}_i a_i - \sum k_i y_i a_i = M \quad (4.34)$$

Returning to Figure 4.14, the free body diagram is shown in Figure 4.15 and the equations of motion for the cross-stream and rotational directions are:

$$m\ddot{y} + c y_1 + k y_1 + c y_2 + k y_2 = F \quad (4.35)$$

$$I\ddot{\theta} - c y_1 a_1 - k y_1 a_1 + c y_2 a_2 + k y_2 a_2 = M \quad (4.36)$$

Substituting $y_1 = y - a_1 \sin \theta$ and $y_2 = y + a_2 \sin \theta$ and assuming small amplitudes of oscillation ($\sin \theta \simeq \theta$), equations 4.35 and 4.36 may be written as

$$\begin{aligned}
 m\ddot{y} + c(\dot{y} - a_1\dot{\theta}) + k(y - a_1\theta) + \\
 c(\dot{y} + a_2\dot{\theta}) + k(y + a_2\theta) = F
 \end{aligned}
 \tag{4.37}$$

$$\begin{aligned}
 I\ddot{\theta} - c(\dot{y} - a_1\dot{\theta})a_1 - k(y - a_1\theta)a_1 + \\
 c(\dot{y} + a_2\dot{\theta})a_2 + k(y + a_2\theta)a_2 = M
 \end{aligned}
 \tag{4.38}$$

Equation 4.38 may be uncoupled by noting that $k_1a_1 = k_2a_2$ and $c_1a_1 = c_2a_2$ (i.e. $a = \text{Length}/2$):

$$m\ddot{y} + 2c\dot{y} - 2ky = F \tag{4.39}$$

$$I\ddot{\theta} + 2ca^2\dot{\theta} + 2ka^2\theta = M \tag{4.40}$$

This approach uses two springs and two dampers, each having coefficients that are half as large as the coefficients traditionally applied to risers. In terms of the traditional coefficients, equations 4.39 and 4.40 can then be written as:

$$m\ddot{y} + c\dot{y} - ky = F \tag{4.41}$$

$$I\ddot{\theta} + ca^2\dot{\theta} + ka^2\theta = M \tag{4.42}$$

Noting that equation 4.41 and equation 4.32 are equivalent, equation 4.42 is expanded by replacing the constants c and k with the well-known riser parameters and

substituting the equation for the moment of inertia of a cylinder rotated about its cross-sectional axis:

$$I = \left(\frac{mr^2}{4} + \frac{mL^2}{12} \right) \quad (4.43)$$

This equation can be generalized by substituting $r = \frac{L}{2A_r}$, where A_r is the aspect ratio (*Length/Diameter*), but for most cases $L^2 \gg r^2$, and equation 4.43 can be simplified to

$$I \approx \frac{mL^2}{12} \quad (4.44)$$

The moment can also be nondimensionalized by the moment coefficient.

$$M = \left(\frac{1}{2} \rho V_\infty^2 L^2 \right) C_m \quad (4.45)$$

Substituting the non-dimensional terms in equations 4.24 and 4.25 into equation 4.43 and dividing by m gives:

$$I\ddot{\theta} + (4\pi\zeta f_n) \left(\frac{L}{2} \right)^2 m\dot{\theta} + (2\pi f_n)^2 m \left(\frac{L}{2} \right)^2 \theta = \left(\frac{1}{2} \rho V_\infty^2 L^2 \right) C_m \quad (4.46)$$

In a manner analogous to the mass ratio, the inertia ratio is defined as the ratio of the body inertia to the inertia of the displaced fluid, and is given by:

$$I^* = \frac{I}{I_d} \quad (4.47)$$

The inertia term in equation 4.46 can therefore be replaced by $I = \frac{m_d L^2}{12} I^*$

which leads to

$$\ddot{\theta} + \frac{(4\pi\zeta f_n) \left(\frac{L}{2}\right)^2 m}{I^* \frac{L^2}{12} m_d} \dot{\theta} + \frac{(2\pi f_n)^2 m \left(\frac{L}{2}\right)^2}{I^* \frac{L^2}{12} m_d} \theta = \frac{\left(\frac{1}{2}\rho V_\infty^2 L^2\right)}{I^* \frac{L^2}{12} m_d} C_m \quad (4.48)$$

$$\ddot{\theta} + \frac{12(\pi\zeta f_n) m^*}{I^*} \dot{\theta} + \frac{12(\pi f_n)^2 m^*}{I^*} \theta = \frac{\left(\frac{1}{2}\rho V_\infty^2 L^2\right)}{I^* \frac{L^2}{12} m_d} C_m \quad (4.49)$$

Finally, substituting equation 4.27 into equation 4.49, the rotational response of a structure to vortex induced vibrations is given by:

$$\ddot{\theta} + \frac{12(\pi\zeta f_n) m^*}{I^*} \dot{\theta} + \frac{12(\pi f_n)^2 m^*}{I^*} \theta = \frac{24}{\pi I^*} C_m \quad (4.50)$$

Together with the rotational response given by Equation 4.50, the expressions for the cross-stream and stream-wise response are given by the following:

$$\ddot{y} + \left(\frac{4\pi\zeta}{U^*}\right) \dot{y} + \left(\frac{2\pi}{U^*}\right)^2 y = \frac{2}{\pi} \frac{C_L(t)}{m^*} \quad (4.51)$$

$$\ddot{x} + \left(\frac{4\pi\zeta}{U^*}\right) \dot{x} + \left(\frac{2\pi}{U^*}\right)^2 x = \frac{2}{\pi} \frac{C_D(t)}{m^*} \quad (4.52)$$

Figures 4.16 and 4.17 illustrate the potential influence of the rotational term on VIV motions. The equations of motion described by equations 4.51 and 4.50 were written into a Matlab routine and solved for various conditions using a fourth order Runge-Kutta method. The lift coefficient was described by:

$$C_l(t) = 0.7 \cos(t) \quad (4.53)$$

and the damping factor, mass ratio, and reduced velocity were set to 0.005, 1, and 5.0, respectively to promote large oscillations. The first case, shown in Figure 4.16 shows the displacement of the cylinder over 100 seconds when no moment is applied

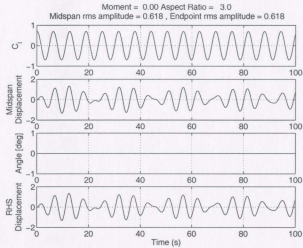


Figure 4.16: Displacement history for cylinder without span-wise lift moment

(i.e. the traditional approach). The results show a dimensionless r.m.s amplitude of 0.618.

Figure 4.17 shows the displacement of the cylinder when the moment coefficient was set to vary with the lift coefficient according to:

$$C_m(t) = 0.1 \cos(t) \quad (4.54)$$

This expression was chosen as a simple means of describing the variation of the moment coefficient over time, and served primarily to compare the motion of a body undergoing pure translation with a body undergoing translation and rotation. The results showed that the dimensionless r.m.s amplitude at the mid-span remained 0.618 (since the centroid of the cylinder was assumed to be located at the cylinder mid-span), and the r.m.s. amplitude at one end of the cylinder (denoted by RHS) increased to 0.798, which represented a 30% increase in amplitude due to the rotation of the cylinder. The maximum rotation angle was computed to be 20.4° and while this value is larger than that expected from a real riser (with larger mass and inertia ratios), it is

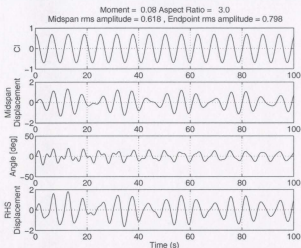


Figure 4.17: Displacement history for cylinder with moment varying with C_l

clear from the figures that a moment applied to the cylinder undergoing VIV behaved differently from the case of a cylinder with a uniform force distribution along the span. The shape and amplitude of the displacement curve, for example was altered significantly due to the combined effects of translation and rotation.

These figures show that an unsymmetrical distribution of lift forces along the cylinder span influenced the response of the cylinder when it was subjected to a sinusoidal lift force. In order to study the behaviour in more detail, numerical simulations were required, and are the focus of Chapter 7. The equations shown in equations 4.37 and 4.38 were implemented into the NWT and solved at each time-step using a 4th order Runge-Kutta routine. The location of the immersed boundary was then updated with the resultant displacements and the Cartesian mesh was refined to reflect the new location of the boundary.

Chapter 5

Modeling Generalities and Validation

5.1 Domain Size

Depending on the length of the cylinder in the span-wise direction, two calculation domains were used in this work. For the validation studies the computational domain, shown in Figure 5.1, was set to be 40 cylinder diameters in the stream-wise direction (x), 50 diameters in the cross-stream direction (z), and 0.5 diameters in the span-wise direction (y). For larger aspect ratios (i.e. for tests where the cylinder length is larger than 0.5 diameters) the domain was set to be $30D \times 30D \times 3D$. For all computational domains, the cylinder was located at the centre of the x and z planes and its axis spanned the extent of the domain in the y direction.

The blockage ratio can be defined as the ratio of the cylinder diameter to the height of the test section and the blockage effect is said to be negligible if this ratio is less than 3-5%. Anagnostopoulos et al. [6] have shown that larger blockage ratios tend to increase the separation angle and drag coefficient, and decrease the size of vortices. For this reason, all of the simulations in this work maintained a blockage ratio below 5%.

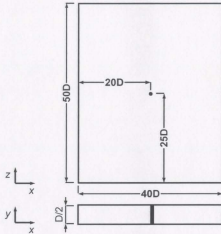


Figure 5.1: Calculation domain

In this research, the following cases were been studied for the simulation of vortex induced vibrations on marine risers.

- Stationary short cylinder at $Re = 100$ for 2nd order validation
- Stationary long cylinder at $Re = 10^5$
- Cross-stream translational VIV response of a cylinder with $L/D = 3$ at $Re = 10^5$
- Cross-stream translation and rotational VIV response of a cylinder with $L/D = 3$ at $Re = 10^5$ and $I^* = 1$
- Cross-stream translation and rotational VIV response of a cylinder with $L/D = 3$ at $Re = 10^5$ and $I^* = m^*$

5.2 Grid Independence Study

The method of performing a CFD simulation on two or more successively finer grids to examine the spatial convergence of a simulation is known as a grid convergence, or

grid refinement study. As the grid is refined and the time step is reduced the spatial and temporal discretization errors, respectively, should asymptotically approach zero, excluding computer round-off error. Roach [58] suggests a grid convergence index (GCI) for the reporting of grid independence studies in CFD. It is a measure of the percentage the computed value is away from the asymptotic numerical value, and indicates how much the solution would change with a further refinement of the grid.

The grid refinement ratio (r) is given in terms of the total number of elements used in the coarse (N_2) and fine (N_1) grids:

$$r = \left(\frac{N_1}{N_2} \right) \quad (5.1)$$

The theoretical order of grid convergence (p_c) is assumed to be equal to 2, or can be estimated from the solutions of three successively finer simulations (f_3 , f_2 , and f_1 , respectively).

$$p_c = \ln \left(\frac{f_3 - f_2}{f_2 - f_1} \right) / \ln(r) \quad (5.2)$$

The grid convergence index is defined as:

$$GCI_{fine} = \frac{F_s |\varepsilon|}{r^{p_c} - 1} \quad (5.3)$$

where F_s is a factor of safety and ε is the relative error, given by Equation 5.4.

$$\varepsilon = \frac{f_2 - f_1}{f_1} \quad (5.4)$$

A factor of safety of 3.0 is recommended for two-grid studies, and 1.25 for comparisons over three grids or more. It is important that each grid level yields solutions that are in the asymptotic range of convergence for the computed solution. This can be checked

by comparing the two GCI values computed over three grids.

$$\frac{GCI_{23}}{r^{p_c} GCI_{12}} \approx 1 \quad (5.5)$$

A value of Equation 5.5 that is close to unity indicates that the solutions are well within the asymptotic range of convergence. Finally, the value of the simulation variable at zero grid spacing can be estimated from Equation 5.6:

$$f_{exact} \simeq f_1 + \frac{f_1 - f_2}{r^{p_c} - 1} \quad (5.6)$$

The NWT uses anisotropic grid refinement on an unstructured Cartesian mesh, which means that the grid spacing, or number of cells in the simulation cannot be fixed a priori. The target anisotropic cell dimensions are given by Δx_{target} , Δy_{target} , and Δz_{target} , and are functions of the variables and/or derivatives at the cell centroid. The adaptation of the mesh is accomplished by comparing the actual cell dimensions to the target cell dimensions from equations 5.7, 5.8, and 5.9 and refining or coarsening appropriately.

$$\Delta x_{target} = \left(\frac{64c_{adapt}^2 F_{yy} F_{zz}}{F_{xx}^4} \right)^{\frac{1}{10}} \quad (5.7)$$

$$\Delta y_{target} = \left(\frac{64c_{adapt}^2 F_{xx} F_{zz}}{F_{yy}^4} \right)^{\frac{1}{10}} \quad (5.8)$$

$$\Delta z_{target} = \left(\frac{64c_{adapt}^2 F_{xx} F_{yy}}{F_{zz}^4} \right)^{\frac{1}{10}} \quad (5.9)$$

where c_{adapt} is the user specified error tolerance (grid adaptation criterion) and F_{xx} , F_{yy} and F_{zz} are the magnitudes of the second derivatives of velocity calculated at the cell centroid. The mesh density may be controlled by adjusting the value of the the

grid adaptation criterion and grid refinement study can therefore be undertaken by adjusting the value of c_{adapt} to produce coarse and dense meshes. All of the simulations presented in this thesis have been subject to a grid independence study. Due to the computational resources required some of the sensitivity studies have been more rigorous than others. The details of each grid independence study is presented with its respective simulation.

5.3 Validating the 2^{nd} -order Velocity Interpolation

In order to validate the 2^{nd} -order velocity interpolation, the flow over a circular cylinder at a Reynolds number of 100 was chosen as a benchmark case. This flow is characterized by a periodic laminar flow regime in which staggered eddies are not shed from the cylinder but rather initiate at the end of the closed near-wake. Furthermore, the roll-up of eddies is gradual until a 'fixed' pattern develops. Important aspects of this flow regime include:

- The eddy formation length. The distance from the base of the cylinder to the point of maximum vorticity is called the length of the eddy formation region (L_f). Beyond L_f viscous dissipation and diffusion gradually reduce the strength of eddies.
- The Strouhal number (see Section 3.3.2)
- Separation bubble size. As shown in Figure 5.2, the distance from the base of the cylinder to the point where the time-averaged stream-wise velocity is zero is given by L_b . This value is normalized by the cylinder diameter such that separation bubble size is given as L_b/D .

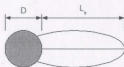


Figure 5.2: Illustration of separation bubble size

Table 5.1: Grid Convergence for 2nd-order Benchmark

Adaptation criterion	C_d	C_l	St	L_f	L/D	# cells
0	1.21	0.21	0.169	2.16	1.45	–
4E-05	1.21	0.21	0.168	2.12	1.44	25000
2E-04	1.21	0.20	0.164	1.90	1.35	10000

Two different grids were used, along with the method of grid convergence discussed in Section 5.2, to obtain grid independent results. The simulation was first carried out for 175 dimensionless time-steps in order for the wake and vortex street to become well established and average values of C_d , L_f and L/D were then computed over an additional 50 seconds. Over the same time-frame the root-mean-square of C_l was calculated as well as the Strouhal number. The results are presented in Table 5.1, where the values reported for an adaptation criteria of zero indicate the predicted value that would result for a perfectly refined mesh (i.e. with a grid spacing of zero).

It is clear that the lift and drag coefficients can be obtained using a fairly coarse mesh, but a finer mesh was necessary to obtain consistent values for the size of the separation bubble and eddy formation length, as shown in Figure 5.3. The simulation, therefore was assumed to be grid independent using an adaptation criterion of $4E-05$ with grid convergence indices ranging from 0.4% to 6%.

The power spectrum of the lift coefficient is shown in Figure 5.4, where there is a clear resonant peak at 0.168 Hz. This value is less than 2% larger than the experimental result of 0.165 obtained by Williamson [83] and less than 0.6% larger than the value of 0.167 reported by Roshko [59].

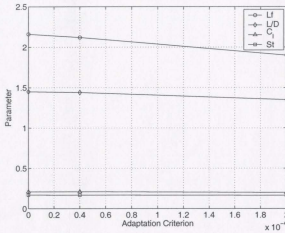


Figure 5.3: Grid Convergence Study at $R_e = 100$

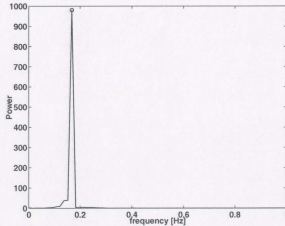


Figure 5.4: Single Sided Amplitude Spectrum of C_1 at $R_e = 100$

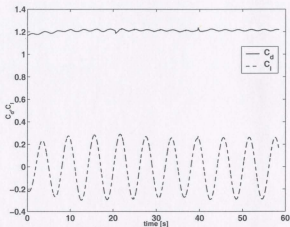


Figure 5.5: C_l and C_d vs time at $Re = 100$

Figure 5.5 shows the lift and drag coefficients computed over the last 50+ seconds of the simulation. The average drag coefficient of 1.2 and r.m.s lift coefficient of 0.21 compared well with the numerical values of 1.27 and 0.24 reported by So et al [70] and agree within 5% and 12%, respectively.

The size of the separation bubble averaged over the final 50s of the simulation was computed to be 1.44. This value is within 3% of the numerical result of 1.4 reported by Park et al. [56]. Finally, the length of the eddy formation region ($L_f = 2.12$) is within 8% of the curve fit through the works of Berger [13] and Nishioko and Sato [52] over a Reynolds number range of $60 \leq Re \leq 120$ presented by Zdravkovich [89]. For $Re = 100$ this curve gives a value of approximately $L_f = 2.3$.

Figure 5.6 and Figure 5.7 show the instantaneous vorticity and velocity contours for flow around a stationary cylinder at $Re = 100$. Qualitatively, the figure shows the classic pattern of stationary vortices in the wake of the cylinder and compares very well with the works of Kim [41] and Singh and Mittal [67]. Finally, an identical simulation was performed using the 1st order interpolation method with slightly less favorable results of $C_d = 1.2$, $C_l = 0.198$, $L/D = 1.45$, $L_f = 2.11$. The results from

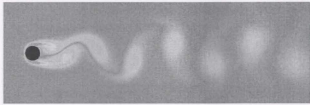


Figure 5.6: Vorticity contours for stationary cylinder at $Re = 100$

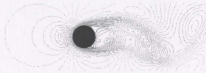


Figure 5.7: Velocity contours for stationary cylinder at $Re = 100$

the first order method give confidence in the strength of the overall code, and also demonstrate the improvements owing to the second order method.

Chapter 6

Simulation of Flow Past a Fixed Circular Cylinder at $Re = 10^5$

The first step in simulating the motion of a cylinder undergoing vortex induced vibrations was thought to be the simulation of the flow field around a stationary cylinder. When the flow field was established and in agreement with experimental/numerical observations, the cylinder was allowed to move in response to its shed vortices. The three-dimensional simulation of the flow of an incompressible fluid past a smooth circular cylinder at a Reynolds number equal to 100,000 is presented in this Chapter.

This flow has been studied numerically by a small number of researchers including Wang [78], Sampaio and Coutinho [60] and Breuer [18]. Wang et al. simulated the flow around a circular cylinder for $Re = 5 \times 10^5$ using a LES code with wall modeling. The simulated pressure coefficient compared well with the experimental work of Warschauer and Leene [79], but the drag coefficient was not captured. The predicted Strouhal number was in agreement with the work of Shih et al. [66] for a rough cylinder, but under predicted the results of Achenbach [3]. Sampaio and Coutinho [60] performed a 2D LES simulation for $Re = 10^4 - 10^6$ and found reasonably good agree-

ment with experimental work at $Re = 3 \times 10^5$, but concluded that finer grids and a fully 3-dimensional model was necessary to improve their results. Breuer [18] studied the applicability of LES for high Reynolds number flows and determined that grid-independent results for three-dimensional, time-dependent flows were a considerable challenge

The onset to transition to turbulence in boundary-layers develops slowly, and the flow at $Re = 10^5$ is known as the precritical regime [89]. This is a regime in which little transition takes place and the boundary-layers at the cylinder separate lamina-ly. The only transition to turbulence takes place in the free shear layers. Furthermore, as the Re is increased, the precritical regime is characterized by the gradual displacement of the separation point downstream and a gradual decrease in the lift and drag coefficients.

6.1 Computational Details

The computational domain for this simulation is shown in Figure 6.1. Periodic boundaries were imposed in the span-wise direction to minimize the effect of span-wise boundaries, and slip boundaries were imposed in the cross-stream direction. A uniform velocity of 1 m/s was specified at the inlet and the downstream boundary was prescribed by a convective outlet.

The span-wise length was set to be $3D$, sufficiently large to capture significantly large three-dimensional span-wise wake effects [20]. It was not possible to simulate larger lengths due to limited computational resources, and these simulations were performed using 16 processors in parallel.

Table 6.1: Computational Times for Numerical Simulation

Case Description	time steps	total simulated time	computational time
Transient	0-10k	17 s	80 days
Periodic	10k-21k	10 s	170 days
Moving	21k-28k	5 s	109 days

6.1.1 Computing Time

Table 6.1 summarises the computational time dedicated to the simulations presented in this thesis. At the beginning of the simulation (from step 0 to step 10,000) there was a period over which the flow was still developing and did not display periodic behaviour. This was labeled as the transient period and was not considered in the statistical analysis of time varying properties describing this flow. Steps 10,000 to 21,000 covered the range of periodic flow and provided the numerical results for flow over a stationary cylinder presented in this chapter. As shown in the table, these simulations required approximately 170 days to complete using 16 3GHz processors.

In order to ensure that all of the moving cylinder simulations started with a well established flow field, and that each had a common set of initial conditions, all of the moving cylinder simulations discussed in Chapter 7 began at the end of the periodic regime of the stationary cylinder (i.e. step 21001).

The computational expense of three-dimensional simulations at high Reynolds numbers is extremely (and sometimes prohibitively) high, due to the level of mesh refinement required. This, coupled with limited computer resources and time restrictions did not allow for a traditional grid independence study to be performed for these simulations. A new approach was therefore required to establish the grid sensitivity. It was decided to perform a grid independence study over three grids that were only one cell thick in the span-wise direction (essentially, a two-dimensional grid), but otherwise identical to the domain shown in Figure 6.1. Rather than tracking changes

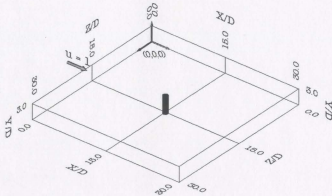


Figure 6.1: Computational domain for flow past stationary cylinder at $Re = 10^5$

in the results against the number of cells in the mesh, the grid adaptation criterion was chosen as the dependent variable in the grid refinement study. This parameter, discussed in section 5.2 specifies the tolerance for which the error across a given cell calls the automatic mesh refinement routine. Assuming that velocity fluctuations in the flow-field are largest in the wake of the cylinder, the domain in Figure 6.1 should also be grid independent for the same value of the grid adaptation criterion.

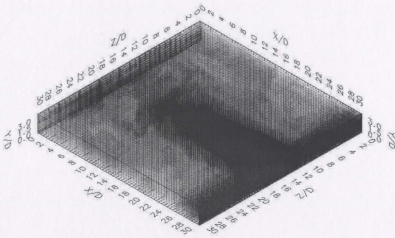
Three different grids were used, along with the method of grid convergence discussed in Section 5.2, to obtain grid independent results. Each simulation was started from rest and carried out for 30 dimensionless time-steps in order for the wake and vortex street to become well established. The average values of C_d and root-mean-square of C_l were calculated as well as the Strouhal number. The results are presented in Table 6.2, and the full analysis is presented in Appendix A.

According to the results of the grid independence study the simulation was assumed to be grid independent using an adaptation criterion of $4E - 05$ with grid

Table 6.2: Grid Convergence for flow over a Stationary Cylinder

Adaptation criterion	1E-03	2E-04	4E-05	0	Grid Convergence Index
C_d	1.03	1.14	1.17	1.18	1%
C_l	0.6	0.8	0.85	0.87	3%
St	0.183	0.211	0.214	0.214	0.6%
# Cells	8700	26500	75000	<i>inf</i>	<i>n/a</i>

convergence indices ranging from 0.6% to 3%. The domain shown in Figure 6.1 was therefore assumed to be grid independent for an adaptation criterion of $4E - 05$. Figures 6.2, 6.3, and 6.4 show the mesh used in this simulation. This mesh has been automatically refined according to the grid independence study, and shows that the grid density is greater in the wake of the cylinder than along the span. This means that assuming the refinement criterion is sufficient in the wake (as determined by the grid independence study), the variation in the span-wise direction will be sufficiently refined as well.

Figure 6.2: Refined mesh for flow past stationary cylinder at $Re = 10^5$

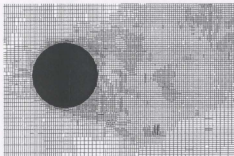


Figure 6.3: Refined mesh around cylinder for flow past stationary cylinder at $Re = 10^5$

6.2 Results

Figure 6.5 shows two cycles of the lift coefficient, along with the drag coefficient for this flow. The predicted r.m.s lift coefficient for the stationary cylinder was computed to be $C_{l,rms} = 0.54$, which is within 2% of the experimental work of Norberg [53] with $C_{l,rms} = 0.55$. The average drag coefficient for the stationary cylinder was $C_d = 1.15$, which is within 4% of the experimental measurements of Schewe [65] and Achenbach [3], who obtained time average drag coefficients of $C_d = 1.20$. Furthermore, the predicted Strouhal number of $St = 0.183$ is also within 4% of the simulated results of Chen [20] with $St = 0.190$, and 2% of Norberg's [54] empirical result of $St = 0.186$. Figure 6.6 shows the amplitude spectrum of lift, and confirms this value with a clear resonant peak at $St = 0.183$. The strong spikes in C_l and C_d do not correspond to the frequency of vortex shedding and cannot be linked directly to periodic flow features. They are likely the result of turbulent shedding at this Reynolds number.

6.2.1 Three-dimensional Effects

The simplest way to identify the three-dimensional characteristics of this flow is accomplished by visualizing the velocity vector and span-wise vorticity plots near the wake of the cylinder. The velocity vector plots at three different locations are shown

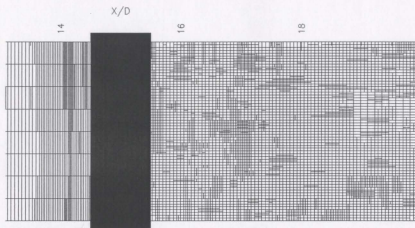


Figure 6.4: Refined mesh along span for flow past stationary cylinder at $Re = 10^5$

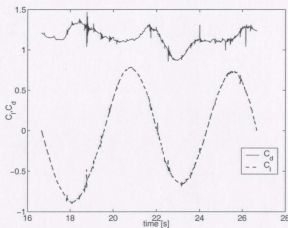


Figure 6.5: Coefficients of lift and drag for stationary cylinder at $Re = 10^5$

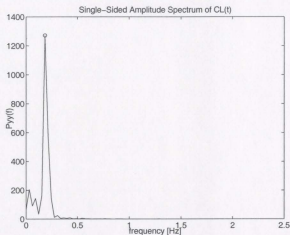


Figure 6.6: Amplitude spectrum of lift coefficient for stationary cylinder at $Re = 10^5$ in figures 6.7 , 6.8 and 6.9.

It is clear from the plots that the near wake velocity at $y = 0.5$ is different from that at the mid-span and at $y = 2.5$. In all of the plots vortices are shed alternately, but they do not remain in-phase along the span of the cylinder. At $y = 0.5$, for example, the vortex formed at the top of the cylinder appears to be much further developed at $y = 2.5$. This phase variation is evidence of the lack of similarity in the near wake and lends credence to the interpretation that the flow is three-dimensional [70].

Plots of span-wise vorticity at the locations specified by figures 6.7, 6.8 and 6.9 are shown in 6.10, 6.11 and 6.12. The vortex shedding pattern is such that in a cycle two vortices are released, one from the bottom and another from the top. This shedding behavior can then be identified as 2S, namely two single vortices. Although the shedding pattern remains 2S along the span of the cylinder, the nature and timing of shed vortices varies considerably.

This can perhaps be seen most effectively in the three-dimensional iso-surface

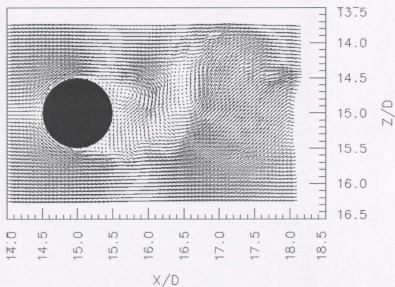


Figure 6.7: Velocity vectors for stationary cylinder at $Re = 10^5$, and $y = 0.5$

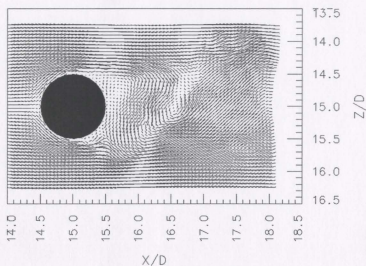


Figure 6.8: Velocity vectors for stationary cylinder at $Re = 10^5$, and $y = 1.5$

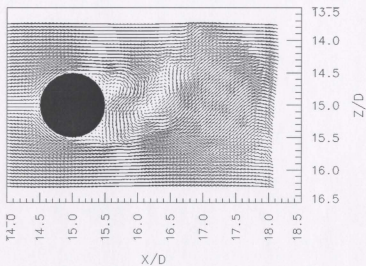


Figure 6.9: Velocity vectors for stationary cylinder at $Re = 10^5$, and $y = 2.5$



Figure 6.10: Vorticity contours for stationary cylinder at $Re = 10^5$, and $y = 0.5$

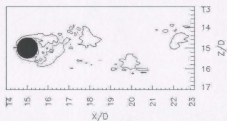


Figure 6.11: Vorticity contours for stationary cylinder at $Re = 10^5$, and $y = 1.5$

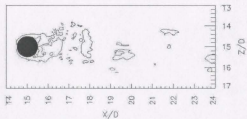


Figure 6.12: Vorticity contours for stationary cylinder at $Re = 10^5$, and $y = 2.5$

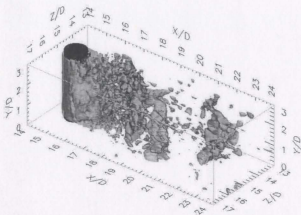


Figure 6.13: Instantaneous span-wise vorticity iso-surfaces for flow past stationary cylinder at $Re = 10^5$. Iso-surfaces $+2.0$ and -2.0

plot of span-wise vorticity shown in Figure 6.13. It is clear from the figure that vortices generated inside the riser boundary-layer are shed downstream and form coherent structures in the 2S pattern. The pattern persists along the span and an increasingly three-dimensional flow field develops downstream. Furthermore, the flow is not uniform along the span of the cylinder, which indicates that the flow around a circular cylinder at $Re = 10^5$ cannot be assumed to be two-dimensional. The three-dimensionality of the flowfield is examined in more quantitative terms later in this section.

Another important feature of a three-dimensional flow-field is the presence of oblique or parallel shedding modes. Williamson [84] and Luo et al. [44] showed that in the absence of free-stream shear and cylinder vibration, discontinuities in the $St - Re$ relationship at low Reynolds numbers were caused by the shedding of vortices at some oblique angle along the span. Figure 6.14 shows the instantaneous span-wise component of vorticity along a plane parallel to the midpoint of the cylinder (i.e.

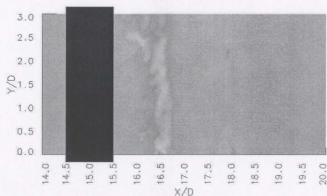


Figure 6.14: Span-wise vorticity in mid-plane of stationary cylinder at $Re = 10^5$ ($z = 15D$)

at $z = 15D$). The shedding appears to be slightly oblique and antisymmetric along the plane, which may be the cause (or consequence) of the time-lag between vortices. Also, Figure 6.15 shows a side view of the iso-surfaces shown in Figure 6.13 and reveals that the vortex structures in the far-wake become more symmetric about the span centre-line as the flow progresses.

It is clear from Figure 6.14 that there is only a single vortex cell within the span of the cylinder, which suggests that the frequency of vortex shedding may be constant. Figure 6.16 shows the lift coefficient over time at various span-wise locations. The calculated St number for each of these curves is indeed the same, which supports the claims of So et al. [70] that the St value is not a good indicator of three-dimensionality.

6.2.2 Correlation Coefficients

An effective way of quantifying the degree of three-dimensionality in a flow-field is by examining the spatial correlation along the span. The correlation coefficient, γ_{ij} ,



Figure 6.15: Instantaneous span-wise vorticity iso-surfaces for flow past stationary cylinder at $Re = 10^5$. Iso-surfaces $+2.0$ and -2.0

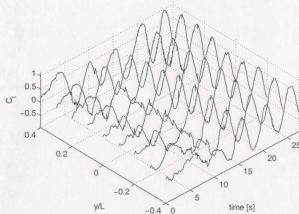


Figure 6.16: C_l vs time at $Re = 10^5$ along span of stationary cylinder

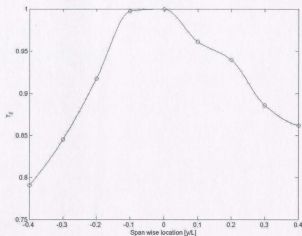


Figure 6.17: Cross correlation coefficient along span of stationary cylinder at $Re = 10^5$

indicates the strength and direction of a linear relationship between two random variables, and is given by [70]:

$$\gamma_{ij(\tau)} = \frac{\sum_t \{ [C_i(Y_i, t + \tau)] [C_j(Y_j, t)] \}}{\sqrt{\sum_t [C_i(Y_i, t + \tau)]^2} \sqrt{\sum_t [C_j(Y_j, t)]^2}} \quad (6.1)$$

where Y_i represents the spatial position along the span and τ represents the time delay between samples. In general terms, correlation refers to the departure of two variables from independence, and a value of γ_{ij} equal to unity indicates that the variables are perfectly correlated [46]. The coefficient γ_{ij} between the mid-span ($Y = 0$) and another location along the span at zero time delay ($\tau = 0$) is shown in Figure 6.17.

The figure shows that the lift force is most correlated near the mid-span, and becomes less and less correlated towards the ends of the cylinder. Furthermore, the flow is shown to be anti-symmetric about the mid-span. These results are consistent with the work of So et al. [70] for flow over a circular cylinder at $Re = 100$ and aspect ratio of 16.

Another measure of the three-dimensionality of a field is the span-wise correlation length, Λ , scaled by the cylinder diameter. There exists a correlation length over which the the force fluctuations in the wake may be described as perfectly correlated. Knowledge of Λ also has significance for vortex-induced vibration modeling since many empirical models use it as a modeling parameter, and it is important to identify the span-wise computational dimension to use in 3-D CFD codes to capture significant flow features. The correlation length can be computed by integrating the correlation coefficient over the cylinder length [9]:

$$\Lambda = \int_{-L/2}^{L/2} \gamma_{ij(z)} dz \quad (6.2)$$

The correlation length for this field was computed to be 2.7, which also compares reasonably well (within 13%) with the empirical formulas presented by Norberg [54]:

$$\Lambda = 2.6 \left(\frac{Re}{2.4 \times 10^5} \right)^{-0.2} = 3.1 \quad (6.3)$$

Despite the significance of the correlation length in three-dimensional fields, significant contributions at high Reynolds numbers are limited. The work described herein has contributed to this scientific knowledge base on the behavior of three-dimensional flow-fields at precritical Reynolds numbers on relatively low aspect ratio cylinders. Section 6.2.3 furthers this study through an investigation of the distribution of forces and moments along the cylinder span.

6.2.3 Span-wise Distribution of Force and Moment Coefficients

Figure 6.18 shows the variation of the r.m.s. lift coefficient along the span of the cylinder averaged over thirty dimensionless time steps. C_l increases from one end of the cylinder to the other and is obviously anti-symmetric about the mid-span. The

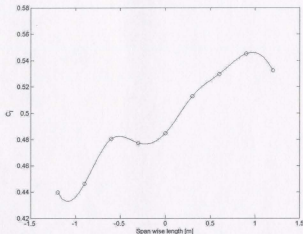


Figure 6.18: Distribution of lift coefficient along the stationary cylinder span at $Re = 10^5$

distribution of the drag coefficient along the span, averaged over the same time period is shown in Figure 6.19. In general, C_d reaches the extreme values near the ends of the cylinder, with the drag coefficient leveling off towards the central $L/2$ span. Similarly to Figure 6.18, the drag coefficient is also anti-symmetric about the mid-span, most likely due to the three-dimensionality of the wake.

The anti-symmetric force distribution imposes a moment about the cylinder. Assuming that the cylinder is uniform, the centroid is located at the midpoint of the cylinder, at a distance $L/2$ along the span. A resultant moment is obtained by summing the moments of the lift force over the cylinder span. Figure 6.20 shows the resultant moment coefficient C_m in the cross-stream direction, along with the corresponding lift coefficient plotted over time. The moment coefficient has peak values at around ± 0.05 and a root mean square value of $C_{m,rms} = 0.029$. It is clear that the moment coefficient and lift coefficient are operating at different frequencies. This implies that the spanwise location of the resultant moment arm is not stationary, and

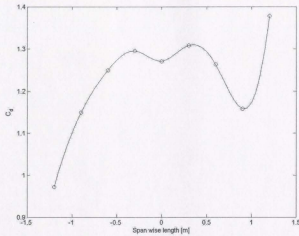


Figure 6.19: Distribution of drag coefficient along the stationary cylinder span at $Re = 10^5$

varies over time.

Figure 6.21 shows the amplitude spectrum of the moment coefficient, with a band of resonance from 0.09 to 0.25 Hz , with peaks located at 0.0916, 0.183, and 0.244 Hz .

To the author's knowledge, this moment coefficient investigation is unique to this thesis and has not been performed (or is not published in the literature) by other researchers. Aside from being a scientific curiosity, it is an important parameter in the code developed for this thesis, since the rotation angle computed by the code is a function of the moment coefficient supplied to it. Furthermore, this information would also be helpful in quantifying the magnitude and behaviour of the bending forces expected in the design of risers.

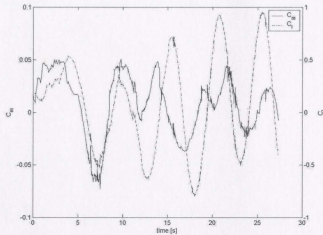


Figure 6.20: Moment coefficient and lift coefficient for stationary cylinder at $Re = 10^5$

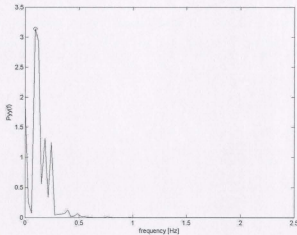


Figure 6.21: Amplitude spectrum of moment coefficient for stationary cylinder at $Re = 10^5$

Chapter 7

Simulation of 3D Flow Past an Elastically Mounted Cylinder Undergoing VIV

The majority of research into vortex-induced vibrations has been dedicated to the case of a cylinder vibrating in the transverse (cross-stream) direction. A single spring-damper system, located at the centre of the cylinder and shown in Figure 7.1, can be used to model this behavior numerically. As discussed in Chapter 2, there are very few papers reporting studies for the more practical case of vibration in the stream-wise and cross-stream directions (Figure 7.2), and even fewer for the case where there is variation of amplitude along the span of a body. For moving, rigid, cylinders, detailed measurements of cross-correlation between lift forces measured at the two ends of the cylinder can be found in Hover et al. [31]. In these experiments, the forces at each end of a rigid tapered and rigid uniform cylinder undergoing forced and free vibrations were measured for $Re = 3800$. They determined that the correlation coefficient was much higher in the case of forced oscillations, especially for the uniform cylinder. To



Figure 7.1: One degree of freedom spring-damper system

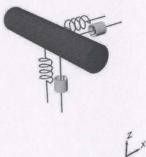


Figure 7.2: Two degrees of freedom spring-damper system (stream-wise and cross-stream)

date, an investigation into the response of a rigid cylinder to flow induced forces that vary along the span-wise direction has not been published. These are much more difficult to simulate numerically, especially at relatively high Reynolds number, and are the focus of this chapter.

7.1 Modelling Details

A model for this type of motion was introduced in Section 4.5, and the conceptual diagram is presented in Figure 7.3. The cylinder is supported by a pair of spring-damper systems in the cross-stream (Z) direction. The model can be easily adapted to include a pair of spring-dampers in the stream-wise direction as well, but it was decided to

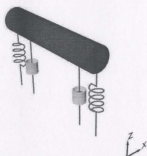


Figure 7.3: Two degrees of freedom spring-damper system (stream-wise and rotation)

determine the effect of cylinder rotation in one direction only, in order to clearly mark the effect of the rotation, and to limit complications. The methodology used for the implementation of harmonic models, however, remains the same irrespective of the plane(s) of rotation through which the cylinder is allowed to move.

The periodic flow-field produced by the stationary cylinder simulation was used as a starting point in the VIV simulation, and the moment induced by the lift forces, as well as the resultant lift and drag forces on the cylinder were input into the Runge-Kutta routines described previously. The cylinder position was then updated with the cross-stream displacements and rotational angle, and the flow-field was solved by the NWT. At each subsequent time step, the harmonic model was re-invoked and the LES flow simulation for the displaced cylinder was repeated until the target number of time steps was achieved. The flowfield produced by the stationary cylinder ensured that the grid was sufficiently refined at the onset of VIV motion, and reduced the likelihood of numerical divergence. While it is acknowledged that this may not be representative of natural VIV onset on an elastically mounted cylinder, the approach is consistent with the numerical approaches of Chen [20] and Bell [12] for the simulation of vortex-induced vibrations on cylinders.

These tests represented an opportunity to investigate how accurate the assumption

of a uniform force distribution, normally assumed in the prediction of VIV, is capable in predicting the wake vortex modes along the span, and hence VIV motion of a marine riser. The simulations are intended to demonstrate local flow features generic to cases having span-wise amplitude variations, and have therefore been designed to promote large amplitude oscillations. For values of the mass ratio parameter, $m^* < 6.0$, a new "super upper" branch with significant stream-wise and cross-stream amplitudes was discovered by Jauvtis and Williamson [36], and results are presented for $m^* = 2.6$. In one of the only LES simulations of vortex induced vibrations on risers at $Re = 10^5$, Chen [20] chose a damping ratio $\zeta^* = 0.005$ and reduced velocity $U^* = 6.055$ and modelled the VIV phenomenon using a single spring/dashpot system. In order to promote high amplitude motions, and provide a means of comparison with other numerical simulations the values of the mass ratio, damping ratio, and reduced velocity for this study were chosen to be the same ($m^* = 2.6$, $\zeta^* = 0.005$ and $U^* = 6.055$).

The simulated results presented in this chapter required considerable computational resources which precluded a long time statistical analysis. The results, therefore concentrate primarily on the behavior of the cylinder at the onset of vortex induced vibrations, and have been performed mainly using a 16 processor (3.6 GHz) PC cluster located at the Centre for Marine Vessel Development and Research at Dalhousie. Towards the end of this research the Atlantic Computational Excellence Network (ACEnet) was also used to perform simulations using 16, 2.6 GHz processors. The case of a cylinder undergoing vortex induced vibrations in the cross-stream direction was first investigated to determine the flow characteristics and establish a baseline for the remaining tests, which allowed the cylinder to translate and rotate in plane parallel to the cross-stream direction. The differences between the simulations, were therefore attributed to the rotation caused by a variable amplitude of vibration along

Table 7.1: Computational Times for Numerical Simulation of Moving Cylinder

Case Description	Cluster	time steps	time [days]
Translation	cmvdr1	21k-28k	117
Trans. + rot. ($I^* = 1$)	mahone	21k-28k	123
Trans + rot ($I^* = m^*$)	placentia	21k-28k	61

the span of the cylinder.

In order to ensure that all of the moving cylinder simulations started with a well established flow field, and that each had a common set of initial conditions, all of the moving cylinder simulations presented in this chapter began at the end of the periodic regime of the stationary cylinder (i.e. step 21001). Table 7.1 shows the computation times for each of the test cases presented in this thesis. The pure translation case (presented in section 7.2) was executed on the cmvdr1 cluster at Dalhousie (cmvdr1.me.dal.ca) for 117 days, using 16 3.6 GHz processors, and the cases for rotation and translation were executed using the AceNet resources described in section 3.2.0.2. Each of the simulations used 16 2.6 GHz processors, but the placentia (placentia.ace-net.ca) cluster produced results twice as fast as the mahone (mahone.ace-net.ca) cluster. This was mainly the result of decreased user activity on the placentia cluster, and an improved hardware configuration. Unfortunately, at the time of writing, the placentia cluster was still in development and required frequent shutdowns for hardware and software modifications, which limited it's effectiveness for this thesis.

7.2 Results for Cross-stream Translation Case

The simulation of vortex induced vibrations on a cylinder translating in the cross-stream direction is presented in this section in order to establish a baseline against which the effects of rotation (discussed in sections 7.3 and 7.4) may be measured.

Table 7.2 summarizes the VIV parameters used in these simulations.

Table 7.2: VIV parameters for cylinder translating in cross-stream direction

Parameter	Value
Re	10^5
U^*	6.055
ζ^*	0.005
m^*	2.65
I^*	n/a

Figure 7.4 shows the lift and drag coefficients at the onset of VIV for the case of a cylinder free to translate in the cross-stream direction (Figure 7.1). The lift coefficient undergoes a transitional period before settling into what appears to be a sinusoidal-type motion, with $C_{l_{rms}} = 3.37$. Over the same period, the drag coefficient reaches a maximum value of approximately 5 and an average value of 1.45. It is difficult, however, to see any trends in the lift and drag coefficients at this stage since the simulated time is not sufficient to compute long-time averages or obtain statistically steady results. As a point of comparison, however, Chen [20] obtained maximum values of $C_{l_{rms}} \sim 3.5$ and $C_d = 5.2$ for a cylinder free to translate in the stream-wise and cross-stream directions. It was difficult to compare time-series data in this manner, however, since the flow was transitional and statistical parameters could not be obtained.

7.2.1 Three Dimensional Effects

The three-dimensional characteristics of this flow near the wake of the cylinder at the mid-span and $0.5D$ from each end are shown in the velocity vector plots in Figures 7.5, 7.6, and 7.7. No clear vortex shedding pattern is obvious at this stage, and the figures look remarkably similar to each other along the span of the cylinder. This indicates that the wake of the cylinder is less three-dimensional than the case of the

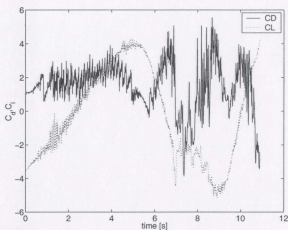


Figure 7.4: Coefficients of lift and drag for cylinder at $Re = 10^5$ oscillating in the cross-stream direction

stationary cylinder (Section 6.2.1) .

Three-dimensional iso-surfaces of velocity for this flow, presented in Figure 7.8, show that while there is some variation along the span of the cylinder, the flow is essentially behaving similarly along the cylinder.

To quantify the degree of three-dimensionality, the correlation coefficients (γ_{ij} , described in section 6.2.2) were computed, and are presented in Figure 7.9. Values of γ_{ij} near unity indicate that the lift coefficient is highly correlated along the entire span of the cylinder. Compared with the results presented for the stationary cylinder, it is clear that the forces along the cylinder span become more correlated when the cylinder is allowed to move in the cross-flow direction. This is an important result, because it supports the commonly held notion (as discussed in chapter 2) that the flow becomes two-dimensional once the cylinder is allowed to respond to it's shed vortices. Perhaps the uniform motion in the direction of the force organizes the wake and governs the flow. But the question remains as to whether this behaviour will continue as the cylinder is allowed to rotate and translate in the same plane. This is

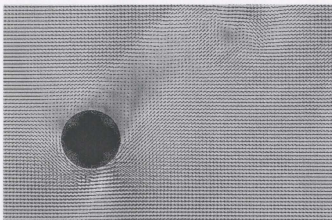


Figure 7.5: Velocity vectors at $y=0.5$ for cylinder at $Re = 10^5$ oscillating in stream-wise direction

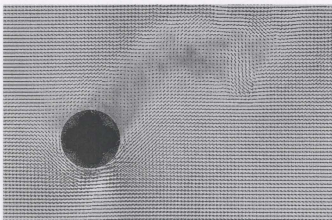


Figure 7.6: Velocity vectors at $y=1.5$ for cylinder at $Re = 10^5$ oscillating in stream-wise direction

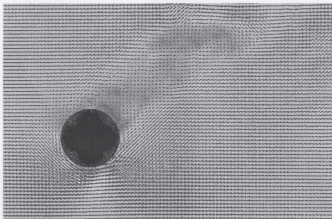


Figure 7.7: Velocity vectors at $y=2.5$ for cylinder at $Re = 10^5$ oscillating in stream-wise direction

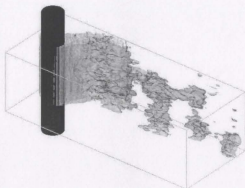


Figure 7.8: Instantaneous iso-surfaces stream-wise velocity for flow past a moving cylinder. Iso-surfaces $+0.5, 0.2$ and $-0.5, -0.2$

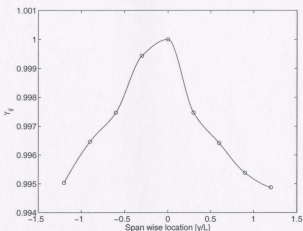


Figure 7.9: Cross correlation coefficient along span of cylinder translating in cross-stream direction at $Re = 10^5$

investigated further in the sections 7.3 and 7.4.

The correlation length, Λ , for this flow-field was computed to be 2.98, which indicates that the force fluctuations in the wake are perfectly correlated for essentially the entire length of the 3m cylinder. This value is higher than $\Lambda = 2.7$ computed for the stationary cylinder, thus providing further evidence of two-dimensionality in the flow field once the cylinder moves.

7.2.2 Span-wise Distribution of Force and Moment Coefficients

Figures 7.10 and 7.11 show the distribution of $C_{l_{rms}}$ and C_d over the length of the cylinder, averaged over time. C_l ranges from 3.35 to 3.38, and C_d ranges from 2.92 to 3.10, indicating that there is a 0.8 percent variation in lift and six percent variation in drag across the span of the cylinder. This is much lower than the twenty percent variation in C_l and thirty percent variation in C_d reported in Section 6.2.3 for the flow over a stationary cylinder, and represents increased uniformity along the cylinder span, and hence increased two-dimensionality.

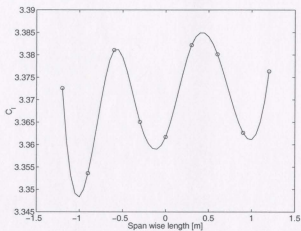


Figure 7.10: Distribution of r.m.s. lift coefficient along span of cylinder translating in cross-stream direction at $Re = 10^5$

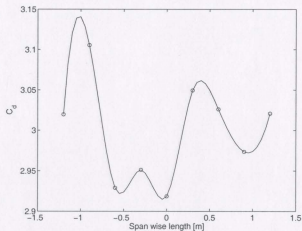


Figure 7.11: Distribution of drag coefficient along span of cylinder translating in cross-stream direction at $Re = 10^5$

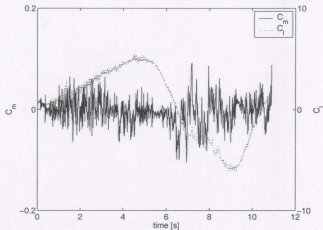


Figure 7.12: Moment and lift coefficients for cylinder at $Re = 10^5$ translating in cross-stream direction

Finally, the moment and lift coefficients for this flow are plotted in Figure 7.12. The moment coefficient has peak values at around ± 0.04 and a root mean square value of $C_{m,rms} = 0.018$. These values are smaller in magnitude than those reported for the stationary cylinder (with peaks of ± 0.05 and $C_{m,rms} = 0.029$). This is not surprising result in light the previous evidence of increased correlation.

7.3 Results for $I^* = 1$

The simulations for a cylinder translating and rotating with $I^* = 1$ is an exaggerated case, designed to promote very large angles of rotation, and hence large amplitude variation along the span of the cylinder. For a cylinder with $L/D = 3$ it was not possible to achieve large amplitude oscillations at the ends of the cylinder using the more realistic case where $I^* = m^*$ (discussed in section 7.4). To investigate the behaviour of a rigid cylinder experiencing large amplitude variations due to VIV, a cylinder with a very low inertia ratio ($I^* = 1$) was selected. The VIV parameters

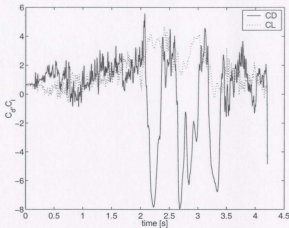


Figure 7.13: Coefficients of lift and drag for translating and rotating cylinder with $I^* = 1$ at $Re = 10^5$

relevant to these simulations are presented in Table 7.3.

Table 7.3: VIV parameters for case of $I^* = 1$

Parameter	Value
Re	10^5
U^*	6.055
ζ^*	0.005
m^*	2.65
I^*	1

Figure 7.13 shows the lift and drag coefficients at the onset of VIV for the case of a cylinder free to translate and rotate in a plane parallel to the cross-stream direction (Figure 7.3). The simulated time is not sufficient to compute long-time averages or obtain statistically steady results, but it is clear that the drag coefficient reaches a maximum value of about 6, and the lift coefficient reaches a value as high as 4. The drag coefficient has a minimum value of -8 , which implies that the rotating cylinder wake produced alternating low pressure regions on the upstream and downstream sides of the cylinder.

7.3.1 Three-dimensional effects

Figure 7.14 shows the velocity contours at the mid-span of the cylinder, and in order to visualize the three-dimensional characteristics of this flow near the wake of the cylinder, velocity vectors at the mid-span and $0.5D$ from each end are shown in Figures 7.15, 7.16, and 7.17. The vortex shedding pattern is governed by the rotation of the cylinder (20.9 degrees at this timestep) and is most apparent at the extremities. The plots were each prepared at the same computational time-step, and the flow varies considerably along the span, as vortices shed from the cylinder in the the negative cross-stream direction (at $y = 0.5$) are shed in the positive direction at the other end. As shown in Figure 7.18, the vortex shedding pattern at the mid-span shows a pair of co-rotating vortices. In the literature, this is known as the 2C pattern and has been identified by Flemming and Williamson [25] in experiments on a cylinder pivoting about a pin connection at the top of the span at $Re \approx 1200$. The 2C pattern does not appear to persist along the span of the cylinder, and is likely affected by the large amplitude translations of the ends of the cylinder, which are much larger than the mid-span translations, due to the cylinder's angle of rotation.

Instantaneous surfaces of stream-wise velocity are shown in Figure 7.19, where the red and blue surfaces represent $u = 0.2m/s$ and $u = -0.2m/s$, respectively. The figure shows three structures at the ends of the cylinder blending together as the cylinder mid-span is approached. In order to further understand the vortex pattern along the span of the cylinder, a conceptual model of the vortex structure was developed.

Figure 7.20 shows the principal three-dimensional vortex structures constructed from cross-sectional measurements of vorticity along the span of the cylinder. At the mid-span, one of the co-rotating vortices evolves into a pair of counter-rotating vortices, thus producing a 2C-(2P+S) antisymmetric hybrid mode across the span of the cylinder. This is essentially a new mode of vortex shedding not previously

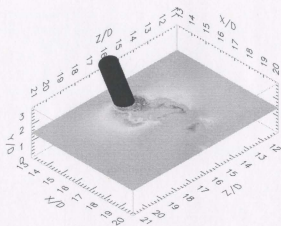


Figure 7.14: Velocity contours for moving and rotating cylinder at $Re = 10^5$, $I^* = 1$ and $y = 1.5$

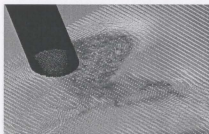


Figure 7.15: Velocity vectors for moving and rotating cylinder with $I^* = 1$ at $Re = 10^5$, and $y = 0.5$

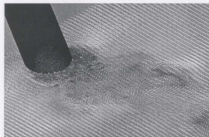


Figure 7.16: Velocity vectors for moving and rotating cylinder with $I^* = 1$ at $Re = 10^5$, and $y = 1.5$

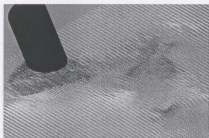


Figure 7.17: Velocity vectors for moving and rotating cylinder with $I^* = 1$ at $Re = 10^5$, and $y = 2.5$

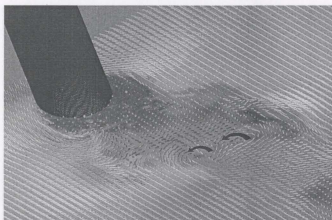


Figure 7.18: Velocity vectors showing 2C pattern for moving and rotating cylinder with $I^* = 1$ at $Re = 10^5$, and $y = 2.5$

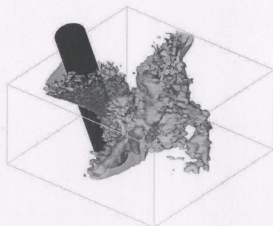


Figure 7.19: Instantaneous iso-surfaces stream-wise velocity for flow past a moving and rotating cylinder with $I^* = 1$ at $Re = 10^5$. Iso-surfaces $+0.2$ and -0.2 m/s

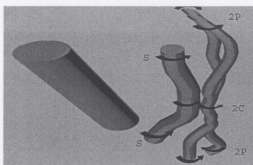


Figure 7.20: 3-D model of vortex shedding from moving and rotating cylinder with $I^* = 1$ at $Re = 10^5$

identified in the literature. An investigation into the parameters influencing this mode, such as reduced velocity, Reynolds number, and range of inertia ratios, would be useful, but would involve extreme computational time.

In order to quantify the degree of three-dimensionality in this flow-field, the correlation of lift across the span was computed and the results are shown in Figure 7.21. The figure shows that there is virtually no correlated region except for the very narrow region around $y/L = 0$. In the central region, the data points decrease from 1 to about 0.244 for $-y/L$, and from 1 to about -0.013 for positive y/L , and indicate a degree of symmetry in the flow-field. This is in direct contrast to the correlation coefficients presented for the stationary cylinder in Section 3.3, which showed higher correlation across the span but less symmetry. Also, the assumption of two-dimensionality is clearly not appropriate for cylinders experiencing this degree of rotation.

The correlation length, Λ , for this flow-field was computed to be 1.06. This indicates that the length over which the force fluctuations in the wake may be described as perfectly correlated is much smaller for the case of a moving (and rotating) cylinder compared to a stationary cylinder, at least at the onset of motion. The rotational component of this flow is most likely the greatest contributor to the reduction in Λ , since it was shown in Section 7.2 that VIV motion becomes more two-dimensional

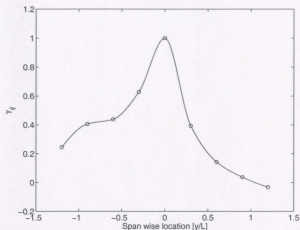


Figure 7.21: Cross correlation coefficient along span of moving and rotating cylinder with $I^* = 1$ at $Re = 10^5$

when cylinders are restricted to pure translatory motion.

7.3.2 Span-wise Distribution of Force and Moment Coefficients

Figure 7.22 shows the variation of the r.m.s. lift coefficient along the span of the cylinder at the onset of VIV. C_l decreases from the ends of the cylinder towards the minimum value near the middle of the cylinder, and shows some symmetry about the mid-span. The distribution of the drag coefficient along the span, averaged over the same time period is shown in Figure 7.23. In general, C_d reaches the extreme values near the ends of the cylinder, with the drag coefficient reaching a minimum value slightly to the positive side of the central region at $y/L = -0.05$. Similarly to Figure 6.18, the drag coefficient shows some symmetry along the span, with variances most likely due to the three-dimensionality of the wake. These figures differ in shape and magnitude from similar plots for the stationary cylinder, and support the previous finding that the flow-field becomes more symmetric at the onset of vortex induced vibrations.

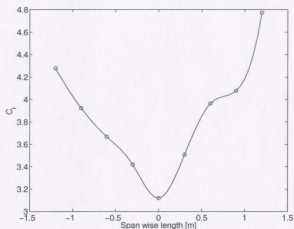


Figure 7.22: Distribution of r.m.s lift coefficient along span of the moving and rotating cylinder with $I^* = 1$ at $Re = 10^5$

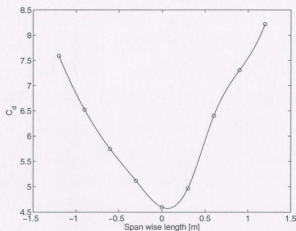


Figure 7.23: Distribution of drag coefficient along span of the moving and rotating cylinder with $I^* = 1$ at $Re = 10^5$

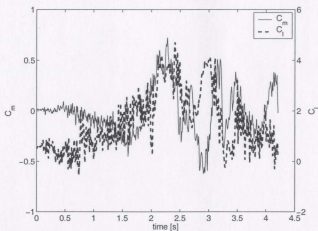


Figure 7.24: Moment coefficient and lift coefficient for moving and rotating cylinder with $I^* = 1$ at $Re = 10^5$

The lift force distribution shown in Figure 7.22 imposes a moment about the cylinder. Figure 7.24 shows the resultant moment coefficient C_m , along with the corresponding lift coefficient at the onset of VIV. The moment coefficient has peak values of ± 0.44 and a root mean square value of $C_{m,rms} = 0.21$. So, while the force distribution appears to be more symmetric about the cylinder, the moment coefficient is much larger, due to the increased r.m.s. values of the lift coefficient, compared to similar results for the stationary cylinder. It is difficult to determine if there is a decreasing trend in the value of the moment coefficient over time, since there is insufficient simulated time upon which to perform a statistical analysis. In order to identify long term trends in the moment coefficient during VIV, several cycles of vortex shedding are necessary. This, however, would require much greater computational resources than were available at the time of this research. Similarly to the case of the stationary cylinder, an investigation into the behavior of the moment coefficient along the span of a cylinder undergoing translation and rotation is unique to this thesis and has not been published by other researchers.

These simulations provide an exaggerated response of the cylinder in order to promote large amplitude variation along the cylinder span. Not only does this allow for a well defined interpretation of the flow in the wake of the cylinder, but the large amplitudes of displacement may be more realistic for longer cylinders, even if the rotation angle is small, which means that the vortex shedding away from the mid-span may be similar. The following section describes the more realistic case of a uniform cylinder with $I^* = m^*$.

7.4 Results for $I^* = m^*$

This simulation of vortex induced vibrations on a cylinder free to translate and rotate with it's inertia ratio equal to it's mass ratio is presented in this section. This is a more realistic value of the inertia ratio for a uniform cylinder, since if the mass is uniformly distributed along the span it follows from equation 4.44 that:

$$I^* = \frac{I}{I_d} = \frac{\left(\frac{mL^2}{12}\right)}{\left(\frac{m_d L^2}{12}\right)} = \frac{m}{m_d} = m^* \quad (7.1)$$

For this simulation, the cylinder is free to translate and rotate in the cross-stream direction as shown in Figure 7.3 and the VIV parameters relevant to the simulation are presented in Table 7.4

Table 7.4: VIV parameters for case of $I^* = m^*$

Parameter	Value
Re	10^5
U^*	6.055
ζ^*	0.005
m^*	2.65
I^*	2.65

Figure 7.25 shows the lift and drag coefficients at the onset of VIV for the case

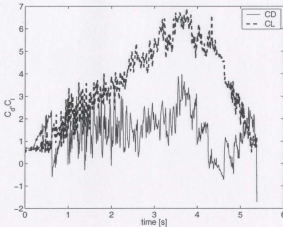


Figure 7.25: Coefficients of lift for translating and rotating cylinder at $Re = 10^5$ and $I^* = m^*$

of a cylinder with its inertia ratio equal to its mass ratio. The r.m.s lift coefficient reaches values of ± 3.9 which is larger than the case for $I^* = 1$, and the case for pure translation described in Section 7.2. Similarly to those other cases, it is difficult to identify any trends in the lift coefficient at this stage since the simulated time is not sufficient to compute long-time averages or obtain statistically steady results. Over the same period, the drag coefficient reaches a maximum value of approximately $C_d = 4$ and an average value of 1.4. These values are slightly less than those predicted for the case of pure translation discussed in 7.2. Furthermore, the peak value of the drag coefficient in the upstream direction is approximately -1, much smaller than -8 predicted for a cylinder translating and rotating with $I^* = 1$.

7.4.1 Three-dimensional effects

The three-dimensional characteristics of this flow near the wake of the cylinder at the mid-span and $0.5D$ from each end are shown in the velocity vector plots in Figures 7.26, 7.27, and 7.28. The flow pattern varies along the span, but not nearly as much

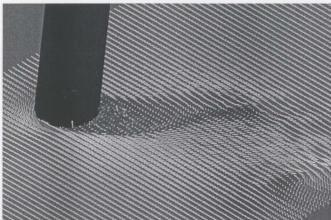


Figure 7.26: Velocity vectors for cylinder at $Re = 10^5$ and $I^* = m^*$, at $y = 0.5$

as for the case of $I^* = 1$. Moreover, the vortex shedding pattern is less dramatic, but also shows a small pair of co-rotating vortices at the mid-span (highlighted in Figure 7.29), and hints of it near the extremities. In contrast to the plots shown for the case of $I^* = 1$, the 2C pattern appears to persist along the span of the cylinder, most likely due to the fact that the rotation angle is much smaller for the case of $I^* = m^*$ and the flow is less affected by the translation of the ends of the cylinder.

Three-dimensional iso-surfaces of velocity for this flow, presented in Figure 7.30, show that there is variation along the span of the cylinder, but the effect of cylinder rotation is not as apparent as for the case of $I^* = 1$.

A comparison of the rotation angles at the onset of VIV is presented in Figure 7.31 for the case of a cylinder with $I^* = 1$ and $I^* = m^*$. It is clear from the figure that much smaller rotation angles exist when an object's inertia ratio is equal to its mass ratio, at least for the case of $m^* = 2.6$. For longer cylinders, the small rotation angles would result in increased amplitudes of motion at the ends of the cylinder, due to

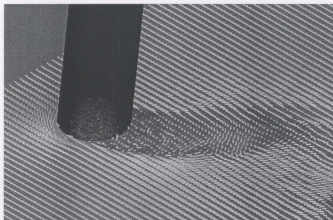


Figure 7.27: Velocity vectors for cylinder at $R_e = 10^5$ and $I^* = m^*$, at $y = 1.5$

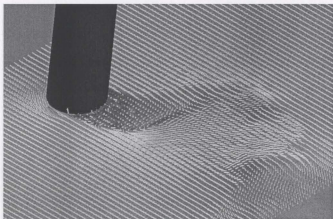


Figure 7.28: Velocity vectors for cylinder at $R_e = 10^5$ and $I^* = m^*$, at $y = 2.5$

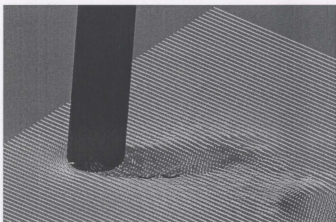


Figure 7.29: 2C pattern for cylinder at $Re = 10^5$ and $I^* = m^*$, at $y = 1.5$

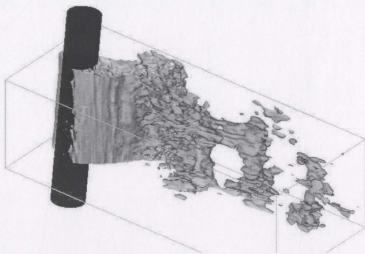


Figure 7.30: Instantaneous iso-surfaces of stream-wise velocity for flow past a moving cylinder with $I^* = m^*$. Iso-surfaces $+0.5, 0.2$ and $-0.5, -0.2$ m/s

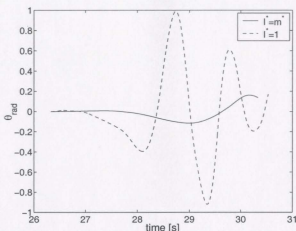


Figure 7.31: Comparison of rotation angles for cylinder at $Re = 10^5$ for $I^* = 1$ and $I^* = m^*$

simple trigonometry. As discussed in Section 7.3, large rotation angles were required in order to study the effects of large amplitude vibrations at the ends of the cylinder on the flow. The variation in amplitude may contribute to the vortex shedding pattern and result in the 2C-(2P+S) hybrid mode. It is also clear from the figure that the period of rotation for the cylinder with $I^* = m^*$ is about twice that for the case of $I^* = 1$. This is most likely due to the influence of the rotation angle on the flow.

A comparison of the dimensionless amplitudes at the cylinder mid-span at the onset of VIV is presented in Figure 7.32 for the case of a translating and rotating cylinder with $I^* = 1$, $I^* = m^*$ and also for the case of pure translation. The largest peak amplitude is found for pure translation, followed by $I^* = 1$ and $I^* = m^*$. Furthermore, the period of motion is shortest for the case of $I^* = m^*$. A similar plot is shown in Figure 7.33 for the cross-stream velocities. The results show that the cross-stream velocity reaches the largest values for $I^* = 1$ followed by $I^* = m^*$ and is smallest for the case of pure translation.

The correlation coefficients along the span of the cylinder with $I^* = m^*$ are pre-

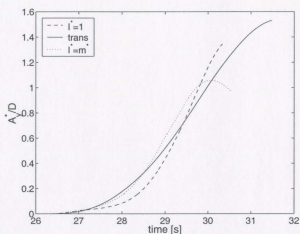


Figure 7.32: Comparison of amplitude ratios for cylinders at $Re = 10^5$ for $I^* = 1$ and $I^* = m^*$ and pure translation

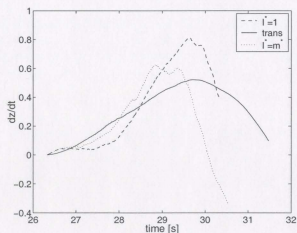


Figure 7.33: Comparison of cross-stream cylinder velocities ratios for translating and rotating cylinder at $Re = 10^5$ for $I^* = 1$ and $I^* = m^*$

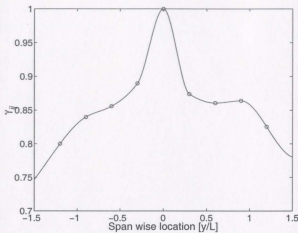


Figure 7.34: Cross correlation coefficient along span of moving cylinder at $Re = 10^5$ for $I^* = m^*$

sented in Figure 7.34 . There is a narrow region of highly correlated flow at the cylinder mid-span and less correlation towards the ends of the cylinder. The correlation length, Λ , for this flow-field was computed to be 2.6, which indicates that the force fluctuations in the wake are perfectly correlated for about eighty-five percent of the length of the cylinder. This value is only slightly lower than $\Lambda = 2.7$ computed for the stationary cylinder, thus indicating that for cylinders with $I^* = m^*$ the onset of vortex induced vibration does not affect the magnitude of the correlation length, although it clearly alters the flow behaviour.

A comparison of the correlation coefficients for all of the cases discussed in this thesis are presented in Figure 7.35. It is clear that the forces along the cylinder span become more correlated when the cylinder is allowed to move in the cross-flow direction. For a cylinder rotating with $I^* = m^*$ the correlation resembles that of the stationary cylinder in terms of magnitude and shape, but contains a more narrow band of highly correlated flow. The exaggerated motion of the cylinder with $I^* = 1$ is mostly uncorrelated, as described previously.

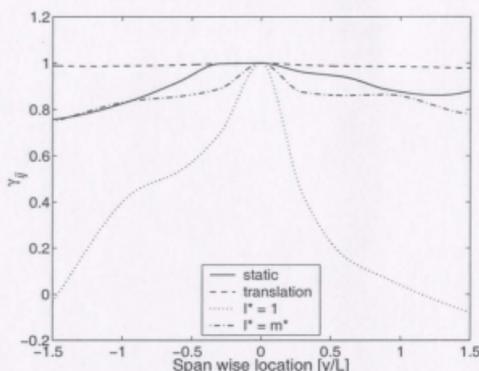


Figure 7.35: Cross correlation coefficient along span of moving cylinder at $Re = 10^5$

7.4.2 Span-wise Distribution of Force and Moment Coefficients

Figures 7.36 and 7.37 show the distribution of C_l and C_d over the length of the cylinder. C_l ranges from about 4.3 to 4.8, and C_d ranges from 3.7 to 4.1, indicating that there is a ten percent variation in both lift and drag across the span of the cylinder. This is less than the twenty percent variation in C_l and thirty percent variation in C_d reported in Section 6.2.3 for the flow over a stationary cylinder. The values of C_l and C_d indicate an increase in the lift and drag coefficients at the onset of VIV. Furthermore, the shape of the lift coefficient distribution curve is similar to that of the stationary cylinder (shown in Figure 6.18), in that the flow is anti-symmetric about the mid-plane, and increases from one end of the cylinder to the other. The shape of the drag coefficient curve does not resemble the drag curve for the stationary cylinder (shown in Figure 6.19)

Finally, the moment and lift coefficients for this flow are plotted in Figure 7.38. The values of the moment coefficient are larger than those reported for the stationary cylinder, due to the increase in the lift coefficient. At the onset of motion the moment

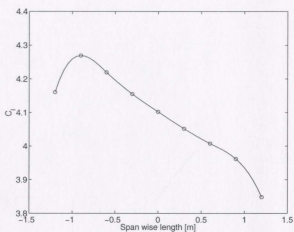


Figure 7.36: Distribution of lift coefficient along span of moving cylinder at $Re = 10^5$ for $I^* = m^*$

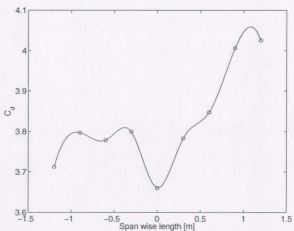


Figure 7.37: Distribution of drag coefficient along the moving cylinder span at $Re = 10^5$ and $I^* = m^*$

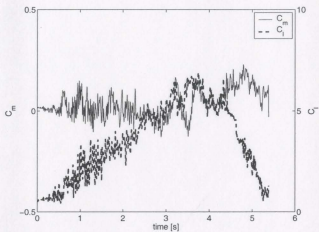


Figure 7.38: Moment and lift coefficients for moving cylinder at $Re = 10^5$ at $Re = 10^5$ for $I^* = m^*$

and lift coefficient curves appear to be moving in opposite directions, but start to become more in-phase with each other as the solution progresses.

Chapter 8

Conclusions & Recommendations

The objective of this research was to demonstrate the use of advanced CFD capabilities for the prediction of cylinder VIV responses at high Reynolds number and to expand the knowledge of VIV for cylinders free to translate and rotate. The present chapter summarizes the results of this research and makes recommendations for future work.

8.1 Summary of Code Development

In order to perform a simulation of vortex induced vibrations using the Numerical Wind Tunnel, considerable code development was required to advance an existing LES platform developed at Dalhousie University. The code development results lead to the following conclusions:

1. The surrounding cells method is an efficient algorithm for finding cells and faces surrounding a given cell in a computational domain. The method was successfully applied to a number of routines in this NWT, and will serve as a valuable tool for future applications and code development. Furthermore, the algorithm is useful for other CFD researchers using unstructured grids.

2. A bi-linear second-order velocity interpolation routine has been implemented into the NWT to improve the velocity prediction at the immersed boundary.
3. A routine was developed for the NWT to calculate the lift and drag forces on a body based on pressure measurements. This assumption is valid because it has been shown that the viscous contribution to the lift and drag forces is negligible for the flow regimes in this research ($Re = 10^5$). The routine effectively identifies the cells adjacent to an immersed boundary and calculates the lift and drag forces accordingly.
4. A "roughness" algorithm was developed and implemented into the NWT to calculate how closely the shape of the immersed boundary is approximated by the Cartesian mesh. This routine requires a validation study to relate the value obtained to the actual roughness, but has proven to be an effective tool for controlling the grid refinement around the immersed boundary (as discussed in section 4.4.1).
5. A method was developed to simulate the influence of span-wise force variation for objects undergoing vortex induced vibrations. The routine was built using the parameters normally applied to bodies experiencing vortex induced vibrations in pure translation, and hence additional damping and spring constants were not necessary. The routine requires the specification of the inertia ratio (I^*) and the moment coefficient (C_m) for a body in a flow, along with the C_l , C_d and other parameters common to translating VIV simulations.

8.2 Summary of Validation for 2nd-order interpolation

In order to validate the 2nd-order velocity interpolation, the flow over a circular cylinder at a Reynolds number of 100 was chosen as a benchmark case. The results of the validation lead to the following conclusions:

1. A grid independence study was performed on C_d , C_l , St , L_f and L/D for grids consisting of 10000 and 25000 cells. The lift and drag coefficients for this flow were well predicted by even the coarse mesh, but a finer mesh was necessary to obtain consistent values for the size of the separation bubble and eddy formation length. The simulation was assumed to be grid independent using an adaptation criterion of $c_{adapt} = 4E-05$, and the calculated C_d , C_l , St , L_f and L/D are within 5%, 13%, 0.6%, 8%, and 3% of the values reported in the literature.
2. The second-order interpolation routine produced more favourable results than an identical simulation using the first-order method. In particular, the lift coefficient, separation bubble size, and length of the eddy formation region predicted by the second-order method were in closer agreement with other experimental and numerical works.

8.3 Summary of Stationary Cylinder Simulations

The flow around a low aspect ratio cylinder at $Re = 10^5$ was numerically simulated using LES. This flow regime was selected based on the knowledge that it represents a somewhat realistic operating environment for marine risers. One of the objectives of the simulation was to investigate the presence of three-dimensional flow over the span of this cylinder, and the computational results led to the following conclusions:

1. The simulation was assumed to be grid independent using an adaptation criterion of $c_{adapt} = 4E-05$ and the calculated values of C_d , C_l and St are consistent with those reported in the literature. Specifically, $C_{l,rms} = 0.54$, which is within 2% of the experimental work of Norberg [53] with $C_{l,rms} = 0.55$. The average drag coefficient for the stationary cylinder was $C_d = 1.15$, which is within 4% of the experimental measurements of Schewe [65] and Achenbach [3], who obtained time averaged drag coefficients of $C_d = 1.20$. Finally, the predicted Strouhal number of $St = 0.183$ is also within 4% of the simulated results of Chen [20] with $St = 0.190$.
2. The 2S pattern of vortex shedding is consistent along the span of the cylinder, but the timing of shed vortices varies considerably. Plots of span-wise vorticity at various locations along the cylinder span indicate that vortices do not remain in-phase along the span of the cylinder. This phase variation is evidence of the lack of similarity in the near wake and indicates that the flow is three-dimensional.
3. The frequency of vortex shedding is constant along the span of the cylinder, and is not a good indicator of three-dimensionality in a flow due to phase differences over the span.
4. The flow is most correlated near the mid-span and becomes less correlated near the ends of the cylinder. Furthermore, the flow is shown to be anti-symmetric about the mid-span, implying that a moment exists about the cylinder mid-span due to an uneven distribution of forces.
5. The correlation length for this flow was computed to be 2.7, which is within thirteen percent of the empirical formulas reported in the literature at this Reynolds number.

6. The lift and drag forces are anti-symmetric about the mid-span and induce moments on the cylinder. The moment coefficient resulting from the lift forces is operating at a frequency different from the lift coefficient, which implies that the moment is not stationary, and varies over time.
7. The amplitude spectrum of the moment coefficient has a band of resonance from 0.09 to 0.25 Hz, with peaks located at 0.092, 0.18, and 0.24 Hz.

8.4 Summary of Moving Cylinder Simulations

The behaviour of a low aspect ratio cylinder experiencing vortex induced vibrations at $Re = 10^5$ was numerically simulated using LES. Modeling parameters were chosen to promote large oscillations and the simulations were intended to demonstrate local flow features generic to cases having span-wise amplitude variations. The simulations were performed for the case of a cylinder free to translate in the cross-stream direction, and also for a cylinder free to translate and rotate in a plane parallel to the cross-stream. Two different inertia ratios were investigated. A cylinder with an inertia ratio equal to unity was used to produce exaggerated results on the short cylinder, so that large amplitudes would exist at the ends of the cylinder, despite the small aspect ratio. Furthermore, the realistic case of a cylinder with its inertia ratio equal to its mass ratio was used to predict the response of the cylinder.

One of the objectives of the simulation was to investigate the influence of three-dimensional flow over the span of this cylinder, and the computational results led to the conclusions listed in the ensuing sections.

8.4.1 Summary of Results for Cross-Stream Translation

1. At the onset of motion the cylinder wake becomes more organized and highly correlated along the span. This supports the notion that three-dimensional flows become increasingly two-dimensional once the cylinder is allowed to respond to its shed vortices. As discussed in section 8.4.3 this behaviour was found to be limited to objects restricted to translation.
2. The correlation length increased from $\Lambda = 2.7$ for a stationary cylinder to $\Lambda = 3.0$ for a $3m$ cylinder undergoing translation at $Re = 10^5$.
3. The magnitude of the r.m.s moment coefficient decreased by 38% during translation. This is explained by the fact that the correlation length increased when the cylinder was allowed to move in the cross-stream direction.

8.4.2 Summary of Results for $I^* = 1$

1. The maximum values of the lift and drag coefficients more than quadrupled at the onset of VIV motion.
2. The vortex shedding at the mid-span showed a pair of co-rotating vortices. This pattern has previously been identified for the case of a cylinder vibrating as a pendulum, and has been denoted as 2C. Perhaps the segment from the point of rotation to the end of the cylinder behaves like a pendulum and induces similar vortex shedding patterns when oscillating.
3. Instantaneous iso-surfaces of stream-wise velocity show three structures at the ends of the cylinder merging together as the mid-span is approached. A conceptual model, constructed from cross-sectional measurements of vorticity, shows the existence of a 2C-(2P+S) antisymmetric hybrid mode across the span of

the cylinder. This is essentially a new mode of vortex shedding not previously identified in the literature.

4. At the onset of motion, there is virtually no region of force correlation except for a very narrow band around the mid-span. There is, however, increased symmetry in the flow-field, which is in direct contrast to stationary cylinder simulations, where there was higher correlation and less symmetry about the mid-span.
5. The correlation length, Λ , was computed to be 1.06, which is much smaller than $\Lambda = 2.7$ for the stationary cylinder.
6. The moment contribution due to lift is increased as a result of larger values of r.m.s lift, despite evidence of increased symmetry in the flow-field once the cylinder starts to move.

8.4.3 Summary of Results for $I^* = m^*$

1. The magnitude of the lift coefficient was 14% larger than for the case of pure translation, and 3% less than the case for $I^* = 1$. The value of the drag coefficient was 1% less than that predicted for the case of pure translation discussed in 7.2. Furthermore, the value of the drag coefficient in the upstream direction is approximately 50% smaller than that predicted for cylinder translating and rotating with $I^* = 1$.
2. The vortex shedding pattern shows a small pair of co-rotating vortices at the mid-span, and hints of it near the extremities. In contrast to the plots shown for the case of $I^* = 1$, the 2C pattern appears to persist along the span of the cylinder, most likely because the rotation angle is much smaller for the case

of $I^* = m^*$ and the flow is less affected by the translation of the ends of the cylinder.

3. The rotation angles are much smaller than for the case of a cylinder with $I^* = 1$.
4. The period of rotation for the cylinder with $I^* = m^*$ is about twice that for the case of $I^* = 1$.
5. The largest dimensionless amplitude was found for pure translation ($A_y = 1.5$), followed by $I^* = 1$ ($A_y = 1.3$) and $I^* = m^*$ ($A_y = 1.1$). Furthermore, the period of motion is shortest for the case of $I^* = m^*$.
6. The cross-stream velocity of the cylinder reached the largest values for $I^* = 1$ ($\frac{dz}{dt} = 0.8$) followed by $I^* = m^*$ ($\frac{dz}{dt} = 0.6$) and is smallest for the case of pure translation ($\frac{dz}{dt} = 0.5$).
7. The correlation length, Λ , for this flow-field was computed to be 2.6. This value is only slightly lower than $\Lambda = 2.7$ computed for the stationary cylinder, thus indicating that for cylinders with $I^* = m^*$ the onset of vortex induced vibration does not affect the magnitude of the correlation length to a large degree.
8. The correlation coefficient curve resembles that of the stationary cylinder in terms of magnitude and shape, but contains a more narrow band of highly correlated flow.
9. The values of the moment coefficient are larger than those reported for the stationary cylinder, due to the increase in the lift coefficient. At the onset of motion the moment and lift coefficient curves appear to be moving in opposite directions, but start to become more in-phase with each other as the solution progresses.

8.5 Significant Contributions to the Field

This research produced a number of new contributions to the field of VIV not previously identified in the literature. These contributions are summarized as follows:

- A model was developed to account for the influence of span-wise force variation for objects undergoing vortex induced vibrations. Conceptually the model consists of a pair of springs and dampers mounted to the ends of a cylinder, and uses many of the variables previously established for the simulation of VIV. The equations of motion have been developed to include a rotational component and the introduction of the inertia ratio.
- A new vortex shedding pattern has been identified for the case of a cylinder free to translate and rotate in a plane parallel to the cross-stream direction. At the mid-span, one of the co-rotating vortices evolves into a pair of counter-rotating vortices, thus producing a 2C-(2P+S) antisymmetric hybrid mode across the span of the cylinder. An investigation into the parameters influencing this mode, such as reduced velocity, Reynolds number, and range of inertia ratios, is justified.
- The assumption of two-dimensionality is only valid for the case of a cylinder undergoing pure translation. Models that restrict the motion to simple translation may govern the flow regime and not accurately reflect the behaviour of an object under less rigid constraints. This has implications for current numerical and experimental techniques since these models generally only allow for cross-stream and/or stream-wise motion. The extent to which the experimental apparatus or harmonic model influenced the behaviour of the riser by eliminating span-wise amplitude variation is important information that should be considered for future riser designs.

- While span-wise correlation should be discouraged on marine risers (either through strakes or some other means), the extent of span-wise correlation is likely being over-predicted by current experimental or numerical techniques.
- An investigation into the moment coefficient and span-wise force distribution for stationary and translating cylinders, as well as the case of cylinders free to rotate and translate in a plane parallel to the cross-stream direction was performed using LES. This information is useful in quantifying the magnitude and behaviour of the bending forces expected in the design of risers.

There have also been relatively few three-dimensional simulations of cylinders at $Re = 10^5$ reported in the literature, which makes the contributions described previously even more substantial.

8.6 Recommendations for Further Work

The following directions for extending the work of this thesis are suggested:

- Continue the current simulations for a longer period of simulated time to compute long-time averages and obtain statistically steady results. These simulations are ongoing, but progress has been slow due to the computational expenses outlined in section 6.1.1. In order to perform meaningful statistical analyses of these flows, in a reasonable amount of time, a greater number of processors must be used.
- Extend the simulations for a range of reduced velocities, mass ratios and inertia ratios to map the response of the cylinder under a variety of loading conditions. This is necessary to identify the parameters affecting the flow regime and in particular the presence of the 2C-(2P+S) hybrid mode.

- Extend the simulations to include a variety of aspect ratios so that the influence of large amplitude variation of the cylinder ends can be investigated.
- Expand the harmonic model to include the influence of span-wise force variation in the stream-wise direction.

Bibliography

- [1] Acenet website (no date), retrieved on 10th october 2005 from the world wide web:<http://www.ace-net.ca/users.html>.
- [2] Centre for marine development and research website (no date), retrieved on 31 june 2007 from the world wide web:<http://cfdnet.com/nwt/>.
- [3] E. Achenbach. Distribution of local pressure and skin friction around a circular riser in crossflow up to $re = 5,000,000$. *Journal of Fluid Mechanics*, 34:625–639, 1968.
- [4] E. Achenbach and Heinecke. On vortex shedding from smooth and rough cylinders in the range of reynolds numbers 6×10^3 to 5×10^6 . *Journal of Fluid Mechanics*, 109:239–251, 1981.
- [5] H. Al-Jamal and C. Dalton. Pressure fluctuation measurements on an oscillating circular cylinder. *Journal of Fluids and Structures*, 19:73–92, 2004.
- [6] P. Anagnostopoulos and G. Iliadis. Numerical study of the blockage effects on viscous flow past a circular cylinder. *International Journal for Numerical Methods in Fluids*, 22:1061–1074, 1996.
- [7] F. Angrilli, G. Di Silvio, and A. Zanardo. Hydroelastic study of a circular cylinder in a water stream. *IUTAM-IAHR Symposium*, 1972.

- [8] W. S. Atkins Consultants. *Best Practice Guidelines for Marine Applications of Computational Fluid Dynamics*. Marinet-CFD, 2003.
- [9] P.W. Bearman. Vortex shedding from oscillating bluff bodies. *Annual Review of Fluid Mechanics*, 16:195–222, 1984.
- [10] P.W. Bearman and I.G. Curie. Pressure fluctuation measurements on an oscillating circular cylinder. *Journal of Fluid Mechanics*, 91:661–667, 1979.
- [11] T. Bell. The numerical wind tunnel a three-dimensional computational fluid dynamics tool. Master's thesis, Department of Mechanical Engineering. Dalhousie University, Canada, 2003.
- [12] T. Bell, J. Militzer, and F. Ham. Simulations of vortex-induced vibrations of long cylinders with two degrees of freedom. *Proceedings of CFDSC 03: The 11th Annual Conference of the CFD Society of Canada, Vancouver, BC, May 28-30, 2003*.
- [13] E. Berger. The determination of hydrodynamic parameters of a karman eddy street from hot-wire measurements at low reynolds numbers (in german). *Zeitschrift fur Flugwissenschaften*, 12:41–59, 1964.
- [14] J. Bishop. Wave force data from the second christchurch bay tower. *Offshore Technology Conference*, OTC Number 4953, Houston, TX, USA, 1985.
- [15] R.E.D. Bishop and A.Y. Hassan. The lift and drag forces on a circular cylinder in a flowing fluid. *Proceedings of the Royal Society of London*, A 277:32–50, 1964.
- [16] R. D. Blevins. *Flow-Induced Vibrations: 2nd ed.* Van Nostrand Reinhold, New York, USA, 1990.

-
- [17] R.D. Blevins. On vortex-induced fluid forces on oscillating cylinders. *Proceedings of the ASME Pressure Vessels and Piping Division*, PVP 389:103–111, 1999.
- [18] M. Breuer. A challenging test case for large eddy simulation high reynolds number circular cylinder flow. *International Journal of Heat and Fluid Flow*, 21:648–654, 2000.
- [19] D. Brika and A. Laneville. Vortex-induced vibrations of a long flexible cylinder. *Journal of Fluid Mechanics*, 250:481–508, 1993.
- [20] H. Chen, C. Chen, R.S. Mercier, and J. P. Pontaza. Cfd simulation of riser viv. *Deepwater Riser VIV Project Comprehensive Status Report*, 2005.
- [21] C. Evangelinos and G.E Karniadakis. Dynamics and flow structures in the turbulent wake of rigid and flexible cylinders subject to vortex-induced vibrations. *Journal of Fluid Mechanics*, 400:91–124, 1999.
- [22] E. A. Fadlun, R. Verzicco, P. Orlandi, and J. Mohd-Yusof. Combined immersed-boundaries / b-splines methods for simulations of flows in complex geometries. *Annual Research Briefs, Centre for Turbulence Research, NASA Ames/Stanford Univ*, 2000.
- [23] C.-C. Feng. The measurement of vortex induced effects in flow past stationary and oscillating circular and d-section cylinders. Master's thesis, Department of Mechanical Engineering. University of British Columbia, Canada, 1968.
- [24] J. H. Ferziger and M Perić. *Computational Methods for Fluid Dynamics: 3rd rev. ed.* Springer Verlag, 2002.
- [25] F. Flemming and C. H. K. Williamson. Vortex-induced vibrations of a pivoted cylinder. *Journal of Fluid Mechanics*, 522:215–252, 2005.

-
- [26] C. A. Friehe. Vortex shedding from cylinders at low reynolds numbers. *Journal of Fluid Mechanics*, 100:237–241, 1980.
- [27] R.D. Gabbai and H. Benaroya. An overview of modeling and experiments of vortex-induced vibration of circular cylinders. *Journal of Sound and Vibration*, 282:575–616, 2005.
- [28] R. Gopalkrishnan. PhD thesis, Department of Ocean Engineering, MIT, 1993.
- [29] R. Govardhan and C.H.K. Williamson. Motions, forces and mode transitions in vortex-induced vibrations at low mass-damping. *Journal of Fluid Mechanics*, 420:85–130, 2000.
- [30] F.E. Ham, F.S. Lien, and A.B Strong. A cartesian grid method with transient anisotropic adaptation. *J. Comp. Physics*, 179:469–494, 2002.
- [31] F.S. Hover, A.H. Techet, and M.S. Triantafyllou. Forces on oscillating uniform and tapered cylinders in crossflow. *Journal of Fluid Mechanics*, 363:97–114, 1998.
- [32] J. S. Humphreys. On a circular cylinder in a steady wind at transition reynolds number. *Journal of Fluid Mechanics*, 9:603–612, 1960.
- [33] J.A. Humphries and D.H. Walker. Vortex-excited response of large-scale cylinders in sheared flow. *ASME Journal of Offshore Mechanics and Arctic Engineering*, 110:272–277, 1988.
- [34] E. Huse, G. Kleiven, and F.G. Nielsen. Large scale model testing of deep sea risers. *Offshore Technology Conference*, OTC Number 8701, 4-7 May, Houston, TX, USA, 1998.

- [35] N. Jauvtis and C.H.K. Williamson. Vortex induced vibration of a cylinder in two degrees of freedom. *Conference on Bluff Body Wakes and Vortex-Induced Vibrations, Port Douglas, Australia, Dec. 2002*.
- [36] N. Jauvtis and C.H.K. Williamson. A high-amplitude 2nd mode of vortex formation, and the effects of non-harmonic forcing in vortex induced vibration. *Eur. J. Mech. B Fluids*, 23:107–114, 2004.
- [37] J.-Y. Jong and J.K. Vandivier. The identification of the quadratic system relating cross-flow and in-line vortex-induced vibration. *Dynamic System Measurement and Control, ASME Winter Annual Meeting, 1985*.
- [38] Y. Kasahara. Wave forces acting on rough circular cylinders at high reynolds numbers. *Offshore Technology Conference, OTC Number 5372, Houston, TX, USA, 1987*.
- [39] A. Khalak and C.H.K. Williamson. Dynamics of a hydroelastic cylinder with very low mass and damping. *Journal of Fluids and Structures*, 10:455–472, 1996.
- [40] A. Khalak and C.H.K. Williamson. Motions, forces and mode transitions in vortex-induced vibrations at low mass-damping. *Journal of Fluids and Structures*, 13:813–851, 1999.
- [41] D. Kim and H Choi. A second-order time-accurate finite volume method for unsteady incompressible flow on hybrid unstructured grids. *J. Comp. Physics*, 162:411–420, 2002.
- [42] P. K. Kundu and I. M. Cohen. *Fluid Mechanics: 3rd ed.* Elsevier Academic Press, California, USA, 2004.

- [43] X. Lu, C. Dalton, and J. Zhang. Application of large eddy simulation to an oscillating flow past a circular cylinder. *Journal of Fluids Engineering*, 119:519–525, 1997.
- [44] S. C. Luo and H. M. Xia. Parallel vortex shedding at $re = 10,000$ a transverse control cylinder technique approach. *Journal of Fluid Mechanics*, 541:143–165, 2005.
- [45] H. Marcollo and J.B. Hinwood. Vortex-induced-vibration of a long flexible cylinder with both forcing and response. *Conference on Bluff Body Wakes and Vortex-Induced Vibrations, Port Douglas, Australia, Dec. 2002*.
- [46] J.T. McClave and F.H. Dietrich. *Statistics*. Maxwell Macmillan, New York, USA, 1994.
- [47] J.A. Mercier. *Large amplitude oscillations of a circular cylinder in a low speed stream*. PhD thesis, Stevens Institute of Technology, Hoboken, NJ, USA, 1973.
- [48] V. Michelassi, J.G. Wissink, J. Fröhlich, and W. Rodi. Large-eddy simulation of flow around low-pressure turbine blades with incoming wakes. *AIAA Journal*, 41:2143–2156, 2003.
- [49] S. Mittal. Computation of 3d flows past circular cylinders of low aspect ratio. *Physics of Fluids*, 13:177–191, 2001.
- [50] G. Moe and Z.-J. Wu. the lift force on a cylinder vibrating in a current. *ASME Journal of Offshore Mechanics and Artic Engineering*, 112:297–303, 1990.
- [51] Young D. F. Munson, B. R. and T. H. Okiishi. *Fundamentals of Fluid Mechanics: 3rd ed.* John Wiley and Sons Inc, New York, USA, 1994.

- [52] M. Nishioka and H. Sato. Mechanism of determination of the shedding frequency of vortices behind a cylinder at low reynolds numbers. *Journal of Fluid Mechanics*, 89:49–60, 1978.
- [53] C. Norberg. Flow around a circular cylinder: Aspects of fluctuating lift. *J. Fluids and Structures*, 15:459–469, 2001.
- [54] C. Norberg. Fluctuating lift on a circular cylinder: review and new measurements. *Journal of Fluids and Structures*, 17:57–96, 2003.
- [55] Heideman J. Norton, D. and W. Mallard. Wind tunnel tests of inclined cylinders. *Offshore Technology Conference*, OTC Number 4122, Houston, TX, USA, 1981.
- [56] J. Park, K. Kwon, and H. Choi. Numerical solutions of flow past a circular cylinder at reynolds numbers up to 160. *KSME Int J*, 12:1200, 1998.
- [57] C. S. Peskin. Flow patterns around heart valves: A numerical method. *Journal of Computational Physics*, 10:252–271, 1972.
- [58] P. Roache. *Verification and Validation in Computational Science and Engineering*. Hermosa Publishing, New Mexico, USA, 1998.
- [59] A Roshko. On the drag and shedding frequency of two-dimensional bluff bodies. *National Advisory Committee for Aeronautics, NACA TN*, 3169:3–5, 1953.
- [60] P. Sampaio and A. Coutinho. Simulating vortex shedding at high reynolds numbers. *10th International Offshore and Polar Engineering Conference, 2000*.
- [61] T. Sarpkaya. Inline and transverse forces on cylinders in oscillatory flow with high reynolds numbers. *Journal of Ship Research*, 21:200–216, 1977.
- [62] T. Sarpkaya. Fluid forces on oscillating cylinders. *Journal of Waterway Port Coastal and Ocean Division ASCE*, 104:275–290, 1978.

- [63] T. Sarpkaya. Hydrodynamic damping, flow-induced oscillations, and biharmonic response. *ASME Journal of Offshore Mechanics and Arctic Engineering*, 117:232–238, 1995.
- [64] T. Sarpkaya. A critical review of the intrinsic nature of vortex induced vibrations. *Journal of Fluids and Structures*, 19:389–447, 2004.
- [65] G. Schewe. On the force fluctuations acting on a circular cylinder in crossflow from subcritical up to transcritical reynolds numbers. *Journal of Fluid Mechanics*, 133:265–285, 1983.
- [66] W. C. L. Shih, C. Wang, D. Cols, and A. Roshko. 1993 experiments on flow past rough circular cylinders at large reynolds numbers. *J. Wind Eng. and Industrial Aerodynamics*, 49:351–368, 1993.
- [67] S. Singh and S. Mittal. Energy spectra of flow past a circular cylinder. *International Journal of Computational Fluid Dynamics*, 18:671–679, 2004.
- [68] A. Slaouti and J.H. Gerrard. An experimental investigation of the end effects on the wake of a circular cylinder towed through water at low reynolds numbers. *Journal of Fluid Mechanics*, 112:297–314, 1981.
- [69] J. Smagorinsky. General circulation experiments with primitive equations i. the basic experiment. *Monthly Weather Review*, 91:99–164, 1963.
- [70] R.M.C. So, Y. Liu, C.H. Cui, and X.Q. Wang. Three-dimensional wake effects on flow-induced forces. *Journal of Fluids and Structures*, 20:373–402, 2005.
- [71] P. K Stansby. The locking-on of vortex shedding due to the cross stream vibration of circular cylinders in uniform and shear flows. *Journal of Fluid Mechanics*, 74:641–665, 1976.

- [72] T. Staubli. Calculation of the vibration of an elastically mounted cylinder using experimental data from forced oscillation. *ASME Journal of Fluid Mechanics*, 74:641–665, 1983.
- [73] Deep Oil Technology. Joint industry program on vortex induced motions of large floating platforms, 1992.
- [74] M.S. Triantafyllou, A.H. Techet, F.S. Hover, and D.K.P. Yue. Viv of slender structures in shear flow. *IUTAM Symposium on Flow-Structure Interactions, June 2003, Rutgers State University, USA*.
- [75] M. Tutor and A.E. Holdo. Large eddy simulation of a smooth cylinder oscillating normal to uniform flow. *Journal of Fluids Engineering*, 122:694–702, 2000.
- [76] A. Voorhees and T. Wei. Three-dimensionality in the wake of a surface piercing cylinder mounted as an inverted pendulum. *Conference on Bluff Body Wakes and Vortex-Induced Vibration, Port Douglas, Australia, 17-20 December 2002*.
- [77] J. B. Vos. Thematic area 1: Best practice advice for external aerodynamics. *QNET-CFD Network Newsletter*, 2:10–13, 2004.
- [78] M. Wang, P. Catalano, and G. Iaccarino. Prediction of high reynolds number flow over a circular cylinder using les with wall modeling. *Annual Research Briefs, Center for Turbulence Research, NASA Ames/Stanford Univ.*, pages 351–368, 2001.
- [79] K. A. Warshauer and J. A. Leene. Experiments on mean and fluctuating pressures of circular cylinders at cross flow at very high reynolds numbers. In *Proceedings Conference Wind Effects on Buildings and Structures*, pages 305–15, 1971.

- [80] F. White. *Viscous Fluid Flow, 3rd Edition*. McGraw Hill Science/Engineering, New York, USA, 2006.
- [81] J. J. Wilde and R. H. M. Huijsmans. Experiments for high reynolds numbers viv on risers. In *The Proceedings of the Eleventh International And Polar Engineering Conference Vol. 3*, pages 400–405, 2001.
- [82] C.H.K. Williamson. The existence of two stages in the transition to three-dimensionality of a cylinder wake. *Physics of Fluids*, 31:3165–3168, 1988.
- [83] C.H.K Williamson. Three dimensional aspects and transition in the wake of a circular cylinder. *7th Symposium Turbulent Shear Flows, Stanford, CA*, page (4), 1989.
- [84] C.H.K Williamson. Vortex dynamics in the cylinder wake. *Annu. Rev. Fluid Mech.*, pages 477–539, 1996.
- [85] C.H.K Williamson and A. Roshko. Vortex formation in the wake of an oscillating cylinder. *Journal of Fluids and Structures*, 2:355–381, 1988.
- [86] Z. Wu. PhD thesis, Civil Engineering, The Norwegian Institute of Technology, 1989.
- [87] M.M. Zdravkovich. Modification of vortex shedding in the synchronization range. *Journal of Fluids Engineering*, 104:513–517, 1982.
- [88] M.M. Zdravkovich. Different modes of vortex sheeding: an overview. *Journal of Fluids and Structures*, 10:427–437, 1996.
- [89] M.M. Zdravkovich. *Flow Around Circular Cylinders*. Oxford University Press, New York, USA, 1997.

Appendix A: Grid Refinement Study

Grid Convergence estimates

Important equations

$$r = r_{eff} = \left(\frac{N_2}{N_1} \right)^{\frac{1}{p}}$$

$$p = \ln \left(\frac{f_2 - f_1}{f_1 - f_0} \right) / \ln(r)$$

$$f_{h \rightarrow 0} = f_1 + \frac{f_1 - f_0}{r^p - 1}$$

$$e = \frac{f_1 - f_0}{f_1}$$

$$CGI_{12} = \frac{F_{ref} |e_{12}|}{r^p - 1}$$

$$CGI_{23} = \frac{F_{ref} |e_{23}|}{r^p - 1}$$

$$asymptotic = \frac{CGI_{23}}{r^p CGI_{12}}$$

Calculate the grid refinement ratio, r , based on the number of cells in the fine grid (N_1) and coarser grid (N_2).

calculate the order of convergence (p), and let $f = Cd, Cl, St$

Use Richardson extrapolation on the two finest grids to obtain an estimate of the value of f at a grid spacing of zero

the relative error is given by epsilon

Calculate the Grid Convergence Index for each of the grids using a factor of safety of 1.25 (see Roache)

Are the solutions in the asymptotic range of convergence (close to unity)

If they are in the asymptotic band we can say that the value of f is estimated to be $f_{h \rightarrow 0}$ with an error band of CGI_{12}

Grid Steps	Cd	Cl	St	e adapt
N1	75000	1.17	0.85	0.214
N2	26500	1.14	0.8	0.211
N3	8700	1.0318	0.5	0.183

F_{ref}	1.25
r	1.414507

Order of Convergence	Cd	Cl	St
p	3.8991177	3.997806	3.4400270

Error estimates			
	Cd	Cl	St
e_{12}	0.026318	0.0025	0.014218
e_{23}	0.104895	0.333333	0.1530025

CGI12	0.012619	0.029671	0.0068181
CGI23	0.050287	0.159847	0.0733722

Does each grid level yield solutions in asymptotic range?

$r^p CGI_{12}$	Cd	Cl	St
	0.045514	0.119895	0.0636356
	1.104895	1.333333	1.1530025

They are all close to 1.00, but Cd is the best

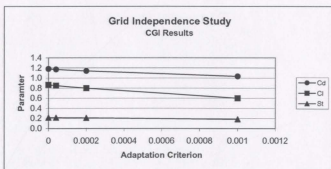
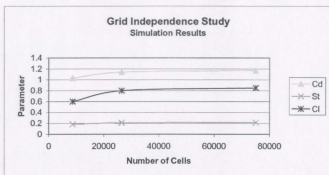
So we apply Richardson extrapolation using the two finest grids to obtain an estimate of the value of the lift at zero grid spacing

- use order of convergence p , and finest two grid results

zero spacing	Cd	Cl	St
	1.181509	0.866667	0.21436

Summary of Results

c_adapt	Cd	Cl	ST
0	1.182	0.867	0.214
4.00E-05	1.170	0.850	0.214
2.00E-04	1.140	0.800	0.211
1.00E-03	1.032	0.600	0.183




```

1  % ***** Dave Murrin, 04/04/2007 *****
2  % The following is a script to analyze the moments along the span of the
3  % cylinder using the spanwise lift and drag output from the NWT
4  % Note that the final output uses the moment coefficient, which is the
5  % moment normalized by the length of the cylinder.
6  % D Murrin
7  %
8  avg_lift_drag_trace = load('avg_lift_drag.csv');
9  lift_drag_0_5 = load('lift_drag_0.30');
10 lift_drag_1_0 = load('lift_drag_0.60');
11 lift_drag_1_5 = load('lift_drag_0.90');
12 lift_drag_2_0 = load('lift_drag_1.20');
13 lift_drag_2_5 = load('lift_drag_1.50');
14 lift_drag_3_0 = load('lift_drag_1.80');
15 lift_drag_3_5 = load('lift_drag_2.10');
16 lift_drag_4_0 = load('lift_drag_2.40');
17 lift_drag_4_5 = load('lift_drag_2.70');
18 %*****
19 span_cuts = [-0.4:1:0.4]';%normalized lengths
20 span_cuts = [-1.2:3:1.2]';%
21 %should check against the raw data from avg_lift_drag
22 %check the final value
23 avg_lift_drag_trace(end,:);
24 ave_check(1,:) = lift_drag_0_5(end,:);
25 ave_check(2,:) = lift_drag_1_0(end,:);
26 ave_check(3,:) = lift_drag_1_5(end,:);
27 ave_check(4,:) = lift_drag_2_0(end,:);
28 ave_check(5,:) = lift_drag_2_5(end,:);
29 ave_check(6,:) = lift_drag_3_0(end,:);
30 ave_check(7,:) = lift_drag_3_5(end,:);
31 ave_check(8,:) = lift_drag_4_0(end,:);
32 ave_check(9,:) = lift_drag_4_5(end,:);
33 % Now we check the average lift and drag
34 average_values = mean(ave_check,1)
35 %now we can calculate the moment contribution
36 for iter = 1:9
37     mom_contrib(iter) = ave_check(iter,2)*span_cuts(iter);
38 end
39 mom_check = sum(mom_contrib)/9
40 mom_from_arm = avg_lift_drag_trace(end,4)*avg_lift_drag_trace(end,2)
41 % We must verify the average values with the cut values in the .out file
42 % Now, call the strouhal routine for avg drag, lift and strouhal
43 avg_cl_cd = strouhal2(avg_lift_drag_trace);
44 avg_0_5 = strouhal2(lift_drag_0_5);
45 avg_1_0 = strouhal2(lift_drag_1_0);
46 avg_1_5 = strouhal2(lift_drag_1_5);
47 avg_2_0 = strouhal2(lift_drag_2_0);
48 avg_2_5 = strouhal2(lift_drag_2_5);
49 avg_3_0 = strouhal2(lift_drag_3_0);
50 avg_3_5 = strouhal2(lift_drag_3_5);
51 avg_4_0 = strouhal2(lift_drag_4_0);

```

```

52 avg_4_5 = strouhal2(lift_drag_4_5);
53 %*****
54 %So, now we have the filtered lift and drag at the cuts. So we will find
55 %the moments and draw a spline through the results
56 %clmom = cilmov(n_cuts-1)*(location - globalLength[1]/2)/globalLength[1];
57 %clmom_sum = cilmom + clmom_sum;
58 %calculate lift moments
59 %plot(avg_0_5(:,1),clmom)
60 % Now we fit the data to a spline so that the timesteps are even
61 % set the timesteps to 0.001 seconds
62 dummy_avgl(:,1) = avg_lift_drag_trace(:,1);
63 dummy_avgl(:,2) = avg_lift_drag_trace(:,4);
64 dummy_avgl(:,3) = avg_lift_drag_trace(:,4);
65 dummy_ones = strouhal2(dummy_avgl);
66 plot(dummy_ones(:,1),dummy_ones(:,2))
67 title('C_m vs time');
68 xlabel('time [s]')
69 ylabel('C_m')
70 %% May be interesting to get the frequency and rms values of the moment
71 stat_results = strouhal3(dummy_ones);
72 %-----
73 %Now plot results
74 %%We should also plot the variation of Cl and Cd over the span
75 %create a vector of the Cd
76 ave_drag(1,:) = 2*mean(lift_drag_0_5(:,3));
77 ave_drag(2,:) = 2*mean(lift_drag_1_0(:,3));
78 ave_drag(3,:) = 2*mean(lift_drag_1_5(:,3));
79 ave_drag(4,:) = 2*mean(lift_drag_2_0(:,3));
80 ave_drag(5,:) = 2*mean(lift_drag_2_5(:,3));
81 ave_drag(6,:) = 2*mean(lift_drag_3_0(:,3));
82 ave_drag(7,:) = 2*mean(lift_drag_3_5(:,3));
83 ave_drag(8,:) = 2*mean(lift_drag_4_0(:,3));
84 ave_drag(9,:) = 2*mean(lift_drag_4_5(:,3));
85 %-----
86 %create vector of Cl
87 rms_lift(1,:) = norm(lift_drag_0_5(:,2))/sqrt(length(lift_drag_0_5(:,2)));
88 rms_lift(2,:) = norm(lift_drag_1_0(:,2))/sqrt(length(lift_drag_1_0(:,2)));
89 rms_lift(3,:) = norm(lift_drag_1_5(:,2))/sqrt(length(lift_drag_1_5(:,2)));
90 rms_lift(4,:) = norm(lift_drag_2_0(:,2))/sqrt(length(lift_drag_2_0(:,2)));
91 rms_lift(5,:) = norm(lift_drag_2_5(:,2))/sqrt(length(lift_drag_2_5(:,2)));
92 rms_lift(6,:) = norm(lift_drag_3_0(:,2))/sqrt(length(lift_drag_3_0(:,2)));
93 rms_lift(7,:) = norm(lift_drag_3_5(:,2))/sqrt(length(lift_drag_3_5(:,2)));
94 rms_lift(8,:) = norm(lift_drag_4_0(:,2))/sqrt(length(lift_drag_4_0(:,2)));
95 rms_lift(9,:) = norm(lift_drag_4_5(:,2))/sqrt(length(lift_drag_4_5(:,2)));
96 %PLOT SPANWISE AVERAGES AND RMS VALUES
97 xx = -1.2:.05:1.2;
98 %yy_L = spline({0:span_cuts;5},{0:rms_lift_at_cut;0},xx);
99 yy_L = spline(span_cuts,rms_lift,xx);
100 figure
101 plot(xx,yy_L,'k-',span_cuts,rms_lift,'ko')
102 title('AVERAGE SPAN WISE RMS LIFT COEFFICIENT');

```

```

103 ylabel('C1')
104 xlabel('Span wise length [m]')
105 yy = spline(span_cuts,ave_drag,xx);
106 figure
107 plot(xx,yy,'k-',span_cuts,ave_drag,'ko')
108 title('AVERAGE SPAN WISE DRAG COEFFICIENT');
109 ylabel('Cd')
110 xlabel('Span wise length [m]')
111 % ***** 3D plots of lift and drag *****
112 %check the lengths of the arrays, and and truncate if necessary, and plot
113 %the distance from 1:length(minlength)
114 lcheck(1) = length(avg_0_5(:,1));
115 lcheck(2) = length(avg_1_0(:,1));
116 lcheck(3) = length(avg_1_5(:,1));
117 lcheck(4) = length(avg_2_0(:,1));
118 lcheck(5) = length(avg_2_5(:,1));
119 lcheck(6) = length(avg_3_0(:,1));
120 lcheck(7) = length(avg_3_5(:,1));
121 lcheck(8) = length(avg_4_0(:,1));
122 lcheck(9) = length(avg_4_5(:,1));
123 min(lcheck)
124 %truncate to minimum length
125 avg_0_5 = avg_0_5(1:min(lcheck),:);
126 avg_1_0 = avg_1_0(1:min(lcheck),:);
127 avg_1_5 = avg_1_5(1:min(lcheck),:);
128 avg_2_0 = avg_2_0(1:min(lcheck),:);
129 avg_2_5 = avg_2_5(1:min(lcheck),:);
130 avg_3_0 = avg_3_0(1:min(lcheck),:);
131 avg_3_5 = avg_3_5(1:min(lcheck),:);
132 avg_4_0 = avg_4_0(1:min(lcheck),:);
133 avg_4_5 = avg_4_5(1:min(lcheck),:);
134 %plot3(t,L,C1)
135 span_lift(:,1) = avg_0_5(:,2);
136 %spanwise_dist(:,1) = -0.4*ones(length(span_lift(:,1)),1);
137 spanwise_dist(:,1) = -0.4*ones(length(span_lift(:,1)),1);
138 spanwise_dist(:,2) = -0.3*ones(length(span_lift(:,1)),1);
139 spanwise_dist(:,3) = -0.2*ones(length(span_lift(:,1)),1);
140 spanwise_dist(:,4) = -0.1*ones(length(span_lift(:,1)),1);
141 spanwise_dist(:,5) = 0*ones(length(span_lift(:,1)),1);
142 spanwise_dist(:,6) = 0.1*ones(length(span_lift(:,1)),1);
143 spanwise_dist(:,7) = 0.2*ones(length(span_lift(:,1)),1);
144 spanwise_dist(:,8) = 0.3*ones(length(span_lift(:,1)),1);
145 spanwise_dist(:,9) = 0.4*ones(length(span_lift(:,1)),1);
146 %
147 plot3(avg_0_5(:,1),spanwise_dist(:,1),avg_0_5(:,2),avg_1_0(:,1),spanwise_dist(:,2),av
g_1_0(:,2))
148 hold
149 plot3(avg_1_5(:,1),spanwise_dist(:,3),avg_1_5(:,2),avg_2_0(:,1),spanwise_dist(:,4),av
g_2_0(:,2))
150 plot3(avg_2_5(:,1),spanwise_dist(:,5),avg_2_5(:,2),avg_3_0(:,1),spanwise_dist(:,6),av
g_3_0(:,2))

```

```

151 plot3(avg_3_5(:,1),spanwise_dist(:,7),avg_3_5(:,2),avg_4_0(:,1),spanwise_dist(:,8),av
g_4_0(:,2))
152 plot3(avg_4_5(:,1),spanwise_dist(:,9),avg_4_5(:,2))
153 xlabel('time [s]')
154 ylabel('Span wise location [y/L]')
155 zlabel('C_1')
156 #zlabel('C_{itl}')
157 hold off
158 %*****
159 % Correlation coefficients between midplane and other values
160 %collect all of the data into a single matrix
161 Corr_pairs = [avg_0_5(:,2),avg_1_0(:,2),avg_1_5(:,2),avg_2_0(:,2),avg_2_5(:,2),avg_3_
0(:,2),avg_3_5(:,2),avg_4_0(:,2),avg_4_5(:,2)];
162 for c_i=1:9
163     CP1 = [Corr_pairs(:,c_i),Corr_pairs(:,5)];
164     [corr_r,corr_p] = corrcoef(CP1);
165     corr_coeff(c_i) = corr_r(2);
166 end
167 %now plot correlation coefficients against span position
168 figure
169 span_interp = -1.5:0.01:1.5;
170 interp_coeff = [pchip(span_cuts,corr_coeff,span_interp)];
171 Correlation_Length = trapz(span_interp,interp_coeff);
172 plot(span_cuts,corr_coeff,'ko',span_interp,interp_coeff)
173 xlabel('Span wise location [y/L]')
174 ylabel({'\gamma_{itij}'}
175 %-----
176 %plot moment along with lift
177 plot(dummy_ones(:,1),dummy_ones(:,2))
178 time = dummy_ones(:,1);
179 mom = dummy_ones(:,2);
180 plotyy(time,mom,avg_cl_cd(:,1),avg_cl_cd(:,2))
181 [AX,H1,H2] = plotyy(time,mom,avg_cl_cd(:,1),avg_cl_cd(:,2),'plot');
182 set(get(AX(1),'Ylabel'),'String','C_m')
183 set(get(AX(2),'Ylabel'),'String','C_1')
184 set(H1,'LineStyle','-')
185 set(H1,'Color','k')
186 set(get(AX(1),'Ylabel'),'Color','k')
187 set(get(AX(2),'Ylabel'),'Color','k')
188 set(AX(1),'YColor','k')
189 set(AX(2),'YColor','k')
190 set(H2,'LineStyle',':')
191 set(H2,'Color','k')
192 title('C_m vs time');
193 xlabel('time [s]')
194 egh = legend([H1 H2],'C_m','C_1');
195

```

```

1 function results = strouhal(lift_drag)
2 % matlab code for finding rms values
3 %import data file, or cd into directory and open it
4 %NOTE: For the strouhal number it is important to ensure
5 %that dt is relatively constant
6 %Store original data
7 raw_data = lift_drag;
8 %%%%%%%%%%%%%%%%%%%%%%%%%%%%%%%%%%%%%%%%%%%%%%%%%%%%%%%%%%%%%%%%%%%%%%%%%
9 %% Remove outliers
10 % Calculate the mean and the standard deviation
11 % of each data column in the matrix
12 % Calculate the mean and the standard deviation
13 % of each data column in the matrix
14 %%%%%%%%%%%%%%%%%%%%%%%%%%%%%%%%%%%%%%%%%%%%%%%%%%%%%%%%%%%%%%%%%%%%%%%%%
15 % first add a column of delta_CL and delta_CD
16 % calculating deltas
17 count = lift_drag;
18 [N,P] = size(count);
19 for C = 2:N
20     count(C,4) = count(C,2)-count(C-1,2) ;
21     count(C,5) = count(C,3)-count(C-1,3) ;
22 end
23 %%%%%%%%%%%%%%%%%%%%%%%%%%%%%%%%%%%%%%%%%%%%%%%%%%%%%%%%%%%%%%%%%%%%%%%%%
24 mu = mean(count);
25 sigma = std(count);
26 [n,p] = size(count);
27 % Create a matrix of mean values by
28 % replicating the mu vector for n rows
29 MeanMat = repmat(mu,n,1);
30 % Create a matrix of standard deviation values by
31 % replicating the sigma vector for n rows
32 SigmaMat = repmat(sigma,n,1);
33 % Create a matrix of zeros and ones, where ones indicate
34 % the location of outliers
35 outliers = abs(count - MeanMat) > 2*SigmaMat;
36 % Calculate the number of outliers in each column
37 nout = sum(outliers);
38 count(any(outliers,2),:) = [];
39 %replace data
40 time = count(:,1);
41 lift = count(:,2);
42 drag = count(:,3);
43 delta_lift = count(:,4);
44 delta_drag = count(:,5);
45 %replace original matrix
46 lift_drag = [time, lift, drag];
47 %%%%%%%%%%%%%%%%%%%%%%%%%%%%%%%%%%%%%%%%%%%%%%%%%%%%%%%%%%%%%%%%%%%%%%%%%End of Outliers Routine %%%%%%%%%%%%%%%%%%%%%%%%%%%%%%%%%%%%%%%%%%%%%%%%%%%%%%%%%%%%%%%%%%%%%%%%%
48 min_value = 1;
49 %filter the data first
50 b = ones(1,10)/10;
51 yall = filtfilt(b,1, lift_drag);

```

```

52 lift_drag = yall;
53 % data filtered and replaced
54 %%%%%%%%%%%%%%%%%%%%%%%%%%%%%%%%%%%%%%%%%%%%%%%%%%%%%%%%%%%%%%%%%%%%%%%%%
55 time = lift_drag(min_value:length(lift_drag),1);
56 %lift = detrend(lift_drag(min_value:length(lift_drag),2));
57 lift = lift_drag(min_value:length(lift_drag),2);
58 drag = lift_drag(min_value:length(lift_drag),3);
59 %%%%%%%%%%%%%%%%%%%%%%%%%%%%%%%%%%%%%%%%%%%%%%%%%%%%%%%%%%%%%%%%%%%%%%%%%
60 %Zero the time
61 t_0 = time(1);
62 t_zeroed = time - time(1);
63 time = t_zeroed;
64 %%%%%%%%%%%%%%%%%%%%%%%%%%%%%%%%%%%%%%%%%%%%%%%%%%%%%%%%%%%%%%%%%%%%%%%%%
65 % Now we fit the data to a spline so that the timesteps are even
66 % set the timesteps to 0.001 seconds
67 delta_t = 0.001;
68 time_vector = time(1):delta_t:time(end);
69 % Now fit the lift and drag coefficients to a cubic spline
70 YI_L = interp(time, lift, time_vector);
71 YI_D = interp(time, drag, time_vector);
72 %look at approximation
73 %plot(time, lift, time_vector, YI_L, 'o')
74 time = time_vector';
75 lift = YI_L';
76 drag = YI_D';
77 %%%%%%%%%%%%%%%%%%%%%%%%%%%%%%%%%%%%%%%%%%%%%%%%%%%%%%%%%%%%%%%%%%%%%%%%%
78 %Compute RMS and mean of data
79 rms_drag = norm(drag)/sqrt(length(drag));
80 rms_lift = norm(lift)/sqrt(length(lift));
81 Avg_drag = mean(drag);
82 %%%%%%%%%%%%%%%%%%%%%%%%%%%%%%%%%%%%%%%%%%%%%%%%%%%%%%%%%%%%%%%%%%%%%%%%%
83 y0 = lift;
84 N = length(y0);
85 M = 2^nextpow2(N);
86 y = [ y0 ; zeros(M-N,1)];
87 Fs = N/(time(N) - time(1));
88 dt = 1/Fs;
89 t = dt*(0:M-1)';
90 df = Fs/M;
91 f = df*(0:M-1)';
92 Y = fft(y0,M);
93 Pyy = Y.* conj(Y) / M;
94 %%%%%%%%%%%%%%%%%%%%%%%%%%%%%%%%%%%%%%%%%%%%%%%%%%%%%%%%%%%%%%%%%%%%%%%%%
95 % Truncate to non-negative frequencies
96 % and find peaks
97 Q = ceil((M+1)/2);
98 Pyy1 = Pyy(1:Q);
99 f1 = f(1:Q);
100 [Pymax Imax1] = max(Pyy1);
101 Imax = find(Pyy1 == Pymax);
102 figure(3), plot(f1, Pyy1)

```

```
103 hold on, plot(f1(Imax),Pyy1(Imax),'bo')
104 xlim([0 5])
105 title('Single-Sided Amplitude Spectrum of CL(t)');
106 xlabel('frequency [Hz]')
107 ylabel('|Y(f)|') % or Power Spectrum
108 ylabel('Pyy(f)') % or Power Spectrum
109 hold off
110 St = f1(Imax);
111 %%%%%%%%%%%%%%%%%%%%%%%%%%%%%%%%%%%%%%%%%%%%%%%%%%%%%%%%%%%%%%%%%%%%%%%%%
112 % Plot lift and drag vs time
113 figure(4),plot(time,drag,'k',time,lift,'k:')
114 title('CD, CL vs time');
115 xlabel('time [s]')
116 ylabel('CD,CL')
117 legend('CD','CL');
118 %%%%%%%%%%%%%%%%%%%%%%%%%%%%%%%%%%%%%%%%%%%%%%%%%%%%%%%%%%%%%%%%%%%%%%%%%
119 %% plot the filtered and unfiltered data
120 time_orig = time + t_0;
121 figure(5),plot(raw_data(:,1),raw_data(:,2),time_orig,lift,'--','LineWidth',2)
122 title('Unfiltered and Filtered CL vs time');
123 xlabel('time [s]')
124 ylabel('CL')
125 legend('Unfiltered CL','Filtered CL');
126 %%%%%%%%%%%%%%%%%%%%%%%%%%%%%%%%%%%%%%%%%%%%%%%%%%%%%%%%%%%%%%%%%%%%%%%%%
127 %% Display the results
128 results = [Avg_drag , rms_lift , St];
129 disp(' Cd(avg) Cl(rms) Strouhal')
130 disp(results)
131
132
```